Extreme Ultraviolet Lensless Microscopy:

Development and Potential Applications to Semiconductor Metrology

by

Bin Wang

B.S., University of Science and Technology of China, 2016

M.S., University of Colorado Boulder, 2019

A thesis submitted to the

Faculty of the Graduate School of the

University of Colorado in partial fulfillment

of the requirement for the degree of

Doctor of Philosophy

Department of Physics

2022

Committee Members:

Margaret Murnane, Chair

Henry Kapteyn

Robert McLeod

Markus Raschke

Michael Toney

Wang, Bin (Ph.D., Physics)

Extreme Ultraviolet Lensless Microscopy: Development and Potential Applications to Semiconductor Metrology

Thesis directed by Professor Margaret M. Murnane and Henry C. Kapteyn

The development and integration of next-generation semiconductor devices is experiencing significant metrology challenges. These devices are ever more complex and three-dimensional in shape and contain ever more types of materials, with critical dimensions of only a few tens of nanometers, or even down to a few nanometers. The structure and composition of these devices, while critical to their overall performance, is extremely difficult to measure non-destructively. Thus, there is an urgent need for non-destructive nano-imaging techniques for general next-generation samples. In this thesis, I present the recent development of EUV lensless microscopy by combining the tabletop coherent extreme ultraviolet light sources based on high harmonic generation and the state-of-the-art computational phase retrieval algorithms (ptychography), as well as their potential applications to semiconductor metrology. In particular, I will present our work on designing and commissioning a tabletop EUV actinic microscope that is capable of performing at-wavelength EUV photomask imaging and defect inspection. We further demonstrated for the first time that fast, reliable and robust ptychographic imaging of periodic structures can be achieved by careful illumination design. This is both a critical advancement for the modern ptychography technique and a promising and economic solution for actinic EUV photomask metrology.

Dedication

To my parents Dongmei Song and Mingxing Wang, who brought me to this world and have been encouraging me to explore, to experience and to grow.

To my beloved wife, Jiaojiao Zhang, who makes our relationship the easiest and sweetest thing possible.

Acknowledgements

I am always and will be forever grateful for my time as a PhD student at the Kapteyn-Murnane group, at JILA and at CU because it gives me the opportunity to meet and learn from some of the brightest and kindest people. My sincere thanks goes to:

- Professor **Margaret Murnane** and **Henry Kapteyn** for being the best advisor in the universe for their invaluable guidance and advise for my academic development as well as their generous support during the hard times in life. This thesis would not have been possible without you. You are not just advisors, but also life-long friends and families (if I may).
- My best [friends + labmates + roommates], Nathan Brooks and Guan Gui, for accomplishing most of the work in this thesis together, for making my lab work and daily life so enjoyable and full of laughter, and most importantly for making me a better human being.
- My mentors in the Kapteyn-Murnane group, especially Dan Adams and Michael Tanksalvala, who taught me almost everything I know about lab work and coding, and constantly inspire me with their brilliance and passion.
- My labmates over the years, who made me feel at home from the very beginning and have been a joy to work with: Charlie Bevis, Robert Karl, Yuka Esashi, Zhe Zhang, Peter Johnsen, Iona Binnie, Nicholas Jenkins, Emma Cating-Subramanian, Chen-Ting Liao, Christina Porter, Elisabeth Shanblatt, Giulia Mancini.
- The other members of the Kapteyn-Murnane group, past and present: Drew Morril, Sinéad, Anya Grafov, Yingchao Zhang, Wenjing You, Xu Shi, Joshua Knobloch, Michael Gerrity,

Brendan McBennett, Emma Nelson, Quynh Nguyen, Christian Gentry, Travis Frazer, Nico Hernandez-Charpak, Oliver Shao, Na Li, Tika Kafle, Michaël Hemmer, Daniel Carlson, Will Hettel, Jeremy Thurston and many many more.

- Liam Weiner, Clayton Bargsten, Kevin Shea and Daisy Raymondson from KMLabs for helping with the laser systems.
- The experts in JILA Computing Team and Instrument Shop for solving every technical problems I have encountered.
- Professor Bob McLeod for being a great instructor in the 'Numerical Methods in Photonics' class.
- Mr Mike Brooks and Ms Cindy Brooks for being the kindest persons and treating me as a family member.
- The friends I have made during graduate school.

CONTENTS

Chapter

TABLES

Table

FIGURES

Figure

Chapter 1: Introduction

1.1 Opening Remarks

You can make things only if you can 'see' them well!

1.2 Photolithography and metrology

In 1965, Gordon Moore predicted that *the number of transistors per silicon chip doubles every year*, which has been widely known as *the Moore's law*. Photolithography was the major manufacturing technique that keeps the Moore's law alive. The root words *photo, litho, graphy* all have Greek origins, with meanings '*light*', '*stone*' and '*writing*' respectively. As suggested by the name, photolithography is a printing ('*writing*') technique that uses light to transfer geometric design patterns from photomasks (essentially master templates, '*stone*') to a layer of '*light*'-sensitive chemicals (photoresists) coated on the substrate. The photoresist either breaks down or hardens where it is exposed to light, and the patterns are then created by removing the softer parts of the photoresist with appropriate solvents. Subsequent etching, deposition or implantation operations can be performed to create complex 2D/3D geometric/compositional structures. Ever since the first introduction of the Moore's law nearly 60 years ago, an enormous amount of science and technology development and innovation in the field of photolithography has been made to keep driving the Moore's law. It has been associated with dramatic decrese in the size of components used in integrated circuits (ICs), a process which is often refered to as "scaling". Scaling has yielded a wide range of powerful and intelligent electronic devices that power our modern society. However, what comes with it is the complexity of these devices in terms of structure and composition, which makes the fabrication processes more and more challenging. For

example, by 2024 the gate length of ICs is projected to be 6 nm and instead of being planar structures, and the gate will wrap around vertically stacked nanowires.

	CD-SEM	Scatterometry	3D AFM	CD-SAXS	TEM
Underlying physics	Electron beam–matter interaction	Light scattering from periodic structures	Surface force–tip interaction	X-ray scattering from electron density spatial variations of about 0.1 nm for average structures, depending on SNR	Electron beam–matter interaction
Resolution (lateral and vertical)	Focusing capability of about 0.3 nm	Model-dependent; about 1 nm, vertical and lateral	<0.01 nm vertical; <1 nm lateral		0.05 nm lateral
Range (field of view)	50 nm to 10 mm	10 μm and larger; dependent on spot size	Tens of nanometres to>500 μm depending on scanner	50–200 μm	Tens of micrometres at low resolution
Advantages (for a hypothetical 5 nm patterned line)	Local and global information; sub-nanometre-level measurement accuracy	Non-scanning (that is, fast); non-destructive; in-line compatibility	Full 3D and limited sample preparation, in-line compatibility; nanometre-level measurement accuracy	Measures ensemble averages for large array; high resolution; larger angles as periodicity gets smaller; Fourier transform calculation is fast	Cross-sectional imaging capability for whole line imaged at atomic resolution; in-line compatibility
Current instrument limitations (for a hypothetical 5 nm patterned line)	Drift; vibration; contamination; beam damage; lack of sub-nanometre beam placement accuracy; information volume must be folded into size or shape determination	Inapplicable to isolated lines; spot size should underfill line arrays	Tip size (dense structures); relatively slow; aspect ratio (such as increased fin height or reduced fin pitch)	Compact X-ray sources limit throughput; scattering interaction is weak; inapplicable to isolated lines	Sample needs to be cross-sectioned (therefore destructive); beam projection artefacts and noise; relatively small high-resolution field of view
Ultimate limitation due to underlying physics	Electron beam wavelength	Non-uniqueness of solutions for inverse light scattering problem	Tip size; difficult to interpret tip–sample interaction in small confined spaces such as contact holes	Interaction volume is small	Electron beam wavelength; beam steering errors
SI length traceability	Calibration samples; displacement interferometry	Calibration results are non-transferable; uncertainty budget challenged owing to geometry approximations	Calibration samples; displacement interferometry	Calibration samples; traceable translation of detector	Lattice information from X-ray diffraction (short traceability path)
Key error sources	Drift; vibration; contamination; electromagnetic fields	Parametric correlation; geometry parametrization; unfitted parameters (for example, pitch)	Tip induced artefacts; tip/sample interaction interpretation	SNR; shape models that cannot fit the correct solution; uniqueness of solution for noisy data or sample structure is unknown	Lens aberration; sample preparation; beam damage (material dependent)
Potential improvements	Very low electron energy variation; displacement laser interferometry; elimination of electron-beam-induced contamination; dose rate management	Spot size; target area reduction for more in-die placement; hybridization	Scanning speed; better modelling of tip–sample interaction	Higher brightness X-ray sources; higher coherence of X-ray source	Electron dose management; improved sample preparation techniques

Figure 1.1: A overview of semiconductor dimensional metrology methods. Figure adapted from [1].

Metrology is the art of measuring tiny structures. It involves measurements of any sample properties of interest and helps illustrate structure-function relationships, and is needed in almost all aspects of IC research and development, integration, manufacturing process control and testing. Semiconductor metrology challenges include but are not limited to measurement of critical dimensions (size and shape), surface and interface properties, line edge/width roughness, layer structure of complex material stacks, chemical composition, strain, material dielectric interfaces. Almost all the dimensional, compositional and interconnect parameters for complex 3D structures, such as gate-all-around (GAA) nanowires, have to be precisely determined. As devices shrink in size (approaching the atomic scale) and become more three-dimensional (3D) in architecture, the relative importance and complexity of metrology increase accordingly. This requires instruments with a wide range of underlying physics including electrons, light in a wide range of frequency (visible, deep ultraviolet, extreme ultraviolet, and x-ray), and surface forces.

Here, we briefly review some key dimensional metrology techniques that are widely used in semiconductor manufacturing industry, as summarized in Fig. 1. Specialized critical dimension scanning electron microscopes (CD-SEMs) are one of the most versatile techniques used for in-line measurements, using a finely focused electron beam to scan over the samples [2,3]. It provides top-down images with critical dimensional parameters such as linewidth, line shape, edge roughness, and contact holes, etc. with sub-nanometer-level accuracy, as shown in Fig. 1.2. Major current limitations include lacking quantitative depth- or chemical-sensitivity and e-beam-induced sample damage and carbon contamination. Critical dimension small-angle X-ray scattering (CD-SAXS) [4] is a variable angle, transmission SAXS measurement where X-rays scattered from a periodic structure are analyzed to non-destructively determine the average shape of the nanostructure, see Fig. 1.3. It can be used to determine parameters such as sidewall angle,

linewidth, pitch and roughness. The primary limitation for CD-SAXS is the brightness of available compact high-energy X-ray sources (> 17 keV), which results in low measurement throughput. Scatterometry [5] is a non-imaging optical technique that allows sub-nanometer model-based measurements of overlay effects [6], geometric critical dimensions and optical constants of patterned arrayed structures, see Fig. 1.4. It is the metrology workhorse for determining CDs owing to the high measurement speed. However, as the modeling/fitting is an inverse problem without a unique solution, sometimes it suffers from inherent ambiguities associated with multi-variable correlation. Transmission electron microscopes (TEMs), mainly operating in two modes – high resolution TEM and high-angle-annular-dark-field (HAADF) scanning TEM, provide unprecedent resolution of about 0.05 nm [7] and is useful for current and future IC device metrology, see Fig. 1.5. However, the main limitation is that it is destructive as most samples need to be cross-sectioned and thinned down to below 100 nm, which precludes certain applications. Atomic force microscopes (AFMs) are well-suited for surface topography measurement with sub-nanometer resolution by positioning a small physics tip (< 10 nm radius) to interact with the surface, see Fig. 1.6 [8,9]. However, it is only used in niche applications or where faster options are unsuitable because it is slow and does not meet the speed requirement in IC high volumn manufacturing (HVM).

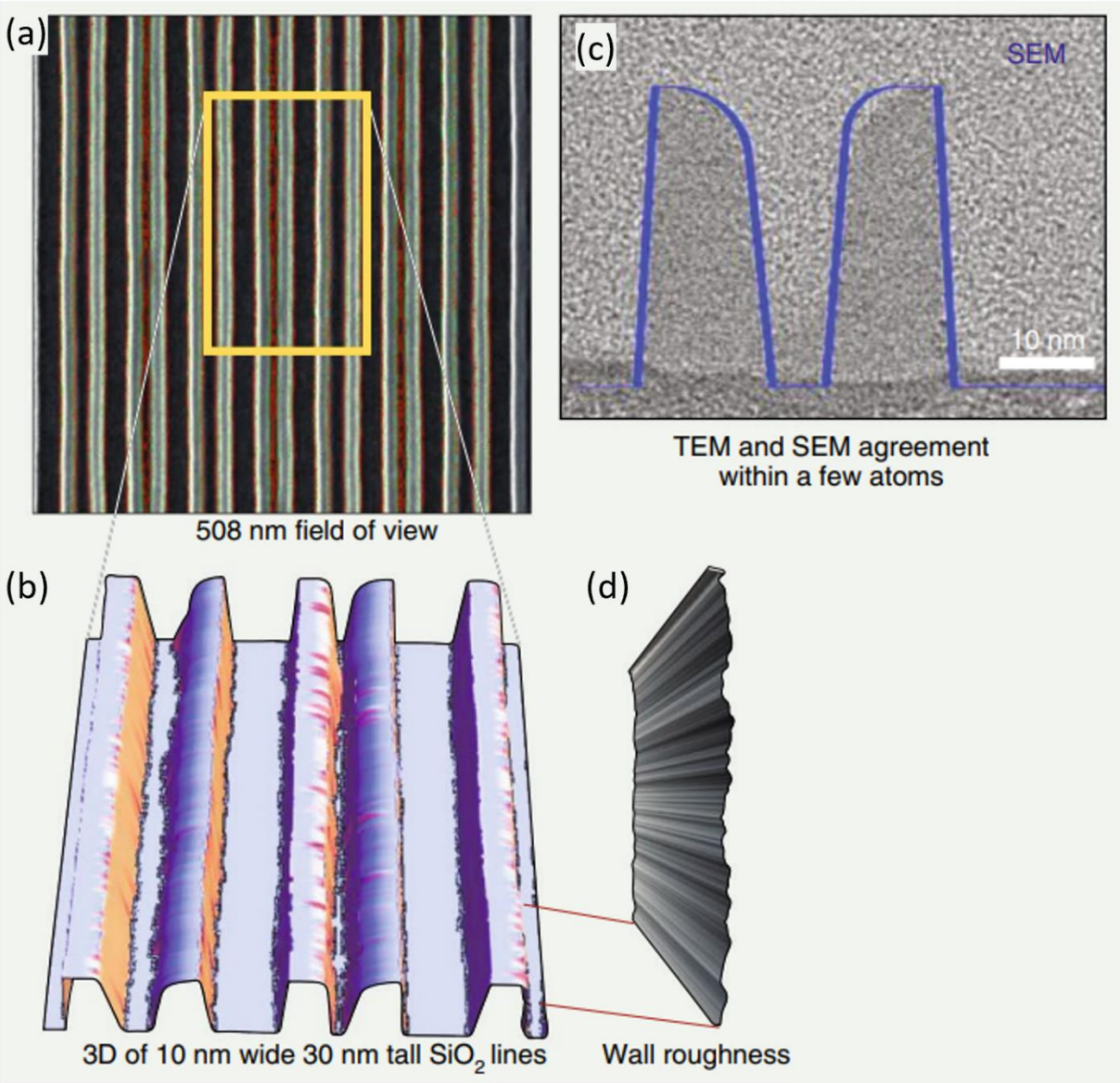

Figure 1.2: Accurate, model-based 3D measurements of size, shape and roughness of 10 nm FinFET structures using CD-SEM. (a) A top down CD-SEM image. **(b)** Model-based 3D rendering from images taken from multiple beam angles. **(c)** Profile of the modelled SEM image overlaid with a TEM cross-section image showing great agreement. **(d)** Sidewall roughness of model-based 3D image. Figure is adapted from [1].

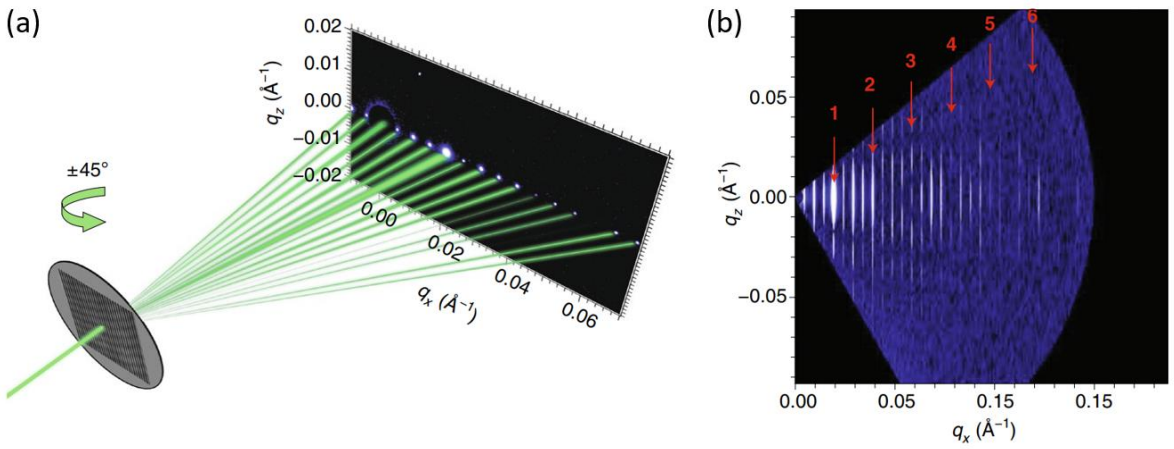

Figure 1.3: Small angle x-ray scattering. (a) Schematic diagram showing variable angle CD-SAXS on a periodic structure. **(b)** An example scattering pattern obtained from a pitch quartering sample. The red arrows mark the peaks from the nominal spacing, and other peaks are superlattice peaks from the pitch quartering. Figure is adapted from [10].

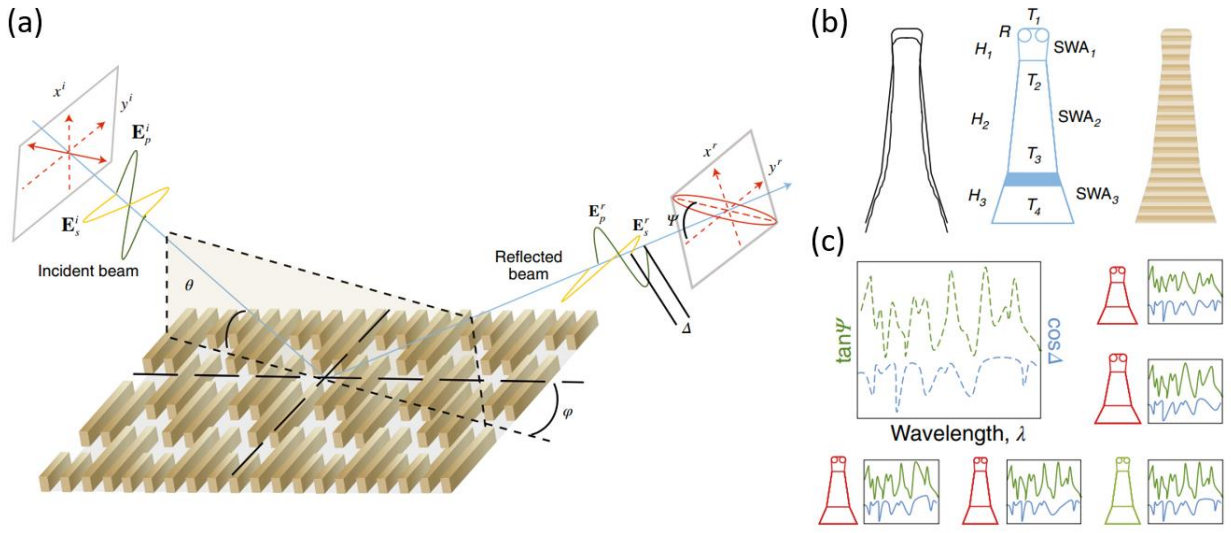

Figure 1.4: Optical scatterometry. (a) Schematic of optical scatterometry on 3D fin structures. **(b)** Three schematics showing a cross-section of a fin, its geometric parameterization and its segmenting for electromagnetic simulation. **(c)** Schematic of experimental data and library fitting. Figure is adapted from [1].

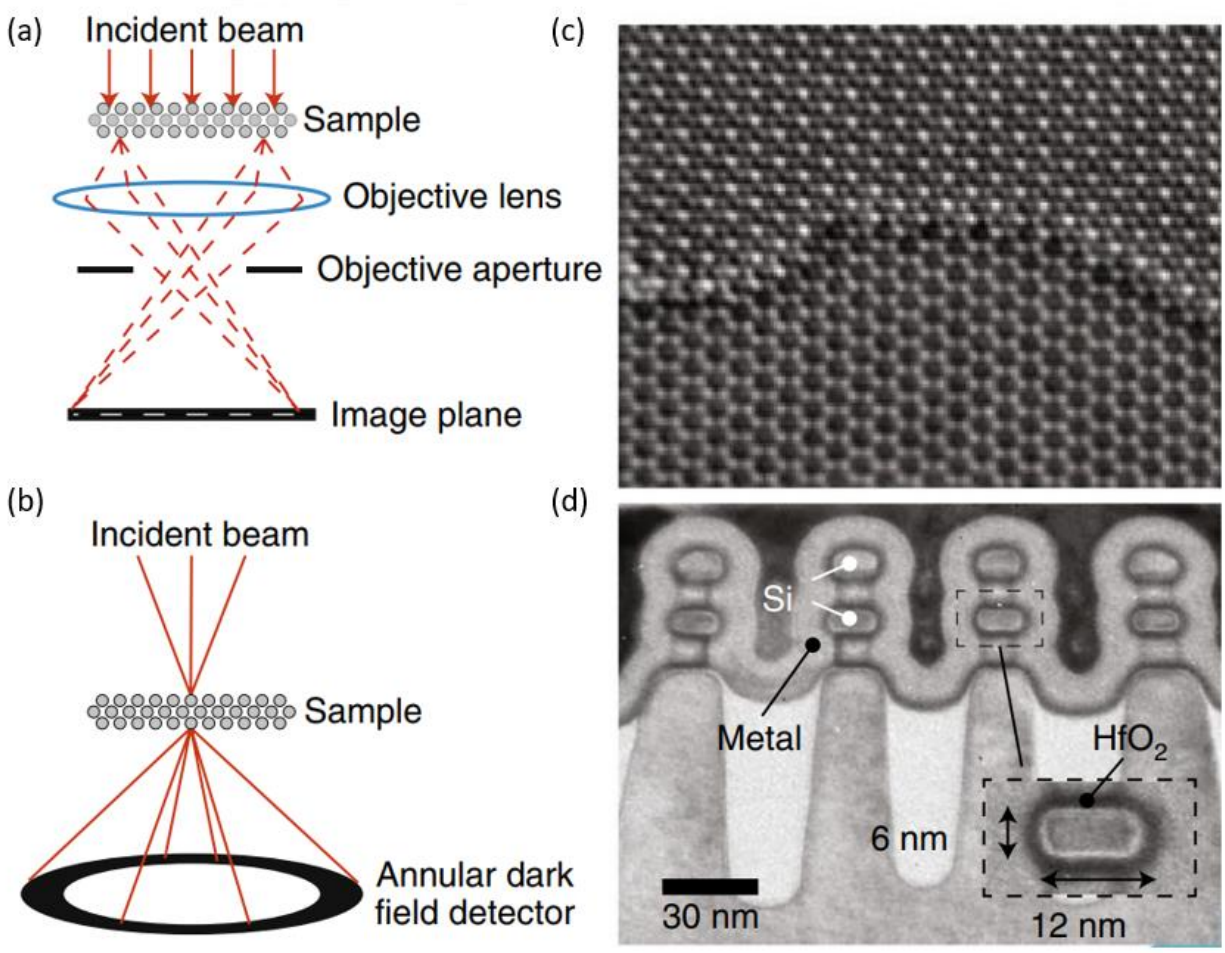

Figure 1.5: Transmission electron microscopy. (a, b) Schematic diagrams of high resolution TEM **(a)** and high-angle-annular-dark-field scanning TEM **(b)**. **(c)** Exit wave phase image of double-layer graphene reconstructed using a series of high resolution TEM through-focal lattice images. **(d)** TEM images of GAA silicon nanosheets. At this length scale whole devices can be imaged, though not with atomic resolution. Figure is adapted from [1].

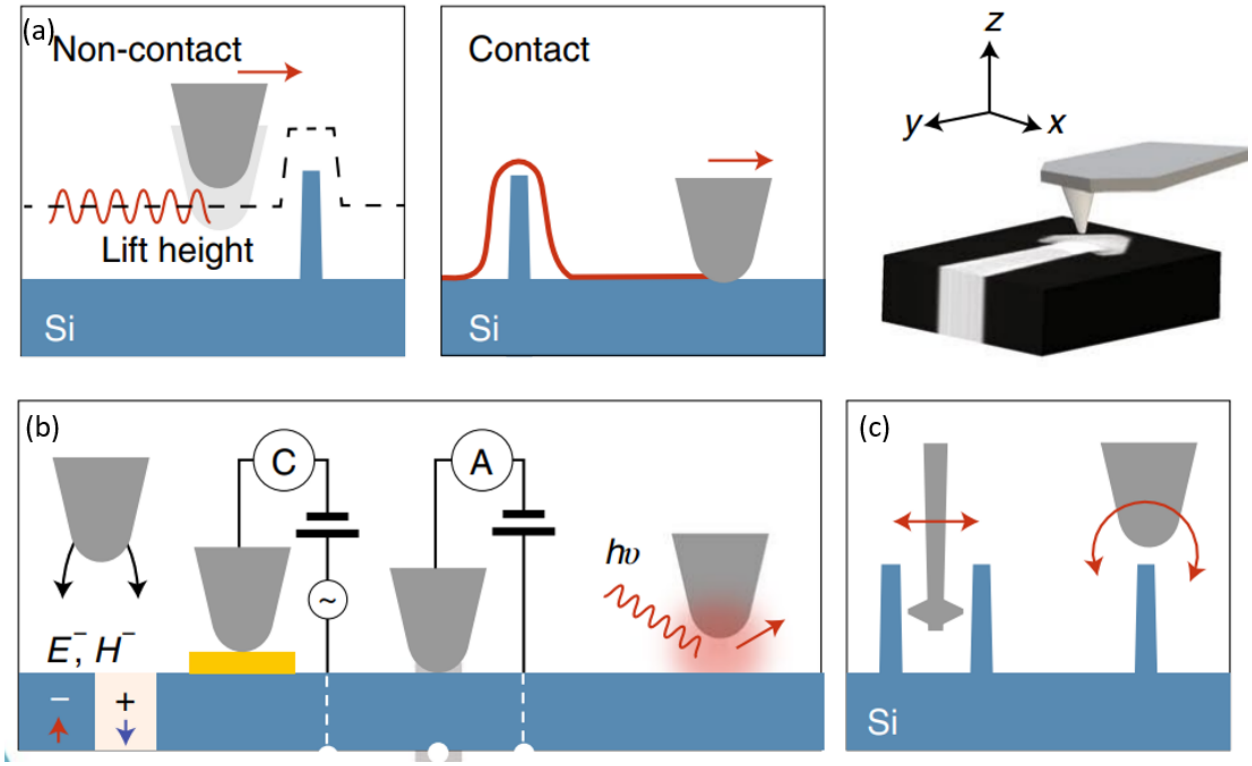

Figure 1.6: (a) Schematic representations of the basic principles of operation for AFM modes. A nanosized tip is used to sense the surface by non-contact or contact tip–sample interaction. (b) Long-range forces including electric and magnetic fields can be measured by studying the frequency changes in an oscillating tip, while local electrical properties such as capacitance or resistance are measured when the tip is in direct contact with the biased sample. In addition, near-field optics techniques are used to explore chemical mapping and optical properties with nanometre precision. (c) , the conventional sensing scheme of AFM has been modified by dedicated tip geometry (that is, T-shaped apex) and tilting scan heads for advanced process monitoring of fins (for example, sidewall and edge roughness). Figure is adapted from [1].

The recent integration of EUV lithography into semiconductor HVM introduces new metrology challenges. First of all, as device features reach 1-10 nm, their functional properties are no longer well-described by macroscopic models because imperfections such as surface/interface roughness and oxide layers have thickness in this regime, and therefore begin to have a considerable impact on their properties and performance in multilayer structures [11,12], metal oxide semiconductor

field effect transistors (MOSFETs) [13,14], and EUV photomasks [15,16]. Non-destructive (or even better, in-situ) measurement in working devices will be critical to further understanding this surface- and interface-dominated effects and optimizing the synthesis and integration of these devices. Secondly, all optics used in EUV lithography are reflective surfaces with Si/Mo alternating multilayers as high reflectors at the 13.5 nm wavelength. Small particles embedded beneath the multilayer coatings will result in small bumps in the multilayer structures, which do not affect the reflectivity but do change the phase delay at the defect position – meaning phase-only defects. Unfortunately, most current metrology techniques are not sensitive to this type of phase defects. Last but not least, actinic patterned EUV photomask metrology tools, meaning using the same 13.5 nm wavelength for inspection as for manufacturing, are extremely desirable due to the distinct contrast mechanisms for electrons and photons, and even for photons at different wavelength/frequency. For example, it has been demonstrated that defects on EUV photomasks detected by electron beams and deep ultraviolet light can result in no impact on the patterned wafer, and vice versa [17]. It has been considered to be a major remaining EUV photomask infrastructure gap.

Finally, I want to wrap up this section by pointing out that no single instrument has the full capabilities (such as resolution, speed, contamination/damage, uncertainty) needed to characterize the whole set of parameters of complex device structures, so multiple complementary tools need to be integrated to provide full understandings, and novel metrology techniques are always under investigation to enable new capabilities.

1.3 EUV as a powerful probe

Metrology tools are essentially instruments that uses some kind of probe to interact with a sample of interest and generate a detailed rendering of that sample, either spatially-resolved or compositionally-resolved or 3D-modeled etc., based on how the probe changed during the interaction. As discussed in the previous section, state-of-the-art semiconductor metrology tools use a wide variety of different probes, for example electrons and photons spanning an extensive range of wavelength, and even physical nano-tips, as each probe see different aspects of the sample due to the rich contrast mechanisms. In this thesis, we focus on making use of photons in a specific range in electromagnetic spectrum, i.e., the extreme ultraviolet (EUV), to develop novel and powerful metrology techniques that hopefully help address some of the challenges presented in the previous section.

Photons in the EUV – wavelength between 10 nm and 100 nm - is recognized as a powerful probe for three primary benefits. First, its short wavelength, compared to visible and DUV light, enables higher spatial resolution for microscopy within the diffraction limit, $\lambda/2NA$, where λ is the probe wavelength and NA is the numerical aperture of the imaging system. Numerical aperture is a dimensionless number measuring the 3D collection angle of an imaging system, typically below a value of 1, which means a traditional imaging system can typically achieve spatial resolution equal to half the wavelength of the illumination at the best. A host of interesting nanoelectronic semiconductor devices has length scales close to the wavelength of EUV light, making it a natural probe for metrology [18-20]. Second, elemental absorption edges are densest in this wavelength range, providing a natural and high contrast mechanism for emelental composition [21]. This compositional sensitivity has been experimentally demonstrated to be powerful and promising [19,20,22]. Thirdly, like x-rays, the photon energy of the most commonly used EUV light (< 40

nm) is far away from interatomic bond resonances. This allows one to simply calculate the index of refraction for any compound material from atomic scattering factors, $f_1(\lambda)$ and $f_2(\lambda)$, of the elements present in that material, which is in contrast to visible light wherein the index of refraction often must be experimentally determined for each compound due to the complex molecular bonding structures. Specifically, the wavelength-dependent index of refraction in the EUV can be represented as:

$$n(\lambda) = 1 - \delta(\lambda) - i\beta(\lambda), \qquad (1.1)$$

where $\delta(\lambda) = n_a r_e \lambda^2 f_1(\lambda)/(2\pi)$ and $\beta(\lambda) = n_a r_e \lambda^2 f_2(\lambda)/(2\pi)$ [23].

For the experimental demonstrations in this thesis, we mostly used EUV photons at 56 nm, 30nm and 13.5nm wavelength.

1.4 EUV microscopy

Microscopy is the technical field of using various kinds of microscopes to form images of samples of interest that cannot be seen with naked eyes. Forming images in the EUV/x-ray region is not as straightforward as in the optical wavelength because of the lack of suitable refractive lenses. Here, we briefly review the efforts in developing EUV/x-ray microscopy techniques.

The simplest method to for an image with EUV/x-ray is to record the shadow of the object, as done in medical x-ray imaging – radiography, see Fig. 1.7. Radiography provides information about the distribution of absorbing materials with millimeter-scale spatial resolution.

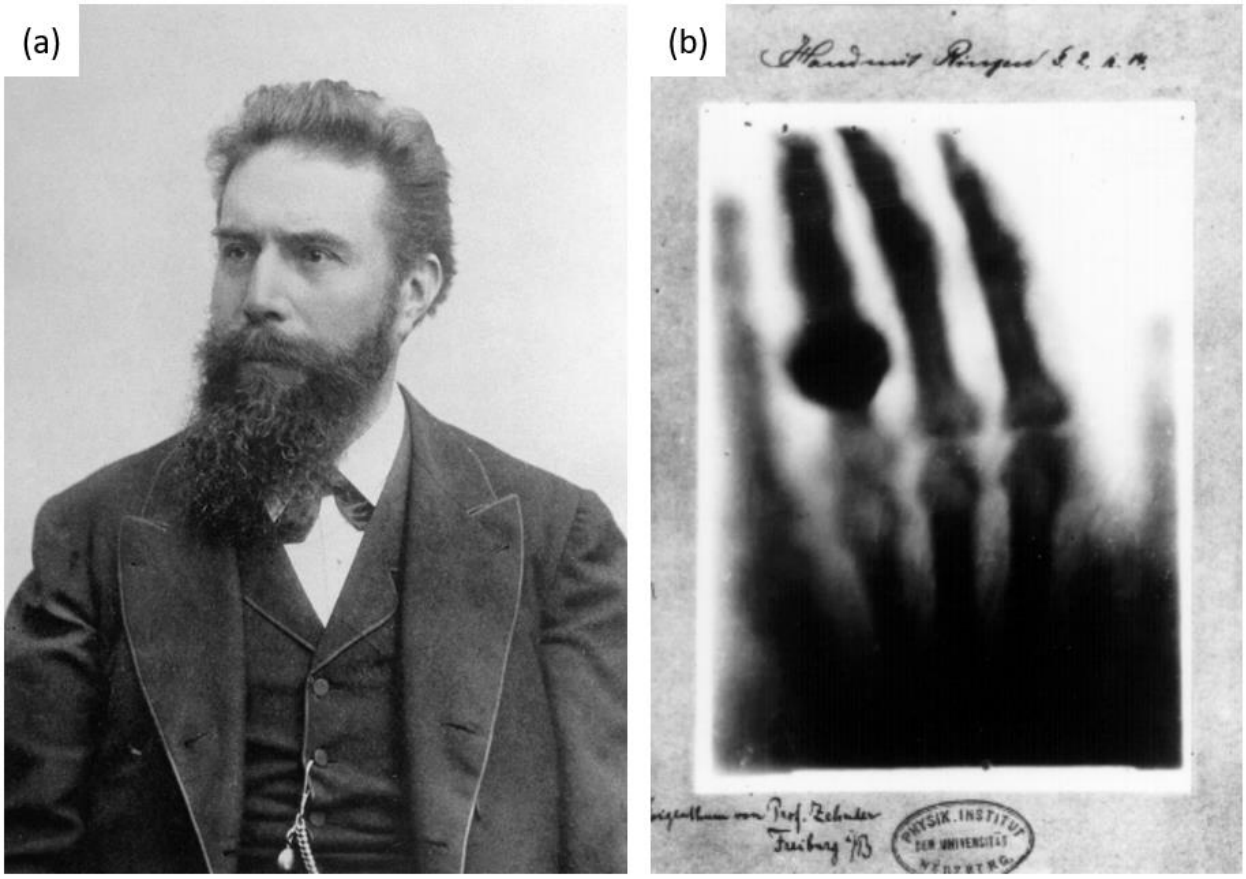

Figure 1.7: One of the first x-ray photographs, taken by the German physistist Willhelm Conrad Röntgen **(a)** showing his wife's hand **(b)**. Figure adapted from [24].

Imaging resolution can be improved by using small apertures. The small aperture is placed directly in front of the sample to form a small beam on the sample, which is then raster scanned to form an image with the resolution dependent on the aperture size [25]. In the case of coherent illuminations, Fourier transform holography was developed [26] to image nanostructures with down to 50 nm resolution [27], as shown in Fig. 1.8. In Fourier transform holography, the light from the small aperture acts as a reference beam and interferes with the diffraction from the sample area and forms intensity modulations, which is then Fourier transformed to obtain an image of the sample. The resolution of Fourier transform holography is proportional to the size of the aperture. Increasing

resolution is challenging because as the aperture becomes smaller, more photons are blocked in the reference beam, diminishing the signal-to-noise ratio in the interference fringes.

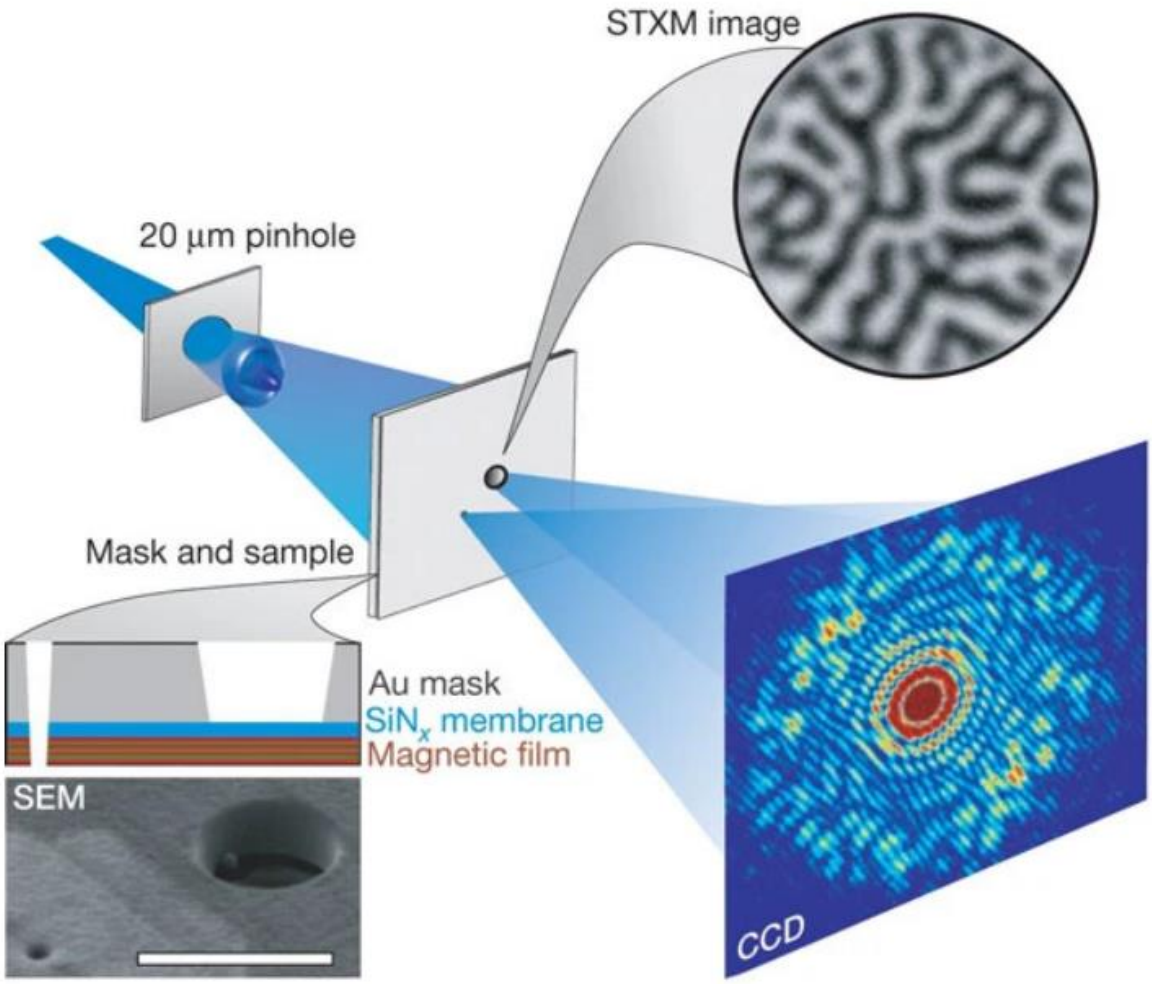

Figure 1.8: Fourier transform holography enables imaging of magnetic structures with 50 nm resolution. In Fourier transform holography, a small aperture is added besides the sample, which creates a reference beam that interferes with the diffraction from the sample area. The interference is recorded on a detector as intensity modulations. A Fourier transform of the intensity image results in an high resolution image of the sample. Figure adapted from [27].

The application of focusing mirrors to EUV/x-ray was pioneered at Stanford by Kirkpatrick and Baez [28]. They used two superpolished substrates, each with either a parabolic or elliptical

curvature, see Fig. 1.9(a). The curved substrates are able to focus a glancing incident x-ray beam and are known as K-B mirrors. The glancing incident angle is needed for high reflectivity. Another mirror geometry, the Schwarzschild configuration, uses multilayer spherical mirrors to focus the beam, see Fig. 1.9(b) [29,30]. Multilayer mirrors are layered structures designed such that only a select bandwidth of radiation is reflected. The use of two mirrors in a proper design, can reduce the astigmatism from spherical surfaces [31,32]. Reflective focusing mirrors do not require coherence, but some other optical focusing elements do, *i.e.*, the Fresnel zone plate and the Laue lens. The Fresnel zone plate consists of a series of concentric rings, designed such that constructive interferences happen at some spots on the optical axis, effectively forming some focus spots, see Fig. 1.9(c). The focus spot size is limited by the fabrication quality, especially the outer most rings. The Laue lens can be thought of a 1D zone plate, creating a 1D focus as tight as 8 nm [33], see Fig. 1.9(d).

The ability to focus EUV/x-rays leads to point scanning microscopy techniques. Zone-plate-based point scanning microscopy techniques have achieved 30 nm resolution [34]. Fresnel zone plates also allow direct image formation, and 10 nm resolution has been achieved [35]. A combination of K-B mirrors and Fresnel zone plates has demonstrated 5 nm spot size [36]. Furthermore, quantitative phase information is possible by analyzing the intensity changes between adjacent scanning points [37].

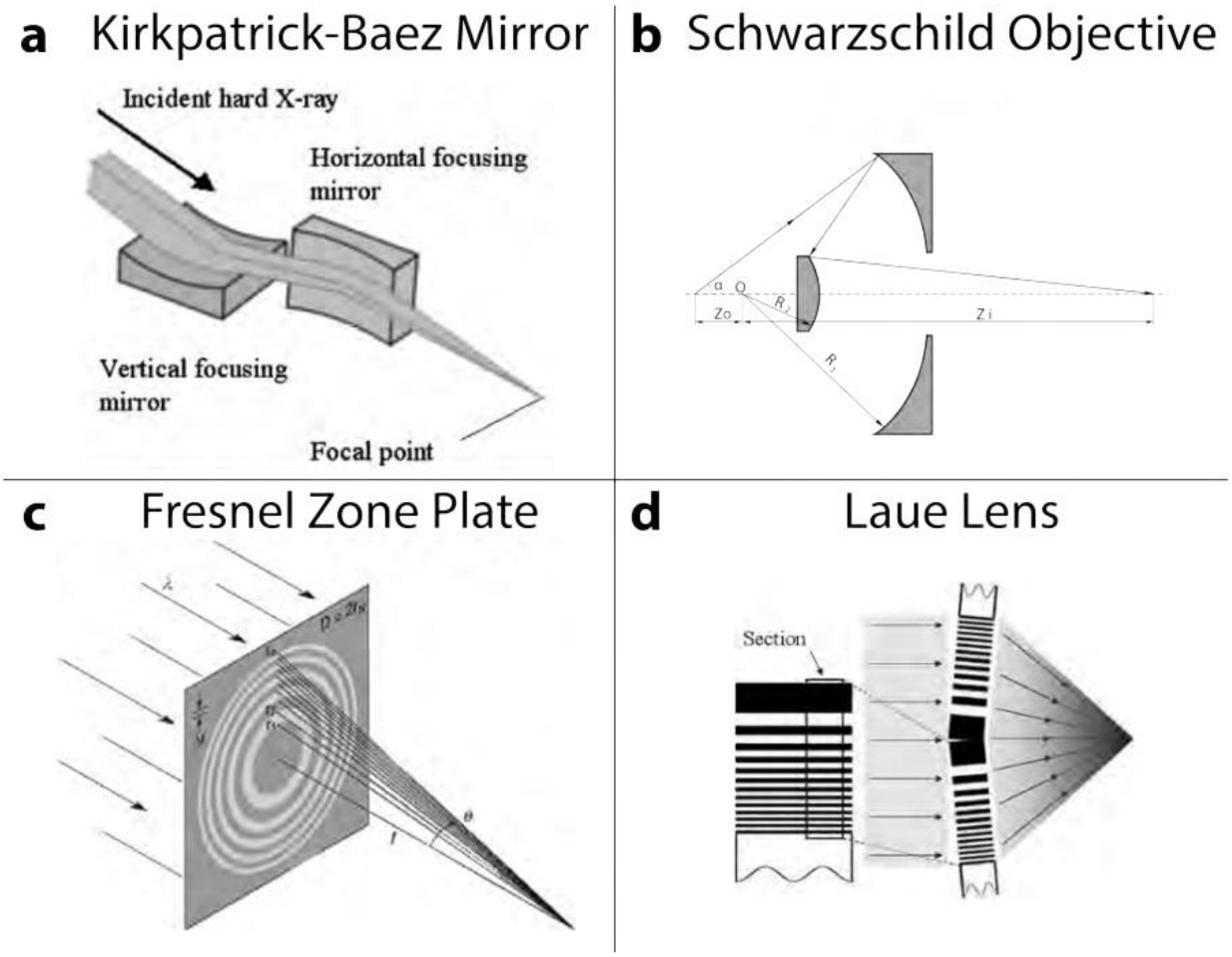

Figure 1.9: Focusing optics in EUV/x-ray. (a) The Kirkpatrick-Baez mirror that consists of two superpolished substrate with parabolic or elliptical curvature. **(b)** The Schwarzschild objective consists of two spherical mirrors with multilayer coatings. **(c)** The Fresnel zone plate is a diffractive element consisting of concentric rings with certain widths and distances. **(d)** The Laue lens is a diffractive element that can form a line focus from sputtered layers of materials. Figure adapted from [39].

So far, the imageing techniques reviewed above rely on either using some image-forming optics to directly form images of the samples or using focusing optics to obtain a small focus spot and then forming images through point scanning. This leads to severe limitation on the microscope performance by the quality and cost of these optical elements. On the contrary, the image forming

technique used in this thesis, i.e., coherent diffractive imaging (CDI), does not require any image forming optics, which makes it the most photon efficient for of imaging [38]. It does require to focus the beam down to several microns, but the resolution is not limited by the spot size but by Abbe's diffraction limit, since it is not a point scanning method. Futhermore, both the amplitude and phase information of the sample can be determined, which enables us to better understand the light matter interactions. The theory and algorithms of CDI will be reviewed in the next section, and experimental demonstrations of CDI using coherent EUV beams will be discussed in Chapters 2-4.

1.5 Coherent diffractive imaging

Coherent diffractive imaging (CDI) is a microscopy technique that uses computational algorithms to replace traditional image forming optics, thus also known as lensless imaging. In CDI, a coherent beam, such as a light or electron beam, is incident on a sample of interest, and the intensity of the far-field diffraction patterns are measured on a pixel-array detector. During the measurement, only the amplitude information, that is the square root of intensity, of the far-field diffraction field is preserved, while the phase information is lost – the well-known phase problem. Some computational algorithms are then used to retrieve the lost phase from these amplitude measurements and some constraints and/or a prior knowledge, a process known as phase retrieval. With both the measured amplitude and retrieved phase information of the far-field diffraction filed, a complex-valued image of the sample can be calculated by back propagating the field from the detector plane to sample plane, which turns out to be a Fourier transform relationship.

Over the past two decades, CDI has exploded in popularity in the X-ray and EUV microscopy communities where high-quality image-forming optics are difficult and expensive to fabricate.

Since its first demonstration using coherent X-rays in 1998 [40], CDI has experienced revolutionary development and has found applications across wide fields such as material science [41-43], semiconductor metrology [44], biological science [45,46], etc. With the added benefits of diffraction-limited resolution and phase-contrast sensitivity, CDI is one of the instrumental tools driving the nanoscale microscopy revolution of the last decade. This chapter discusses the formulation of the phase problem and its solution as through iterative optimization.

1.5.1 Single diffraction pattern CDI

In the early stage of CDI, one is usually interested in retrieving the phase from a single diffraction intensity measurement, as in image recovery from speckle interferometry data in astronomy and from structure factors in crystallography. To mathematically formulate this single diffraction pattern phase retrieval problem, we use two complex-valued functions $f(x,y) = |f(x,y)| \cdot e^{i\eta(x,y)}$ and $F(u,v) = |F(u,v)| \cdot e^{i\psi(u,v)}$ to represent the wave field in the sample exit plane (that is immediately after the wave interacting with the sample) and the detector plane, respectively. Mathematically, they are related by a Fourier transform relationship with a normalization factor $\boldsymbol{C}$ *i.e.*,

$$F(u,v) = |F(u,v)| \cdot e^{i\psi(u,v)} = C \cdot \mathcal{F}[f(x,y)] = C \cdot \iint_{-\infty}^{+\infty} f(x,y) e^{-i2\pi(ux+yv)} dxdy, \qquad (1.2)$$

where (x,y) is a 2D spatial coordinate, and (u,v) is the corresponding 2D spatial frequency coordinate. One wishes to recover $\psi(u,v)$ given a measurement of $|F(u,v)|$ and some constraints or a prior information about $f(x,y)$. In practice, one deals with sampled data, assuming 2D square sampling grids, in a computer. The Fourier transform in Eq. (1.2) and its inverse are then replaced by the discrete Fourier transform and its inverse:

$$F(u,v) = C \cdot \sum_{x=0}^{x=N-1} \sum_{y=0}^{y=N-1} f(x,y) \cdot e^{-i2\pi(ux+yv)/N}, \qquad (1.3)$$

$$f(x,y) = C \cdot \sum_{u=0}^{u=N-1} \sum_{v=0}^{v=N-1} F(u,v) \cdot e^{i2\pi(ux+yv)/N}, \quad (1.4)$$

which are computed using the fast Fourier transform (FFT) algorithm.

Over the past 70 years, the initial ideas of phase retrieval have been adapted and expanded into a formulation as a non-convex optimization problem [47]. The proposed algorithms typically take the form of iterative projections (and sometimes reflections) onto constraint sets in the spatial space (or **real space**) and the spatial frequency space (or **reciprocal space**) where measurements are taken and/or a prior knowledge is known. This process is repeated iteratively until some convergence criteria is met. A brief introduction of these algorithms is given here. For a more detailed discussion, please refer to [48].

When formulating phase retrieval algorithms, it is useful to understand the following two concepts: *the constraint sets* and *the projector and reflector*.

The constraint sets: In the phase retrieval problem stated before, both the real space and the reciprocal space are involved. There are mainly two constraint sets, one in each space. The real space constraints can vary depending on the sample, the imaging system, and the algorithm in use, examples including the non-negativity of real space pixel value [49], constraints on the image histogram [47], or most commonly the support or isolation constraint $\boldsymbol{C_S}$ [50], which simply constraints that the object's pixel values are zero outside some defined support region $\boldsymbol{D}$. The reciprocal space constraint $\boldsymbol{C_A}$ is also known as Fourier modulus constraint, which constraints that the Fourier modulus of the solution is equivalent to the measurements.

The projector and reflector: The projector onto one constraint set is a mapping from a general guess image, v, onto an an image in the constraint set, ξ, such that $|\xi - v|$ is minimized [51]. This means that the guess image, v, is simply mapped to the closest point in the constraint set. For the support constraint, the support projector is given by

$$\boldsymbol{P_S}\{v\} = \begin{cases} v, & x \in \boldsymbol{D} \\ 0, & else \end{cases}. \quad (1.5)$$

For the Fourier modulus constraint, the projector includes first Fourier transforming v to the reciprocal space to form $\tilde{v} = \mathcal{F}\{v\}$, then replacing its amplitude with the measurement, $\widetilde{\boldsymbol{P}}_{\boldsymbol{M}}\{\tilde{v}\} = \sqrt{I} \cdot e^{i \cdot angle\{\tilde{v}\}}$, and finally inverse Fourier transforming it back to the real space, $\mathcal{F}^{-1}\{\widetilde{\boldsymbol{P}}_{\boldsymbol{M}}\{\tilde{v}\}\}$. Putting them all together, the Fourier modulus projector is given by

$$\boldsymbol{P_M}\{v\} = \mathcal{F}^{-1}\{\sqrt{I} \cdot e^{i \cdot angle\{\mathcal{F}\{v\}\}}\}, \quad (1.6)$$

where $\mathcal{F}$ and $\mathcal{F}^{-1}$ are the Fourier transform and inverse Fourier transform operations, $angle\{\}$ is an operation that takes the phase of the input, and I is the measured Fourier intensity distribution.

The reflector is a mapping that applies the same operation as the projection operation but moves twice as far. It can be constructed from the corresponding projector as follows

$$\boldsymbol{R_S}(v) = v + 2(\boldsymbol{P_S}\{v\} - v) = 2\boldsymbol{P_S}\{v\} + v, \quad (1.7)$$

$$\boldsymbol{R_M}(v) = v + 2(\boldsymbol{P_M}\{v\} - v) = 2\boldsymbol{P_M}\{v\} + v, \quad (1.8)$$

Within this formalism, the phase retrieval problem is equivalent to finding a solution v that is an element of the union between the two constraint sets $\boldsymbol{C_S}$ and $\boldsymbol{C_A}$. For the solution to be unique, the constraint sets must be non-convex and must intersect at only one point. The solution is found by starting from a random guess and iteratively projecting between the constraint sets, as shown in Fig. 1.10.

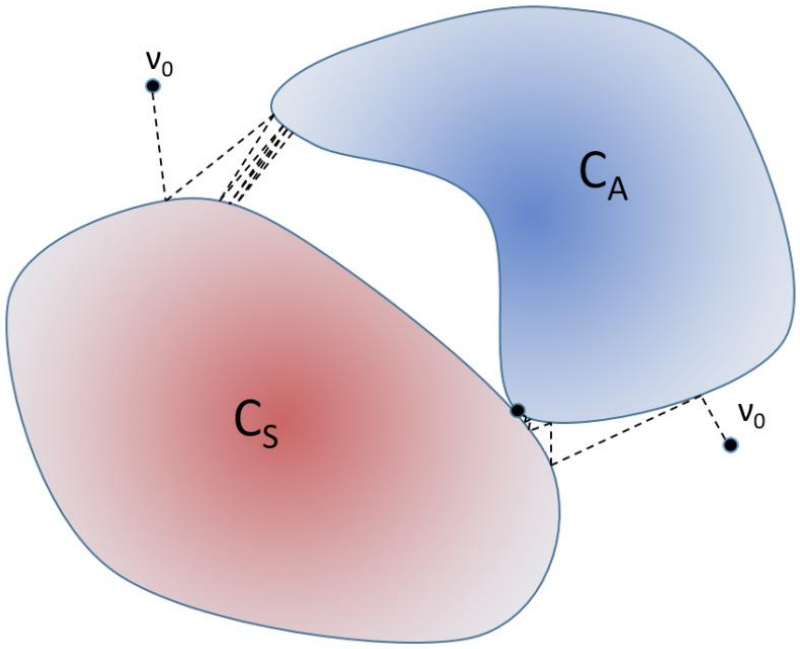

Figure 1.10: A schematic representation of alternating projection algorithms for phase retrieval. The algorithm starts from an initial random guess, v_0, and is iteratively projecting onto the support constraint C_S and the Fourier modulus constraint C_M to find a global minimun solution. Figure adapted from [52].

Several algorithms based on these concepts have been proposed and demonstrated. We will now summarize some commonly used projection algorithms in Table 1 and provide visual representations of their characteristic behavior for intuitive understanding.

Table 1: Summary of various phase retrieval algorithms.

Algorithm	Iteration update formula $v^{(n+1)} =$
ER	$\boldsymbol{P_S P_M}\{v^{(n)}\}$
SF	$\boldsymbol{R_S P_M}\{v^{(n)}\}$
HIO	$\begin{cases}\boldsymbol{P_M}\{v^{(n)}\}, & v^n \in \boldsymbol{D} \\ (\boldsymbol{I}-\beta\boldsymbol{P_M})\{v^{(n)}\}, & v^n \notin \boldsymbol{D}\end{cases}$
DM	$\left(\boldsymbol{I}+\beta\boldsymbol{P_S}\left((1+\gamma_s)\boldsymbol{P_M}-\gamma_s\boldsymbol{I}\right)-\beta\boldsymbol{P_M}\left((1+\gamma_M)\boldsymbol{P_S}-\gamma_M\boldsymbol{I}\right)\right)\{v^{(n)}\}$
RAAR	$\left(\frac{1}{2}\beta(\boldsymbol{R_S R_M}+\boldsymbol{I})+(1-\beta)\boldsymbol{P_M}\right)\{v^{(n)}\}$

The first algorithm called *error reduction* (ER) (Gerchberg-Saxton [53,54]) is

$$v^{(n+1)} = \boldsymbol{P_S P_M}\{v^{(n)}\}, \tag{1.9}$$

which tries to find a solution by projecting back and forth between two constraint sets, as illustrated in Fig. 1.11(a). The *solvent flipping* (SF) algorithm replaces the support projector $\boldsymbol{P_S}$ with its reflector $\boldsymbol{R_S}$:

$$v^{(n+1)} = \boldsymbol{R_S P_M}\{v^{(n)}\}, \tag{1.10}$$

to improve the convergence speed, as shown in Fig. 1.11(b). The *hybrid input-output* (HIO) algorithm is based on a nonlinear feedback control theory and can be constructed as:

$$v^{(n+1)} = \begin{cases}\boldsymbol{P_M}\{v^{(n)}\}, & v^{(n)} \in \boldsymbol{D} \\ (\boldsymbol{I}-\beta\boldsymbol{P_M})\{v^{(n)}\}, & v^{(n)} \notin \boldsymbol{D}\end{cases}, \tag{1.11}$$

where $\boldsymbol{I}$ is the identity operator, and β is a hyperparameter controlling the feedback strength, as shown in Fig. 1.11(c). The *difference map* (DM) is a general set of algorithms [47] that requires 4 projections, see Fig. 1.11(d):

$$v^{(n+1)} = \Big(\boldsymbol{I} + \beta \boldsymbol{P_S}\big((1+\gamma_s)\boldsymbol{P_M} - \gamma_s \boldsymbol{I}\big) - \beta \boldsymbol{P_M}\big((1+\gamma_M)\boldsymbol{P_S} - \gamma_M \boldsymbol{I}\big)\Big)\{v^{(n)}\}, \quad (1.12)$$

where β, γ_M, γ_S are feedback parameters and it is suggested in [47] that the optimal combination is $\gamma_M = \beta^{-1}$ and $\gamma_S = -\beta^{-1}$. Finally, the *relaxed averaged alternating reflector* (RAAR) algorithm [55] corresponds to:

$$v^{(n+1)} = \Big(\tfrac{1}{2}\beta(\boldsymbol{R_S R_M} + \boldsymbol{I}) + (1-\beta)\boldsymbol{P_M}\Big)\{v^{(n)}\}. \quad (1.13)$$

It is widely believed that RAAR is one of the most powerful phase retrieval algorithms. For $\beta = 1$, HIO and RAAR coincide.

The first experimental demonstration of CDI using x-ray was not until 1999 by Miao *et al.* [56]. Miao reconstructed a pinhole sample (gold dots on a silicon nitride film) using 1.7 nm light at normal incidence in transmission geometry, using essentially HIO algorithm and reporting 75 nm resolution. The long delay between the proposal of phase retrieval and its experimental demonstration using x-rays was ecidence of the weakness of single diffraction pattern CDI algorithms, expecially in the presence of experimental uncertainties. Furthermore, the phase retrieval algorithms presented above are only capable of reconstructing exit surface waves – which are complex-value wave fields immediately after the interaction between the illumination and the sample, not the sample image itself. This could potentially result in some issues in cases where the illumination is not uniform and has complicated structures. Luckily, these limitations can be overcome by a more robust and powerful extension of CDI called ptychography, which is the focus of this thesis and will be introduced in the next section.

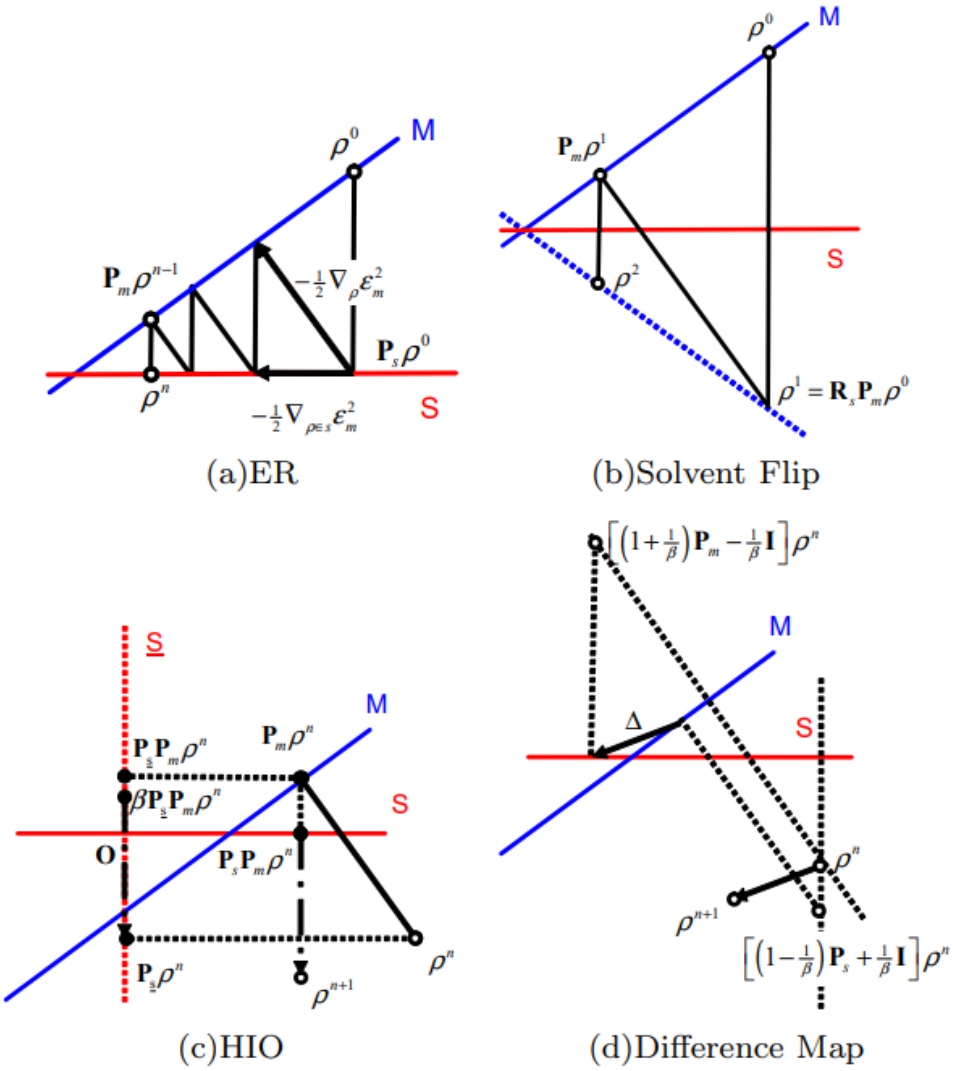

Figure 1.11: Geometric representation of various projection algorithms using the most simplified version of the constraint sets: two intersecting straight lines. (a) Error reduction algorithm: it starts from a point on the modulus constraint by assigning a random phase to the diffraction modulus and iteratively projects onto the two constraint sets. **(b)** The solvent flipping algorithm replaces the support projector with its reflector to increase convergence speed. **(c)** Hybrid input-output algorithm. **(d)** Difference map algorithm. Figure adapted from [48].

1.5.2 Ptychography

Ptychography is a coherent diffractive imaging technique that has revolutionized EUV and X-ray imaging in the last decade. The basic principal of ptychography was originally proposed as a method of calculating the phase of the Bragg peaks from a crystal by Hoppe *et al.* in 1969 [57]. The idea was then re-visited and demonstrated to improve spatial resolution in transmission electron microscopy by Nellist, Chapman and Rodenburg in 1995 [58]. In 2004, it was adapted in the optical microscopy community to image with short-wavelength light [59], and substantially extended in 2009 to include probe deconvolution, such that complex images of both a sample and the beam illumination are returned [60,61]. Since the early 2000s, ptychography has proven robust enough to handle real-world experimental conditions/uncertainties using both facility-scale and tabletop EUV and X-ray sources ([20,44,62-64] are but a few examples; more works are reviewed in [65]). Indeed, many of the STXM beamlines at facility-scale sources have been upgraded to have ptychography capability in the last 10 years because the necessary experimental hardware is essentially identical other than the detector (which can be a bucket detector for STXM but must be a pixel array camera for ptychography).

In ptychography, instead of taking a single diffraction pattern on spatially confined samples, the illumination beam is scanned across spatially extended samples in an area-by-area manner, as oppose to point-by-point scanning, and diffraction patterns are collected at each scan position. During the scanning, a significant amount of area overlap between adjacent scan positions is maintained, which creates a large amount of information redundancy to enable fast, robust and high-quality image reconstruction through phase retrieval. Furthermore, this information redundancy also allows to decouple the illumination function and the sample transmittance/reflectance function. The mathematical formulation is decribed below:

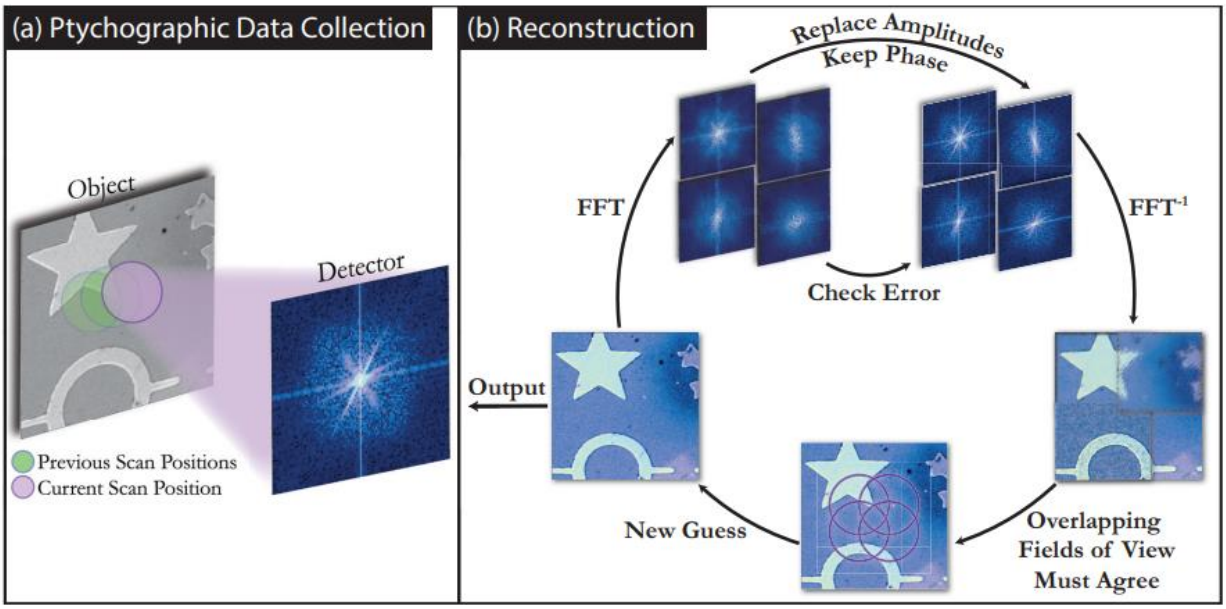

Figure 1.12: Ptychography data collection and reconstruction. (a) A schematic showing the ptychography data taking procedure, where a coherent illumination is scanned across a sample and diffraction patterns are measured at each position. (b) A schematic showing the ptychography data reconstruction procedure. Figure adapted from [66].

Data taking in ptychography:

When taking ptychography datasets, we collect a series of far-field diffraction intensity patterns at a set of J known positions, $\vec{r}_j = (x_j, y_j)$ for $j = 1,2, \dots, J$. At each scan position, we assume that the exit surface wave (ESW) can be modelled as the product of the complex-valued illumination function, $p(x, y)$ called the *probe*, and the shifted sample transmittance or reflectance function, $o(x - x_j, y - y_j)$ called the *object*:

$$\psi_j(x, y) = p(x, y) \cdot o(x - x_j, y - y_j). \quad (1.14)$$

This is valid for samples in which the beam does not significantly diffract, which is equivalent to obeying the first Born approximation. The ESW then propagates (and diffracts) in the free space between sample and detector:

$$\Psi_j(u,v) = \mathcal{P}\{\psi_j(x,y)\} = \mathcal{P}\{p(x,y)\cdot o(x-x_j, y-y_j)\}, \quad (1.15)$$

where $\mathcal{P}$ is a propagator and usually takes the form of Fresnel or Fraunhoffer propagation.The detector measures the intensity distribution as (Fig. 1.12(a))

$$I_j(u,v) = \left|\Psi_j(u,v)\right|^2 = \left|\mathcal{F}\{P(x,y)\cdot O(x-x_j, y-y_j)\}\right|^2. \quad (1.16)$$

Image reconstruction in ptychography:

Similar to the single diffraction pattern CDI algorithms discussed in section 1.5.1, ptychography phase retrieval algorithms alternatively projects a guess solution onto real and reciprocal spaces where constraints are applied in each space. The constraint in reciprocal space is still the Fourier modulus constraint, identical to Eq. 1.6. The real space constraint is the so called overlap constraint which enforces the overlapped sample area from multiple measurements to be identical. Here, we describe the extended ptychographic iterative engine (ePIE) algorithm [61] that will be extensively used throughout the rest of this thesis.

The inputs of the ePIE algorithm includes:

(1) The J measured diffraction intensities, $I_j(\vec{k})$, with $j = 1,2,\ldots J$;

(2) The coordinate of each scan position, $\vec{r}_j$, with $j = 1,2,\ldots,J$;

(3) The initial guesses for the probe and object functions, $p^{(0)}(\vec{r})$ and $o^{(0)}(\vec{r})$.

In the nth iteration, the ePIE algorithms run as follows, see Fig. 1.12(b):

[1] For the jth scan position, calculate the ESW:

$$\psi_j^{(n)}(\vec{r}) = p^{(n)}(\vec{r})\cdot o^{(n)}(\vec{r}-\vec{r}_j); \quad (1.17)$$

[2] Propagate the ESW to the detector plane:

$$\Psi_j^{(n)}(\vec{k}) = \mathcal{P}\{\psi_j^{(n)}(\vec{r})\}; \quad (1.18)$$

[3] Apply the Fourier modulus constraint by replacing the Fourier modulus with the measured amplitude while keeping the Fourier phase:

$$\Psi'^{(n)}_j(\vec{k}) = \sqrt{I} \cdot e^{i \cdot \angle \Psi^{(n)}_j(\vec{k})}; \quad (1.19)$$

[4] Propagate the updated function back to the object plane to form an updated ESW:

$$\psi'^{(n)}_j(\vec{r}) = \mathcal{P}^{-1}\{\Psi'^{(n)}_j(\vec{k})\}; \quad (1.20)$$

[5] Update the probe and object guesses using the updated ESW:

$$\begin{cases} p^{(n+1)}(\vec{r}) = p^{(n)}(\vec{r}) + \alpha \frac{o^{*(n)}(\vec{r}-\vec{r}_j)}{|o^{(n)}(\vec{r}-\vec{r}_j)|^2}[\psi'^{(n)}_j(\vec{r}) - \psi^{(n)}_j(\vec{r})] \\ o^{(n+1)}(\vec{r}) = o^{(n)}(\vec{r}) + \alpha \frac{p^{*(n)}(\vec{r}+\vec{r}_j)}{|p^{(n)}(\vec{r}+\vec{r}_j)|^2}[\psi'^{(n)}_j(\vec{r}) - \psi^{(n)}_j(\vec{r})] \end{cases}, \quad (1.21)$$

[6] Repeat steps (1-5) at all other scan positions to complete one full iteration to update the entire illuminated object area.

Further extensions of the ePIE algorithm include a recent edit for better convergence [67], a multimode implementation (which will be discussed and used in Chapter 2) [68], a super-resolution scheme relying on extrapolation [69], and upsampling undersampled data [68,70].

1.6 High Harmonic Generation

In this section, I will discuss tabletop coherent extreme ultraviolet (EUV) and soft x-ray (SXR) sources based on high harmonic generation (HHG) in gases, since they are the primary tool used in the experiments in this thesis. This is not meant to be a complete description of HHG but will hopefully introduce some of the basic concepts and principles of HHG. Some detailed reviews of HHG can be found in theses from previous graduate students in the Kapteyn-Murnane group [71,72], including the thesis of Tingting Fan for a complete discussion of circularly polarized HHG with collinear bichromatic drivers [73].

High harmonic generation is an extremely nonlinear process, in which intense, femtosecond pulses of light of some fundamental frequency, for example in the near infrared, is upconverted by some conversion medium to higher frequency harmonics in the EUV and/or SXR wavelength region, see Fig. 1.13 for a schematic illustration of the setup and some example HHG spectra using different drivers. At the core of the HHG process is the coherent nature of the driving laser and the atoms in the conversion medium, which work cooperatively to produce a bright and highly coherent beam of harmonics. The polarization, coherence and temporal properties of the driving laser is preserved during this process. It provides a compact and accessible way to generate coherent light beams in the EUV and SXR regimes when optimally phase matched [74-77], and is driving revoluntionary advances in quantum materials [78-82], nanoscale transport [83,84] and lensless imaging [18,20,22,85-87].

1.6.1 The microscopic picture: three-step model

The fundamental mechanism of HHG resides at the atomic scale. In HHG, charged particles, *i.e.*, the nuclei and electrons in the atoms, experience a force in the oscillating electric field of the incoming electromagnetic wave (intensive femtosecond laser fields) according to Coulomb's law. Electrons, being 1837 times less massive than protons, are accelerated more readily by the electric field. The subsequent motion of the electrons, as accelerating charged particles, results in re-radiation in the form of high energy photons. The coulomb potential from the ion causes the electrons to take on nonlinear motion – that is, the electrons do not simply undergo harmonic oscillations at the same frequency as the incident laser field. It is this anharmonic motion that results in emission of electromagnetic radiation at higher harmonics to the fundamental.

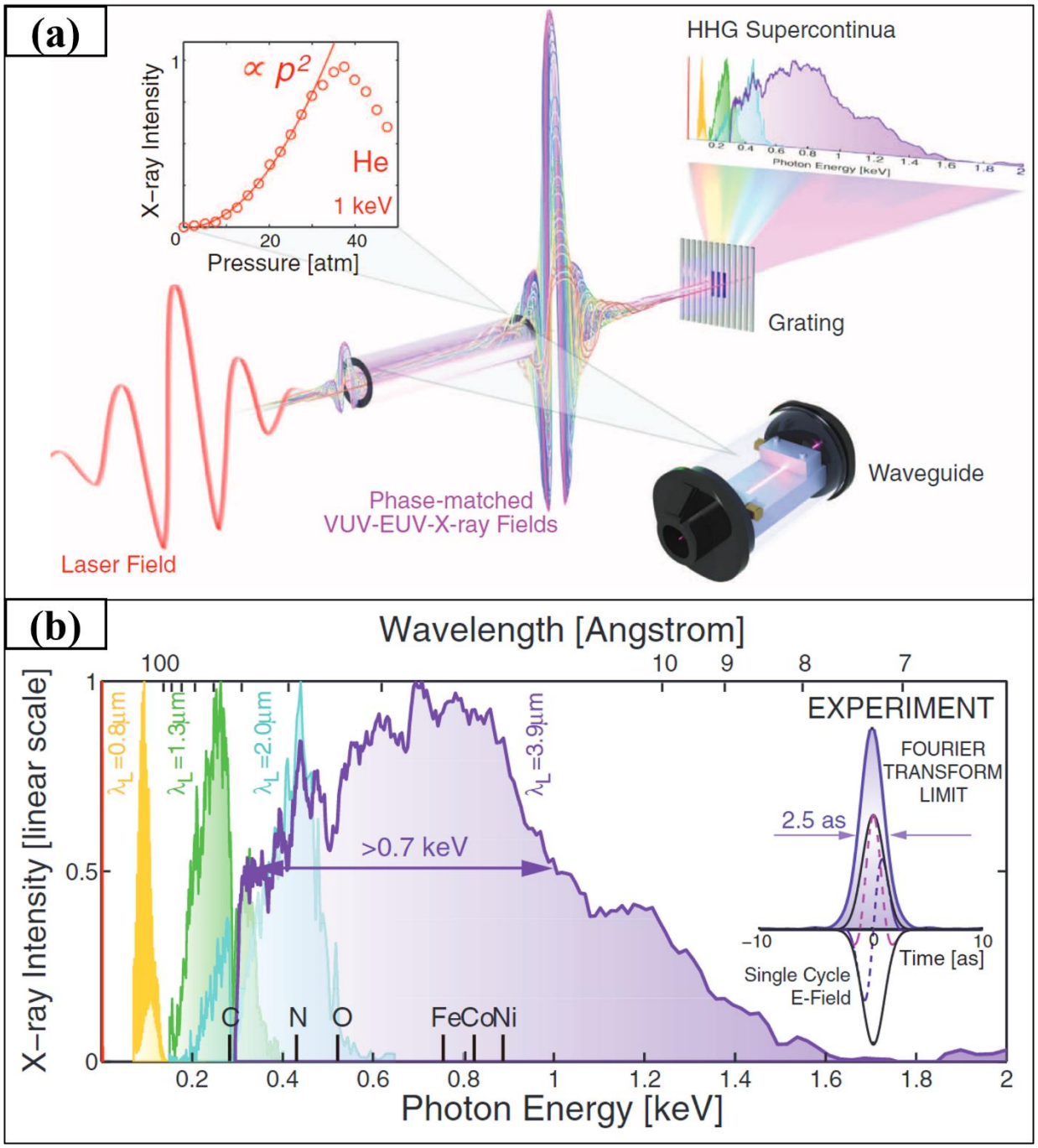

Figure 1.13: High harmonic generation. (a) Schematic illustration of high harmonic generation when a mid-IR driving laser pulse is focused into a high-pressure gas-filled waveguide. (b) Experimental HHG spectra emitted under full phase matching conditions as a function of driving laser wavelength (yellow, 0.8μm; green, 1.3μm; blue, 2μm; purple, 3.9μm). Figure is adapted from [77];

High harmonic generation was for the first time observed in the late 1980s [88,89]. Shortly thereafter, broad HHG spectra generated with infrared driving lasers with roughly similar harmonic intensities throughout the spectrum up to a cutoff energy were reported [90,91]. This indicates a non-perturbative regime of frequency conversion that had not been seen in lower intensity experiments, and a theoretical framework other than perturbation theory was needed to explain these findings.

In 1993, a semi-classical three-step model was proposed to better describe the HHG process [92,93]. This model is simplified, ignoring details of the fully quantum mechanical nature of the process [94], yet elegent, providing an intuitive picture of the HHG process and accurately predicting many important characteristics. It is formulated by considering the interaction of a single atom with an ultrafast laser pulse, and is depicted in Fig. 1.14.

The three-step model is detailed below:

Initial condition: The bound electrons in (typically) noble gas atoms stay in the ground state, feeling the Coulomb potential from the nuclei that prevents electrons from escaping.

Step 1 - Tunnel-ionization: A strong laser field tilts the Coulomb potential and decreases the potential barrier, allowing electrons to tunnel ionize out of the atoms with significant probability, called the ADK rate [96], which is named after the authors who derived it. The laser's electric field must to be of similar order of magnitude as the Coulomb potential ($5 \times 10^{11}\ V/m$ for hydrogen) to significantly tilt the Coulomb potential to allow tunnel ionization, but not so high as to make the electrons unbound. Ti:sapphire amplifier laser systems can provide $10^{14} - 10^{16}\ W/cm^2$ peak power density which is sufficient for driving HHG.

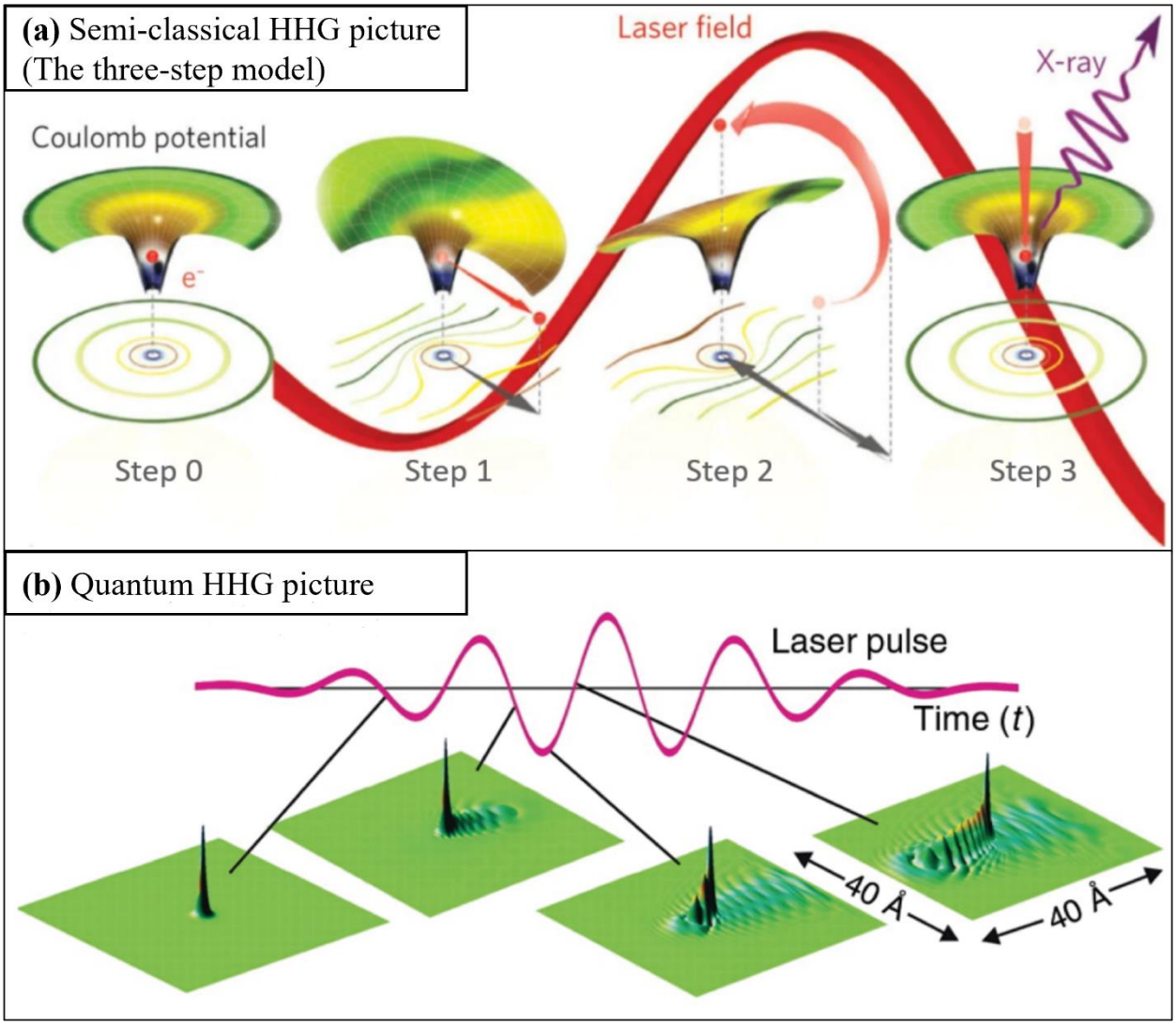

Figure 1.14: The three-step model – the microscopic picture of HHG. **(a)** The semi-classical picture of HHG, i.e., the three-step model. Electrons experience tunnel-ionization out of the Coulomb potential, acceleration in the laser field, recombination with their parent ions and simultaneous emission of high energy photons, adapted from [77]. **(b)** The quantum picture of HHG where the oscillating electron wave packets generate dipole radiation. Figure adapted from [95].

Step 2 - Acceleration: Once electrons are ionized and become free, they are accelerated away from the parent ions. As the laser field reverses direction, they are driven back toward the parent ions. During this acceleration process, electrons gain kinetic energy from the laser field, becoming highly energetic. Semi-classicly, this process can be modeled as a point charged particle moving in the laser's oscillating electric field. Quantum mechanically, the wave function of the ionized electrons must be calculated as a function of time. The longer the electrons are in the unbound state, the more spread out the wave function will be. Both approaches yield the same prediction for the electrons' kinetic energy when they come back to the parent ions, which depends on the phase of the laser's electric field when the electron tunnels out and becomes unbound. This maximum energy gain is:

$$\Delta E_{max} = 3.17\, U_p = 3.17 \frac{e^2 \mathcal{E}^2}{4\, m_e \omega^2} = \frac{e^2}{c\, \epsilon_0\, m_e} \frac{1}{(4\, \pi\, c)^2}\, I\lambda^2, \qquad (1.22)$$

Where U_p is called the ponderomotive energy (the energy that the electrons gain in the laser's electric field – sometimes called the cycle-averaged "quiver" energy), e is the electron charge, c is speed of light in vacuum, m_e is the electron mass, I is the driving laser peak intensity, and λ is the driving laser wavelength.

Step 3 – Recombination: The electrons arrive back at and recombine with the parent ions with a finite probability, and release the accumulated energy, up to ΔE_{max} in Eq. (1.22), in the form of high energy photons. The recombination probability can be found by calculating the expectation value of the dipole transition from the free electron state to the bound ground state. The cutoff energy of the higher-order harmonics is given by:

$$E_{cutoff} = I_p + 3.17\, U_p \propto I\lambda^2, \qquad (1.23)$$

Where I_p is the ionization potential of the atoms.

I would like to point out three interesting features of HHG:

(1) **Longer wavelength driving laser can produce higher energy photons** since $E_{cutoff} \propto \lambda^2$ in Eq. (1.23). This can be understood again by considering the kinematic motion of a free electron in an oscillating electric field. The longer the wavelength of the driving laser, the longer the electron stays in the electric field and is accelerated, the more energy the electron gains from the field. However, higher photon energy comes at the cost of HHG flux.

(2) **Only odd harmonics of the driving laser are radiated.** Harmonic emission occurs when the electron recombines with its parent ion. If the electron is ionized at a phase $\phi_0 \in [0, \pi/2)$, the recombination will happen at a later phase $\phi_f \in (\frac{\pi}{2}, \pi]$ within the same half laser cycle. This results in harmonic emission occurring every half-cycle of the driving laser field, as shown in Fig. 1.15. The averaged result would be a pulse train of harmonic emission with temporal spacing $\frac{\lambda}{2c}$, and each individual harmonic pulse would have a duration less than a half-cycle of the driving laser field ($\tau_{HHG} < \frac{\lambda}{2c}$). This $\frac{\lambda}{2c}$ periodicity of the harmonic pulses in the time domain generates interference in spectral domain, causing the spectral peaks to occur only at every odd harmonic of the fundamental driving frequency.

(3) EUV beams generated by HHG can be fully spatially coherent, as demonstrated by Zhang *et al.* [97] by diffraction through pinholes spaced by 150μm and 250μm apart that shows 100% fringe visibility. We will take heavy advantage of this high degree of spatial coherence in the coherent diffractive imaging experiments presented in Chapter 2-4.

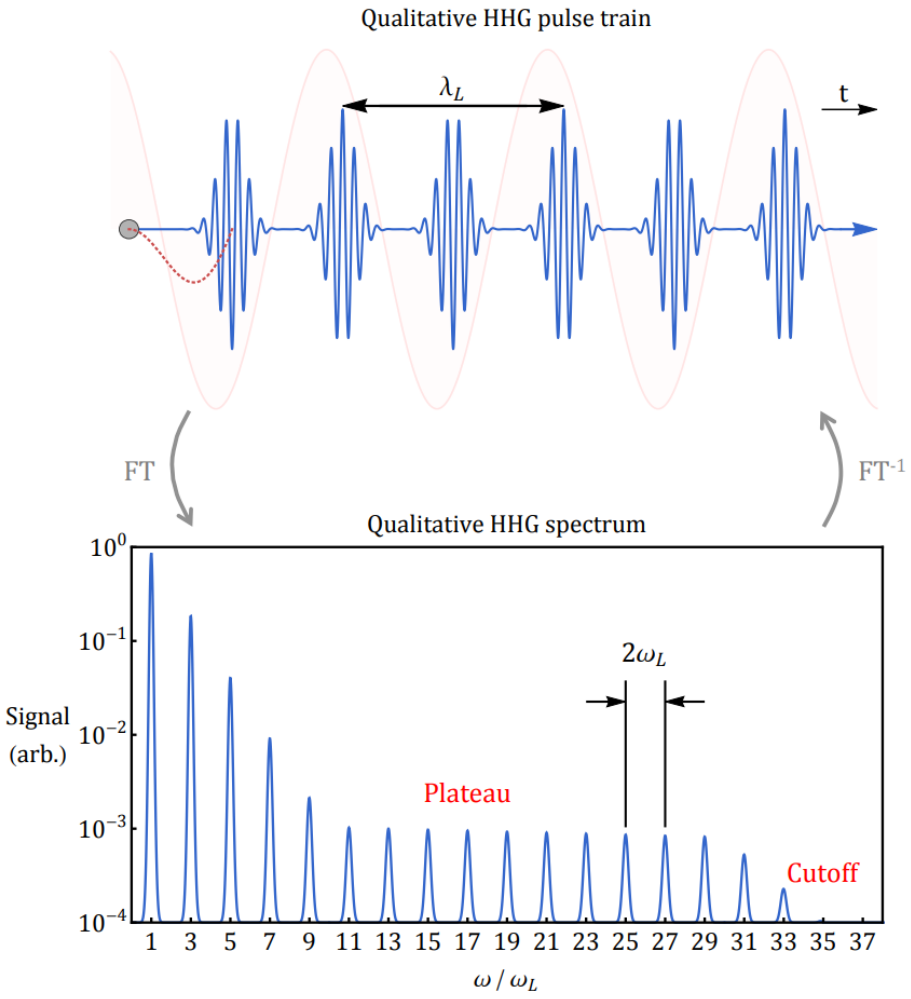

Figure 1.15: The temporal and spectral properties of HHG. Qualitative plots of HHG in time (top) and frequency (bottom) domains. Harmonic emission happens every half-cycle of the driving laser field, resulting in $\frac{\lambda}{2c}$ temporal spacing between HHG pulses. In frequency domain, this manifests as the characteristic $2\omega_L$ spacing of peaks in the spectrum, meaning only odd harmonics are generated. Figure is adapted from [72].

1.6.2 The macroscopic picture: phase matching

The three-step model gives us an fairly intuitive understanding of the HHG process at the single atom level. In order to have bright and coherent EUV beams of EUV/SXR light at the macroscopic level, a coherent summation of many single emitters is needed by matching the dispersion of the

HHG EUV light with the driving laser within the conversion medium, a process known as phase matching, as shown in Fig. 1.16. Phase matching is possible in various geometry and media, however, the discussion here is limited to phase matching in a capillary waveguide filled with noble gas [74, 98] because most of the experiments in this thesis use this technique.

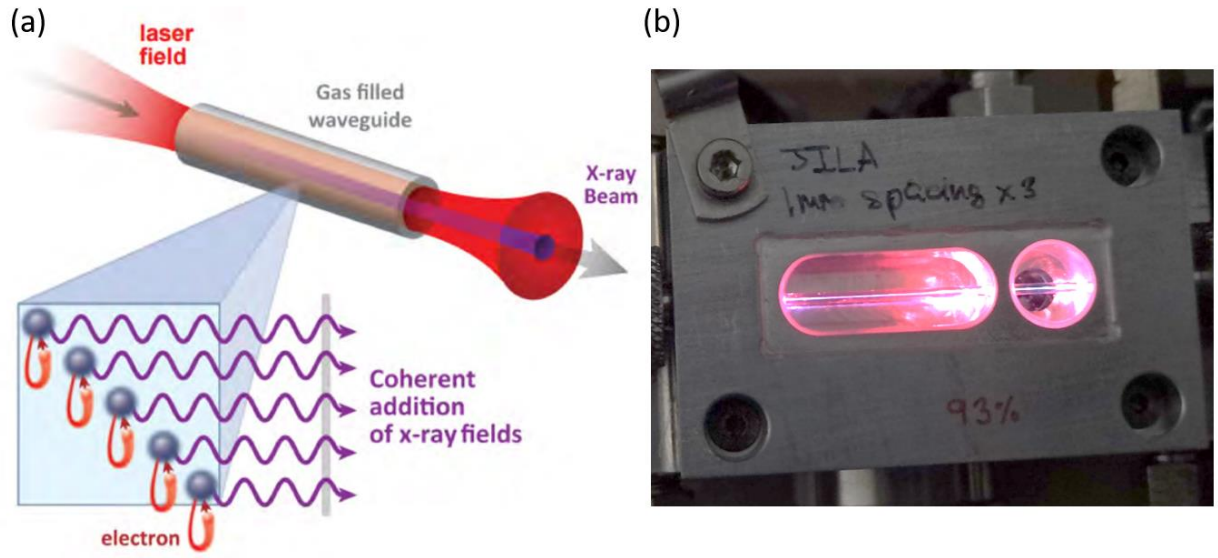

Figure 1.16: **Phase matching – the macroscopic picture of HHG. (a)** An intensive ultrafast laser is focused into a gas-filled waveguide, and the gas pressure is tuned to optimally achieve phase matching. This results in a coherent addition of the high harmonic radiation from each single emitters. **(b)** A picture showing the phase matching phenomenon in a waveguide filled with ~ 1 atmosphere of He gas.

Quantitatively, the phase matching requires the phase velocity of the driving laser, $v_0 = \frac{\omega_0}{k_0}$ is equal to that of the harmonic beams, $v_q = \frac{\omega_q}{k_q}$, where ω is the angular frequency and k is the magnitude of the wave vector in the propagation direction. Since $\omega_q = q\ \omega_0$, we must have:

$$\Delta v = v_q - v_0 = \frac{(q\ k_0 - k_q)\omega_0}{k_q k_0} = 0. \qquad (1.24)$$

Thus, the requirement for phase matching reduces to the following wavenumber matching:

$$\Delta k = q\, k_0 - k_q = 0. \qquad (1.25)$$

For ultrafast driving laser coupled into the EH_{11} fundamental mode of a capillary waveguide filled with noble gas, the wavenumber matching turns out to be [74, 99]:

$$\Delta k = \underbrace{\frac{q\mu_{11}^2\lambda_0}{4\pi a^2}}_{waveguide\ dispersion} - \underbrace{q\frac{2\pi P(1-\eta)}{\lambda_0}(\Delta\delta + n_2)}_{neutral\ atom\ dispersion} + \underbrace{qP\eta N_a r_e \lambda_0}_{plasma\ dispersion}. \qquad (1.26)$$

All terms include both the driving laser wavelength, λ_0, and the harmonic order, q. The waveguide dispersion term includes the mode factor, μ_{11}, describing waveguide coupling, and the waveguide inner radius, a. The neutral atom dispersion term includes the gas pressure, P, the ionization level, η, the difference in the indices of refraction of the gas for the driving wavelength and the HHG, $\Delta\delta$, and the second order nonlinear index of refraction of the gas for the driving laser, n_2. Last but not least, the plasma dispersion term includes the gas pressure, ionization level, the number density of atoms per atmosphere, N_a, and the classical electron radius, r_e. It is worth pointing out that:

(1) The waveguide and plasma terms provide positive dispersion, while the neutral atom term provide negative dispersion. This implies that phase matching is possible only if the ionization level stays below a critical value given by:

$$\eta_c = \frac{1}{1+\lambda_0^2\, r_e\, N_a/2\pi\Delta\delta}, \qquad (1.27)$$

Recalling Eq. (1.23), the cutoff energy of HHG cannot be increased by simply increasing the peak intensity of the driving laser, because phase matching is not possible at ionization level higher than η_c.

(2) both the neutral atom and plasma terms are dependent on the gas pressure and they provide dispersion with opposite signs. This indicates that the gas pressure is a convenient and effective experimental knob to achieve phase matching. From Eq. (1.26), the phase matching pressure in a waveguide geometry is found to be:

$$P_0 = \frac{\mu_{11}^2 \lambda_0^2}{4\pi a^2} \frac{1}{2\pi\,(1-\eta)(\Delta\delta+n_2)-\eta N_a r_e \lambda_0^2}. \quad (1.28)$$

In the experimental demonstrations in this thesis, we will use 400nm and 800nm femtosecond laser pulses to drive phase-matched HHG in gas-filled waveguides to produce bright and coherent EUV beams around 56nm and 13.5nm respectively.

It is worth mentioning that this pressure dependent phase matching condition is true only in the waveguide geometry. In a plane-wave free focus geometry, the phase matching condition occurs at the critical ionization regardless of pressure. The waveguide serves essentially to provide a new-plane-wave geometry and confine the beam over several Rayleigh lengths, improving the conversion efficiency in situations where the limited focal depth would otherwise limit conversion efficiency. Moreover, the initial experiments with HHG in the waveguide geometry were critical to understanding phase matching, providing a pressure dependence to the HHG process that makes it possible to clearly see phase matching effects.

Chapter 2: EUV Multibeam Ptychography

In this chapter, we demonstrate temporally multiplexed multibeam ptychography implemented for the first time in the EUV, by using a high−harmonic−based light source. This allows for simultaneous imaging of different sample areas, or of the same area at different time stamps or incidence angles. Furthermore, we show that this technique is compatible with wavelength multiplexing for multibeam spectroscopic imaging, taking full advantage of the temporal and spectral characteristics of high harmonic light sources. This technique enables increased data throughput using a simple experimental implementation and with high photon efficiency.

2.1 Introduction

Recent advances in nanofabrication require correspondingly powerful characterization techniques in order to capture both the structure and functional dynamics of nanosystems on their intrinsic length- and time-scales. Exciting new capabilities for probing the structural, mechanical, and transport (charge, heat, spin) properties of materials [12,18,20,46,100-106] down to angstrom and attosecond scales have been enabled by tabletop coherent short wavelength light sources based on high harmonic generation (HHG). In HHG, an intense femtosecond laser pulse is converted into coherent short-wavelength light, which can span from the vacuum and extreme ultraviolet (VUV and EUV) to the soft x-ray (SXR) spectral regions [74,75,88,89,107-109]. HHG light sources are characterized by their distinctive temporal and spectral structures — for example, when driven by many-cycle near-infrared laser pulses, HHG radiation emerges as a coherent series of attosecond bursts in the time domain, and as a comb of narrow ($\Delta\lambda/\lambda < 1\%$) harmonics in the spectral domain. Alternatively, when driven either by mid-infrared laser pulses or few-cycle near-infrared pulses,

HHG beams emerge as coherent supercontinua [77,110]. These unique properties make it possible to tailor the characteristics of HHG light sources for a wide range of applications in precisely probing the structure and dynamics of molecules, materials and nanosystems.

Coherent short wavelength light produced by HHG light sources has many unique advantages: it can (1) penetrate many visibly-opaque materials, including silicon and certain metallic or oxide layers, to probe and image buried structures; (2) image with nanoscale spatial resolution; (3) access intrinsic elemental, chemical and magnetic contrast, and (4) enable nondestructive dynamic imaging, without the need to coat, label or freeze the sample [18,20,22,101]. Lensless microscopy with HHG light sources can be implemented robustly through ptychographic coherent diffractive imaging (CDI) [61-64,85,111,112]. In ptychography, a coherent illuminating probe beam is scanned over an unknown object at a series of overlapping positions to produce a set of diffraction patterns, which are then used in a phase retrieval algorithm to extract a complex-valued image of the sample. Ptychography thus enables robust, diffraction-limited, phase-sensitive imaging of nanosystems. Powerful extensions to ptychography can enable multi-dimensional imaging of functional nanosystems — for example, incorporating a pump-probe scheme into ptychography for ultrafast stroboscopic imaging of nanoscale dynamics [86], scanning the incidence angle to obtain the depth-resolved composition of a specimen [20], or scanning polarization and incidence angle to measure three-dimensional magnetic structures [113,114]. However, the trade-off between the obtainable field of view and the dataset size and acquisition time inherent to the scanning ptychographic modality is further exacerbated by the introduction of these additional dimensions. Thus, it is extremely desirable to decrease the dataset size and acquisition time necessary for ptychography imaging and its extensions.

Several techniques have recently been developed to enhance the throughput of ptychography. Single-shot ptychography uses a pinhole array and lens to eliminate the scanning requirement [115-118]; however, there is an associated reduction in achievable resolution due to the reduced NA, and the reliance on refractive optics makes it difficult to implement in the EUV or X-ray. An appealing alternative is the use of two spatially separated beams for imaging, here referred to as multibeam imaging, based on ptychographic information multiplexing (PIM) [68]. By illuminating a sample with multiple mutually incoherent modes, multiple images can be simultaneously acquired and reconstructed with no tradeoff in resolution. Multibeam ptychography has been demonstrated to expand the field of view for ptychography microscopes based on visible light sources and synchrotron X-ray beams. With visible light, the requisite mutual incoherence is obtained by using dichroic or polarizing optics to obtain multiple beams differing in color or polarization, respectively [119]. However, such optics are not straightforward to fabricate for EUV wavelengths. PIM with mutually coherent light sources has been demonstrated by using autocorrelation filtering to digitally remove the interference artifacts, however this can only be done in special cases [120]. At synchrotron light sources, multibeam ptychography has been carried out by isolating two areas of a large beam separated by a distance greater than the transverse coherence length [121-123]. However, in addition to being photon-inefficient, this is not a straightforward solution for the fully coherent beams produced by tabletop HHG systems [75]. As such, multibeam ptychography has yet to be implemented for HHG light sources. In this work, we demonstrate that multibeam ptychography is naturally enabled by the pulsed nature of HHG light sources, which support mutual incoherence of illuminating modes through temporal separation. We demonstrate two-beam ptychographic EUV imaging with increased field of view, and resolution equal to single-mode ptychography with no additional cost in terms of

dataset size and collection time. Furthermore, by using a dichroic HHG source and simultaneously acquiring and reconstructing four modes (two wavelength channels in each beam), we show that temporal and spectral multiplexing are mutually compatible, enabling full use of the HHG comb for multi-wavelength imaging. Simultaneous spectral and temporal multiplexing make full use of the unique intrinsic properties of the HHG light source, enabling flux-efficient microscopy with a very simple experiment design. It enables simultaneous acquisition of data at different times, incidence angles, or locations on the sample, and thus can be applied to a wide range of ptychography-based techniques including dynamic imaging [86], ptychotomography [45], and wide-field-of-view imaging [119-123].

2.2 Experimental configuration

We demonstrate an EUV multibeam ptychography microscope illuminated by a high-harmonic generation (HHG) light source (Fig. 2.1). Part of the output of a Ti:sapphire amplifier (KMLabs Wyvern HE, λ = 790 nm, 45 fs pulse duration, 8 mJ pulse energy, 1 kHz repetition rate) is frequency doubled in a β-barium borate (BBO) crystal to generate light at 395 nm, yielding a 2ω pulse energy of 600 μJ when driven by 2 mJ of the fundamental laser. The 2ω beam is then coupled into a 5 cm length, 150 μm diameter hollow core waveguide filled with argon gas to generate harmonics. The driving laser is separated from the generated harmonics by using a 200 nm aluminum filter. This filter also blocks any harmonics with $\lambda > 77$ nm, while harmonics with $\lambda <$ 39 nm exceed the HHG cutoff energy, and so are not generated. Furthermore, due to the centrosymmetry of the medium, only odd-numbered harmonic orders are emitted. The remaining EUV light thus consists of narrow peaks at the 7th ($\lambda = 56$ nm) and 9th ($\lambda = 44$ nm) harmonics, the ratio of which can be varied by adjusting the argon pressure in the HHG waveguide. For temporal

multiplexing, we use an argon pressure of approximately 600 torr, to produce a quasi-monochromatic high-harmonic beam with λ = 56 nm. For wavelength and temporal multiplexing, we use a lower pressure of 150 torr, to produce a bichromatic light source with comparable intensity at λ = 56 nm and λ = 44 nm, as shown in the insert of Fig. 2.1. This beam is focused using a toroidal mirror (gold-coated, feff = 30 cm, 3x demagnification, 5° incidence angle from grazing), and divided between two paths by a glancing-incidence half-mirror (B4C coating, fused silica substrate, 3° incidence angle from grazing, nominal reflectivity 95%). The resulting two focusing beams are redirected towards the sample using a pair of glancing incidence recombining mirrors (B4C coating, fused silica substrate, 3° incidence angle from grazing, nominal reflectivity 95%). The sample is mounted on a precision translation stage ensemble (SmarAct) and translated in the plane perpendicular to the optical axis.

Approximately 1.5 mm in front of the sample, we place a laser-drilled pinhole to introduce a hard edge onto each beam for faster and higher-quality reconstructions. After transmitting through the pinholes, the beams impinge on different areas of the sample separated by about 4 mm, at an angle of ~3° from normal-incidence. This angle is small enough that there is minimal distortion in the diffraction patterns within our detector numerical aperture (NA = 0.27), and hence we do not need to correct for effects from conical diffraction (tilted plane correction) [124,125] during the reconstruction process. The total diffraction pattern is captured by an EUV-CCD detector (Andor iKon-L, 2048 × 2048, 13.5 μm pixels) positioned about 49 mm after the sample. Although the diffraction orders from the two illuminating beams overlap over the full area of the sensor, the DC peaks (1/e2 intensity width = 135 μm) are separated by about 1.59 mm, or 5.7% of the detector width. This slight separation is helpful in decoupling the contributions from the two beams during the reconstruction process (see Section 2.6).

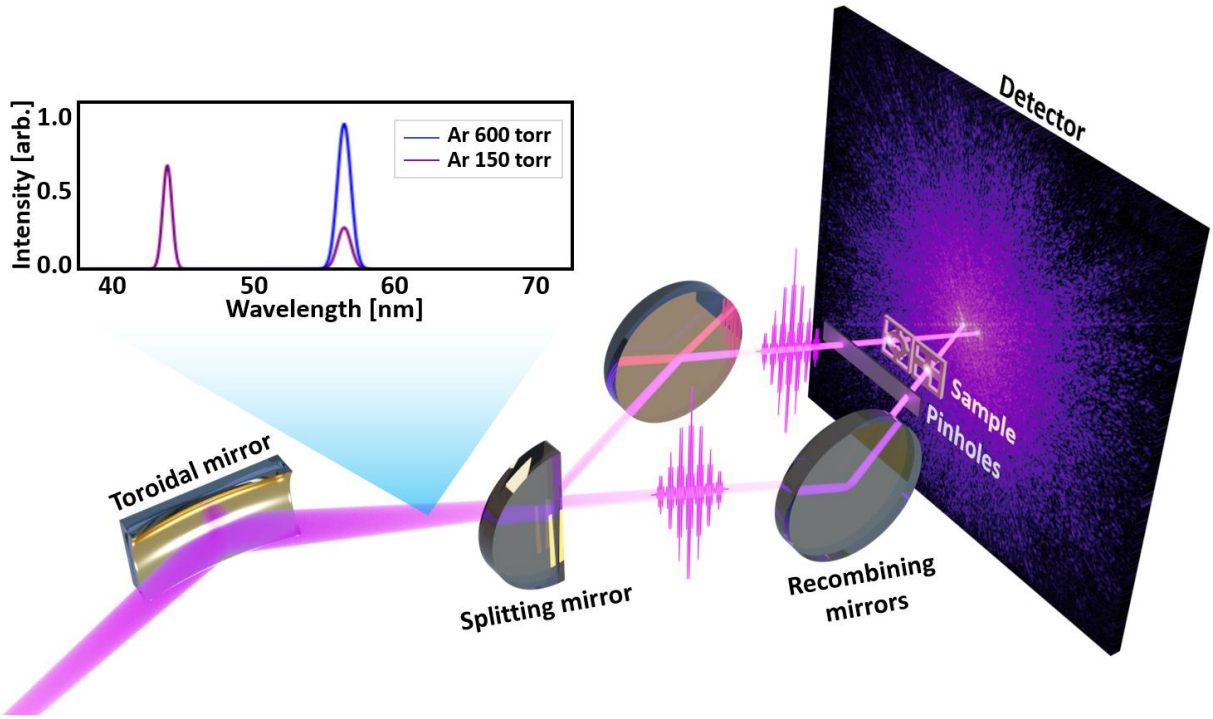

Figure 2.1: Schematic of the temporally multiplexed EUV microscope. The output of an HHG light source is divided into two separate paths and focused onto distinct areas of a sample, and the combined diffraction is recorded. Due to differences in the path lengths of the two beams relative to the extremely short duration of the HHG pulse train, the component diffraction patterns add incoherently, and the data can be directly used for multimode ptychography reconstructions. The insert shows the estimated spectra of the EUV light source. By adjusting the argon gas pressure in the waveguide, the generating conditions can be adjusted to select either a single harmonic peak at 56 nm, or two peaks at 44 nm and 56 nm. Figure adapted from [87].

2.3 Temporal multiplexing

In order to implement multiplexing in ptychography, we require that the beams are mutually incoherent, i.e., that they do not interfere. Despite the fact that the two beams in the experiment are derived from the same spatially coherent light source, and thus carry nearly identical spectral content and polarization, no interference is observed in the detector plane between the two component diffraction patterns. This is due to the short-pulse nature of HHG, combined with a

slight difference in path length traversed by the two beams. As a field-driven process, the HHG pulse train is emitted during the high-intensity portion of the driving laser pulse. For ~50 fs driving laser pulses, the HHG pulse train has a total envelope duration of ~10 fs, which gives a longitudinal coherence length of ~10 μm. Because the constituent beams travel optical paths which differ by greater than this very short coherence length, the pulse trains arrive at different times in the detector plane and not interfere. Mathematically, the total electric field of the two HHG beams $E(t)$ is composed of two electric field components $E_a(t)$ and $E_b(t)$. Because the camera exposure time is orders of magnitude longer than the oscillation period of the electric field components, the observed time-integrated diffraction pattern I is

$$I = \int_{-\infty}^{\infty} |E(t)|^2 dt = \int_{-\infty}^{\infty} |E_a(t) + E_b(t)|^2 dt$$
$$= \int_{-\infty}^{\infty} |E_a(t)|^2 dt + \int_{-\infty}^{\infty} |E_b(t)|^2 dt + \int_{-\infty}^{\infty} E_a^*(t) E_b(t) + \int_{-\infty}^{\infty} E_a(t) E_b^*(t) dt. \quad (2.1)$$

The final two cross terms represent the interference of the constituent fields, and manifest as modulation on top of the overlapped diffraction patterns, with a spatial frequency dependent on the probe wavelength and spacing in the sample plane. Even in the case that this frequency is below the pixel size of the detector (as is the case in our experiment), it is generally aliased to lower frequency modulation which prevents the application of multimode ptychography [120]. If, however, the fields are zero outside of some pulse duration τ, and separated in time by $\Delta t > \tau$ due to differences in optical path lengths, then the cross terms vanish:

$$I = \int_{0}^{\tau} |E_a(t)|^2 dt + \int_{\Delta t}^{\tau+\Delta t} |E_b(t)|^2 dt$$
$$= I_a + I_b \quad (2.2)$$

Therefore, the observed quantity is the incoherent sum of the individual diffraction components, and multimode ptychography can be directly used to analyze the data. A similar idea has been incorporated into single shot ptychography [126,127] for imaging of a dynamic sample. Here, we use this temporal multiplexing to achieve multibeam imaging with an HHG light source.

The sample consisted of a pair of 3 mm diameter transmission electron microscopy (TEM) grids mounted side by side. The first was a regular copper grid (62 μm period, 42 μm spacing, 20 μm bar) with a rectangular Quantifoil carbon mesh (part number Q410CS7, 9 μm period, 7 μm spacing, 2 μm bar); the second was a Ted Pella H7 Reference grid with Lacey Carbon support structure (part number 01897, 400 Mesh, 63 μm period, 51 μm spacing, 12 μm bar). On both grids, silver nanowires with a diameter of ~100 nm (Sigma-Aldrich Part #778095-25ML) were dropcast to provide deep sub-micron features. Unique and identifiable areas on both grids (the center of the regular TEM grid, and the letter "Q" on the reference grid) were chosen for illumination so that the ptychography results could be easily compared to optical microscope images.

For the data presented here, we collect diffraction patterns at 145 positions in the shape of a Fermat spiral, with an average nearest-neighbor spacing of 5 μm, or about 30% of the beam radius [128]. At each position, we acquire three diffraction pattern images with exposure times of 0.1, 1, and 10 seconds, and combine them to form a composite high dynamic range (HDR) image in order to increase the signal-to-noise ratio. The two fields of view are then reconstructed simultaneously using the PIM multimode ptychography phase retrieval algorithm [68]. In the reconstruction process, we include a supporting noise mode to improve reconstruction fidelity by accounting for systematic incoherence (see Section 2.6.1) [22,129], as well as a Fourier-space amplitude limit to help decouple the two physical modes (see Section 2.6.2).

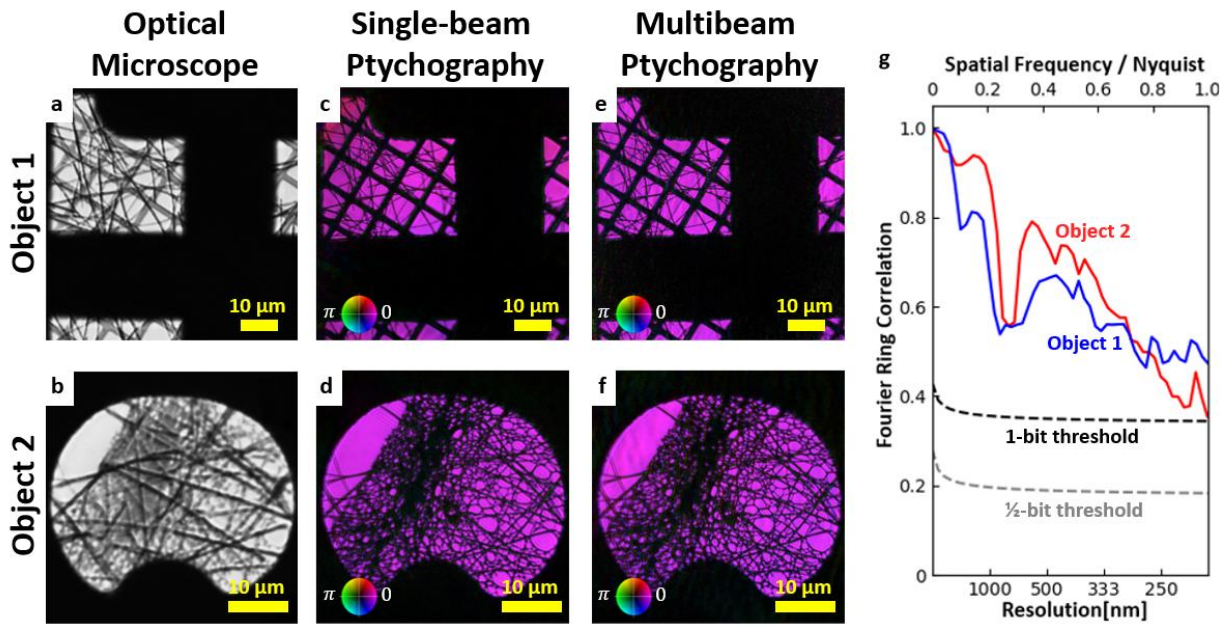

Figure 2.2: Single-wavelength, temporally multiplexed ptychography results. (a,b) Optical microscope images with white-light illumination transmitted through a short-pass filter (cutoff wavelength 400 nm) of (**a**, object 1) silver nanorods deposited onto a carbon mesh, and (**b**, object 2) silver nanorods deposited onto a lacey carbon support structure. **(c,d)** Separately acquired single-mode ptychography reconstructions of the same field of view using 56 nm illumination, and **(e,f)** simultaneously acquired, temporally multiplexed ptychography reconstructions using 56 nm illumination. **(g)** Fourier ring correlation measurement for the temporally multiplexed reconstructions, done by separating multibeam scans (**e**, **f**) into two independent data sets and reconstructing separately, demonstrating resolution out to the Nyquist frequency. Figure adapted from [87]

The multibeam ptychography results are shown in Figs. 2.2(e-f), and are compared to images obtained with an optical compound microscope (Olympus BH2-UMA, 50x, NA=0.70) using bright field, narrow-band illumination (white light transmitted through a short pass filter with cutoff wavelength 400 nm) shown in Figs. 2.2(a-b), as well as two separately acquired single-beam ptychography reconstructions shown in Figs. 2(c-d) (acquired by blocking one of the two HHG beams). The single-beam and multibeam ptychography scan parameters (step size = 5 µm, field of

view ≈ 5500 μm^2, exposure time = 0.1/1/10 s, etc.) are equal — thus the total dataset size and acquisition time to complete both single-beam scans were twice those required for the multibeam scan. In the ptychography images, the phase of the complex electric field is indicated by color (hue), while the amplitude is represented by the brightness (value). The coarse features are consistent between all three sets of images; however, fine features such as the nanowires and lacey carbon mesh are not well-resolved by the optical microscope due to the longer illuminating wavelength. In contrast, these features are much more clearly resolved in both the single-beam and multibeam EUV ptychography reconstructions.

The pixel size of the reconstructed images for our ptychography microscope is given by $\Delta r = \lambda z/Np$, where λ is the wavelength, z the sample-detector distance, N the number of pixels on the detector in the x or y direction, and p the detector pixel size in the x or y direction. For our experimental parameters, $\Delta r \approx 100$ nm. The best achievable resolution for both the single-beam and multibeam reconstructions is given by the Nyquist-Shannon sampling theorem as twice this pixel size, or 200 nm [130]. To quantitatively evaluate the resolution of our images, we split the acquired multibeam dataset into two independent subsets of diffraction patterns, independently reconstructed both subsets, and used Fourier ring correlation (FRC) to measure the repeatability of reconstructed features in diffraction space [131]. The results for both object 1 and 2 are plotted in Fig. 2.2(g), along with the ½-bit and 1-bit information threshold curves, which represent signal-to-noise ratio levels of 0.5 and 1, respectively, as a function of spatial frequency. The FRC curves for both objects stay above both threshold curves out to the Nyquist frequency corresponding to 200 nm spatial resolution, confirming that we have detectable spatial frequency content above the noise level out to the edge of the detector. This analysis therefore shows that our EUV microscope increases throughput without sacrificing spatial resolution.

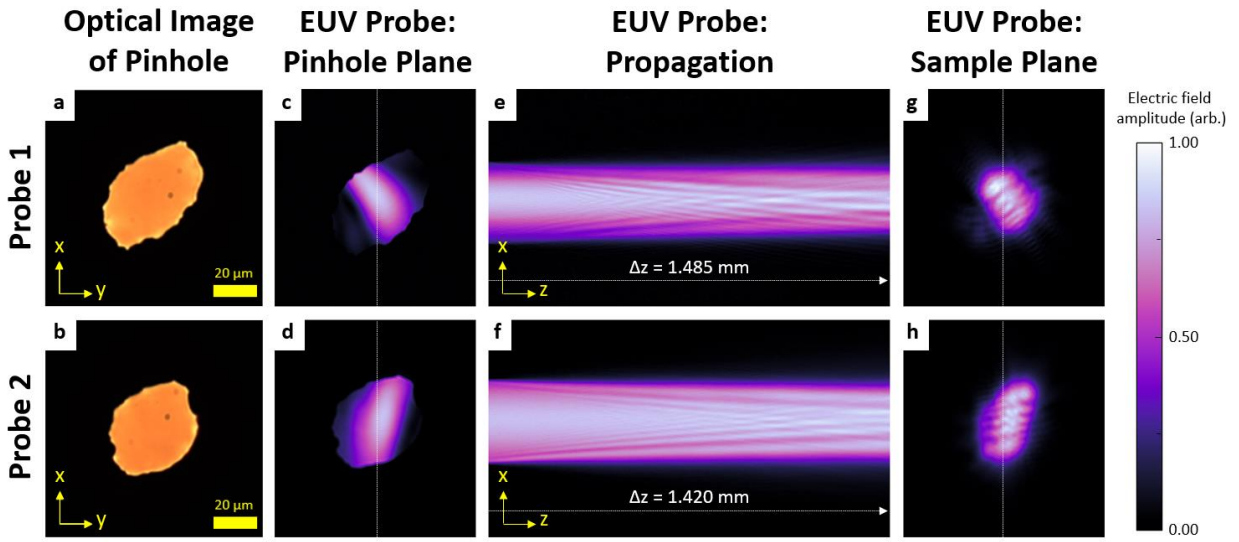

Figure 2.3: Characterization of reconstructed probes from multibeam ptychography scans. **(a,b)** Optical microscope images of the laser-drilled pinholes used to improve and constrain the two illuminating EUV modes for the ptychography microscope. **(c,d)** Reconstructed probes from the multibeam ptychography in the pinhole plane (**c**, probe 1; **d**, probe 2) **(e,f)** Evolution of the beams throughout propagation from the pinhole to the sample plane, shown as a slice at y = 0, i.e., the vertical dashed white lines in **c**, **d**, **g** and **h**. **(g,h)** Reconstructed probes in the sample plane. Figure adapted from [87].

The reconstructed probe profiles in the sample plane, Figs. 2.3(g-h), show near-field diffraction features from the hard edge introduced by the pinhole mask. To check the consistency of our results, we numerically backpropagate these probes, Figs. 2.3(e-f), from the sample plane back to the pinhole plane, in which the sharp edge of the aperture is clearly visible without any sort of masking, Figs. 2.3(c-d). This plane is found to be about 1.42 mm and 1.49 mm from the sample for the 1st and 2nd probes, respectively, where the difference in distances is due to a slight relative angle between the pinhole mask and the sample mount. The shapes of the pinholes are confirmed to be correct by comparison with optical microscope images, Figs. 2.3(a-b), giving a high degree of confidence in the accuracy of the retrieved probes and hence the reconstruction quality.

2.4 Simultaneous temporal and spectral multiplexing

Previous work involving multibeam ptychography employed only a single type of multiplexing; modes with orthogonal polarizations, distinct wavelengths, or different times as described in the previous section, were used to achieve the requisite incoherence. Here, we demonstrate that wavelength-multiplexed spectromicroscopy [132-136] is compatible with temporal multiplexing, and that the two types of multiplexing naturally fit with the characteristics of HHG light sources. We illuminate the same areas of the sample as in the previous section – but now with a bichromatic beam, and acquire a ptychography scan at 300 scan positions arranged in a 20 x 15 rectangular grid, with average nearest-neighbor spacing of 2 μm and random offset at each position of up to 0.4 μm to avoid gridding artifacts. As in the single-wavelength case, diffraction patterns are acquired at each position with exposure times of 0.1, 1, and 10 seconds, and combined to create HDR data.

To increase the speed of the reconstruction algorithm, we crop the acquired diffraction patterns to 1024 × 1024 pixels. We then apply the same multimode ptychography algorithm described above with four physical modes to include the two beams, each with two wavelengths, as well as two noise modes, one for each wavelength, for a total of six modes. This produces four images, Figs. 2.4(a–d), where each of the objects are reconstructed at the two harmonic wavelengths. Fine features such as edges, nanowires, or lacey carbon appear sharper in the 44 nm images than in their 56 nm counterparts due to the reduced pixel size in the reconstructions. Additionally, there is clear spectral contrast in the lacey carbon film, evident by comparing the same areas of the 56 nm reconstructions in Fig. 2.4(e), corresponding to the boxed area in Fig. 2.4(c), and the 44 nm reconstructions in Fig. 2.4(f), corresponding to the boxed area in Fig. 2.4(d). In Figs. 2.4(e–f), the brightness corresponds to the square root of the electric field amplitude to make the intensity and

phase contrast clearer. The field transmitted through the thin carbon film has a wavelength-dependent transmission, as well as a positive and wavelength-dependent relative phase shift, Figs. 2.4(e–f). By taking the average phase shift over small areas of the carbon film and the open area (orange and white circles, respectively), we find that the measured phase shift is consistent with the expected (anomalous) dispersion of an amorphous carbon film [137] of thickness 18–24 nm, Fig. 2.4(g), in agreement with thickness estimates from the manufacturer.

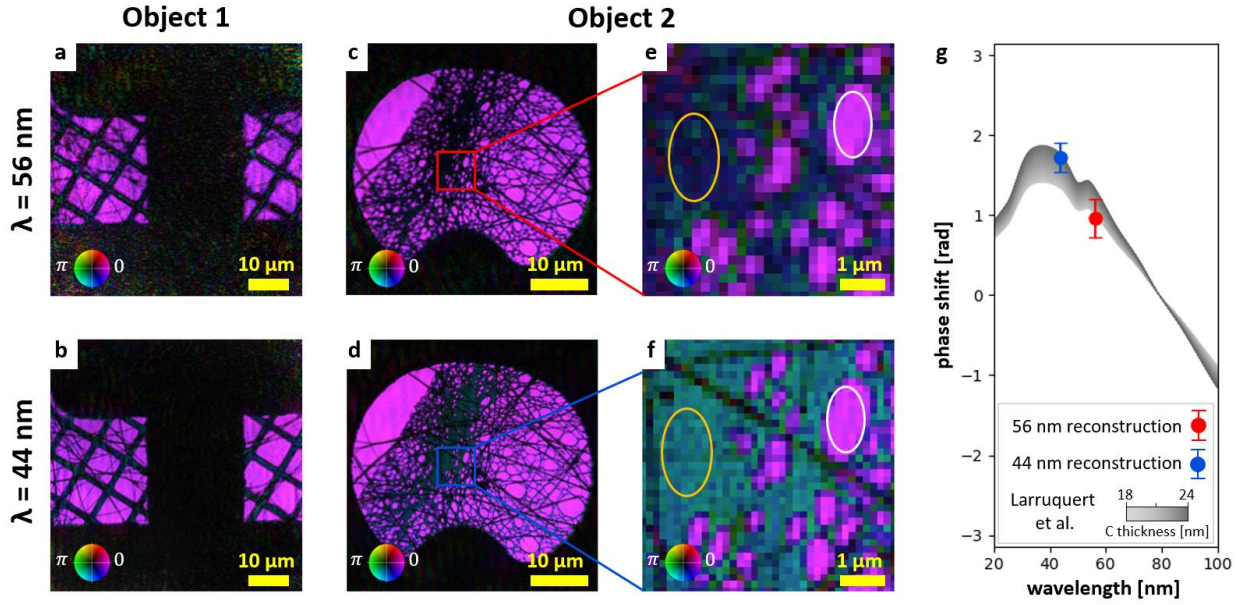

Figure 2.4: Temporally and spectrally multiplexed ptychography reconstructions. (a-d) Simultaneous reconstruction of object 1 (**a,** 56 nm; **b,** 44 nm) and object 2 (**c,** 56 nm; **d,** 44 nm). **(e-f)** Close-up of object 2 reconstructions, corresponding to the red and blue boxes in **(c-d)**. Here, the brightness corresponds to the square root of the complex field amplitude to highlight the phase and intensity contrast in the lacey carbon support mesh. White and orange ovals correspond to continuous areas of free space and lacey carbon, respectively. **(g)** Average phase shift measured for the lacey carbon at both harmonic wavelengths, compared to calculations for a range of thicknesses with literature values for the refractive index of amorphous carbon [137]. Figure adapted from [87].

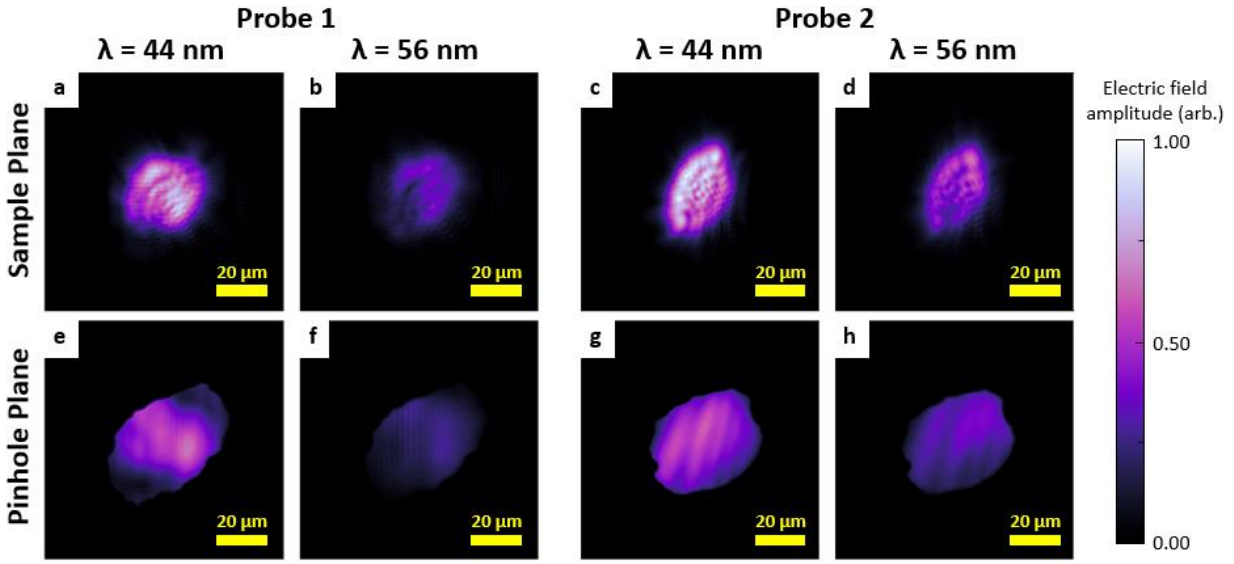

Figure 2.5: Reconstructed probes for temporally and spectrally multiplexed ptychography. **(a-d)** Probe amplitudes in the sample plane, retrieved as output from the ptychography algorithm. **(e-h)** Probe amplitudes in the pinhole plane, obtained by numerical back-propagation from the sample plane. Relative weights of the four probes are obtained by setting the transmission value of the free-space regions of the object reconstruction to unity, and scaling the probes appropriately. The 56 nm reconstructions (**b, d, f, h**) are interpolated onto the same pixel size as the 44 nm reconstructions (**a, c, e, g**). Figure adapted from [87].

The set of four reconstructed physical probes in the sample plane, Figs. 2.5(a-d), correspond to two beams, each containing two wavelengths. The approximate relative weights of the probes (from which the spectrum in Fig. 2.1 is estimated) are obtained by setting the free-space regions of the reconstructed objects to a transmission value of unity, and scaling the probe amplitudes appropriately to conserve power. For a given beam, the probe profiles for the 56 nm and 44 nm reconstructions are similar, but not identical. We repeat the procedure of backpropagating the probes to the pinhole plane, Figs. 2.5(e-h). As before, we find a well-defined sharp edge for each of the probes which is consistent with the expected pinhole size and shape, thus giving us high confidence in the accuracy of our reconstructed images. By comparing the two harmonic

wavelength reconstructions for a given beam in this plane, we observe that the illumination profile on the pinhole is slightly different for the two wavelengths.

2.5 Discussion

We have demonstrated a new type of multiplexed ptychography based on the temporal separation of otherwise similar HHG pulse trains. Mutual incoherence between the illuminating modes, which is necessary for the application of the PIM multimode ptychography algorithm, is acquired effectively automatically due to the very short duration of the HHG pulse train. This technique thus enables multiple diffraction-limited images to be acquired in parallel with an HHG-based microscope without the need for wavelength- or polarization-selective optics, which in the EUV and X-rays are not as readily available as in the visible. We show that this technique can be implemented with a simple, flexible, and photon-efficient experimental design, requiring only a few glancing-incidence optics for division and redirection.

As both illuminating modes have the same polarization and spectral qualities, they can be used to probe the consistent response of a static sample at different spatial positions for large field of view, or at different incidence angles for ptychotomography. Alternatively, a unique capability of the temporal multiplexing would be to acquire simultaneously multiple snapshots of the evolution of a dynamic sample. Thus, we expect that temporally multiplexed ptychography can be used to improve the throughput of a wide range of data-intensive EUV imaging experiments.

Additionally, given the distinctive spectral character of HHG light sources, we show a logical extension by simultaneously incorporating wavelength multiplexing of multiple harmonic teeth for multispectral imaging. This simultaneous implementation of temporal and spectral multiplexing in ptychography is a natural way to utilize the unique properties of HHG light

sources. We expect that this technique will continue to work as the number of temporally offset beams is increased through further division and recombination, and as the HHG comb is extended into the soft x-ray region by using ultraviolet driving lasers in multiply-ionized plasmas [138] or mid-infrared necklace beam drivers in helium [139].

2.6 Supplementary materials

2.6.1 Multimode ptychography algorithm overview

Ptychographic information multiplexing (PIM) [68] is used in this experiment to simultaneously reconstruct multiple spectral and/or temporal probe and object modes, which are mutually incoherent, from a single ptychographic data set. We use $P_{j,k}(\vec{r})$ and $O_{j,k}(\vec{r})$ to represent these mutually incoherent modes, where j denotes the j^{th} temporally isolated pulsed mode and k the k^{th} spectral mode. Under the projection approximation, the exit surface wave (ESW) in the sample backplane of the j^{th} temporal mode and k^{th} spectral mode at the l^{th} scan position can be modeled as $\psi_{j,k,l}(\vec{r}) = P_{j,k}(\vec{r}) \cdot O_{j,k}(\vec{r} - \vec{r}_l)$, where $\vec{r}$ is the coordinate in object plane and $\vec{r_l}$ is the position of the l^{th} scan position. The propagation of ESWs from the sample to the detector plane is modeled using the Fresnel diffraction equation, and the expected diffraction intensity pattern recorded by the detector at the l^{th} scan position, $I_l(\vec{q})$, is the incoherent superposition of the individual diffraction patterns from all modes,

$$I_l(\vec{q}) = \sum_{j,k} |\mathcal{P}_k\{\psi_{j,k,l}(\vec{r})\}|^2 = \sum_{j,k} |\mathcal{F}\{\psi_{j,k,l}(\vec{r}) \cdot FresnelPhase_k\}|^2 \quad (2.3)$$

where $\vec{q}$ is the reciprocal space coordinate with respect to the object space coordinate $\vec{r}$. $\mathcal{P}_k\{\psi\} = \mathcal{F}\{\psi \cdot FresnelPhase_k\}$ is the wavelength-dependent propagator for the k^{th} spectral mode from the sample to the detector planes, where $\mathcal{F}$ is the Fourier transform operation, and $FresnelPhase_k = e^{i\frac{\pi}{\lambda_k \cdot z} \cdot r^2}$ is the wavelength-dependent phase shift due to the curvature of the

wavefronts. In our multibeam ptychography setup, we centered the multiplexing diffraction patterns at the middle point of the centers of all diffraction components. The centers of each diffraction component are off centered in the detector plane, which can be attributed to a linear phase in real space, according to the Fourier shift theorem. One could let the PIM algorithm solve for it as part of the probe phase, but by using this prior knowledge of the imaging system and incorporating a known linear phase into the beam propagator, the PIM algorithm converges faster and achieves higher quality images of samples. We rewrite Eq. (3) below by including the linear phases for each mode in the beam propagator:

$$I_l(\vec{q}) = \sum_{j,k} |\mathcal{P}_k\{\psi_{j,k,l}(\vec{r}) \cdot e^{i\vec{r}\cdot\vec{q}_{j,k}}\}|^2 \qquad (2.4)$$

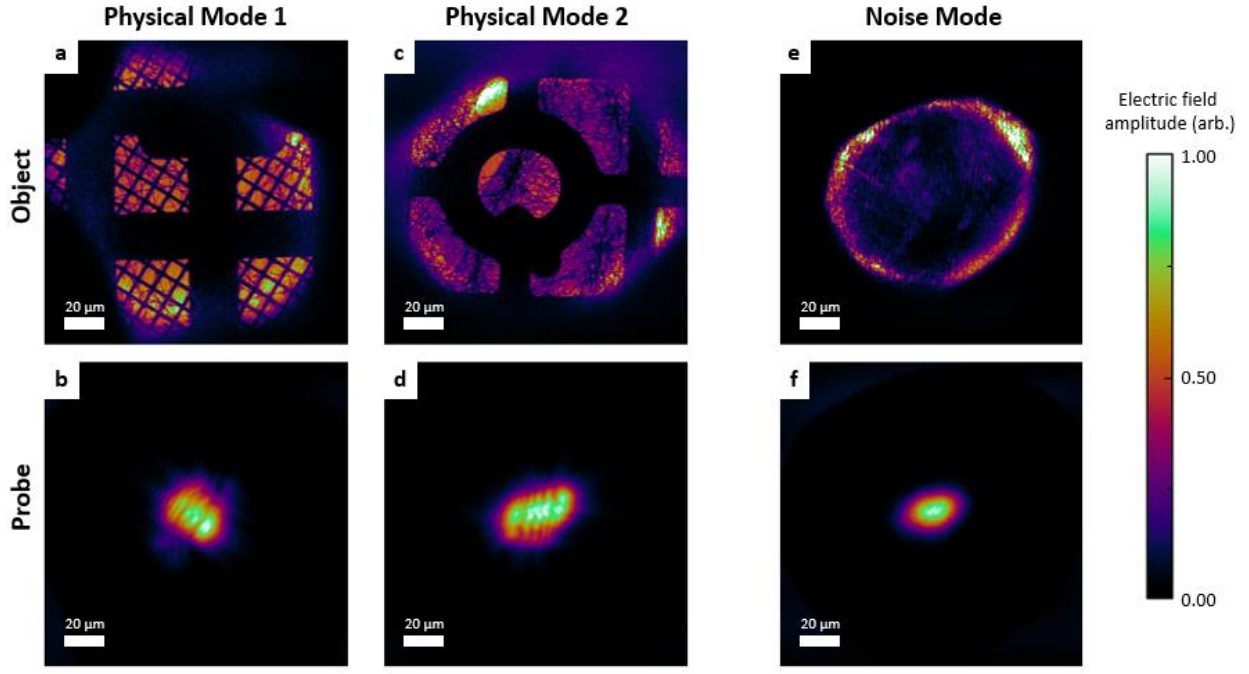

Figure 2.6: Physical and noise modes of the temporal multiplexing experiment. (a) Object 1 reconstruction at 56 nm, **(b)** Probe 1 reconstruction, **(c)** Object 2 reconstruction, **(d)** Probe 2 reconstruction, all shown in amplitude and corresponding to physical modes in the system. **(e)** Noise object 1 and **(f)** noise probe 1, accounting for decoherence effects in the system. Figure adapted from [87].

Furthermore, various experimental uncertainties need to be accounted for to reconstruct high fidelity images, such as illumination pointing and intensity fluctuations, sample vibration, detection noise, etc. They can be modeled as decoherence effects and can be compensated for by including noise modes in Figs. 2.6(e-f), which are mutually incoherent with respect to the physical modes in Figs. 2.6(a-d) [129]. Here, we included one noise mode, ${P^{noise}}_k(\vec{r})$ and ${O^{noise}}_k(\vec{r})$, for each wavelength in the illumination. The total diffraction intensity pattern at the lth scan position recorded by the detector, $I_l(\vec{q})$, can be expressed as

$$I_l(\vec{q}) = \sum_{j,k}|\mathcal{P}_k\{\psi_{j,k,l}(\vec{r}) \cdot e^{i\vec{r}\cdot\vec{q}_{j,k}}\}|^2 + \sum_k|\mathcal{P}_k\{{\psi^{noise}}_{k,l}(\vec{r})\}|^2 \quad (2.5)$$

where ${\psi^{noise}}_{k,l}(\vec{r}) = {P^{noise}}_k(\vec{r}) \cdot {O^{noise}}_k(\vec{r} - \vec{r_l})$ is the ESW of the noise modes. Notice that there is no linear phase in the propagation of noise modes, because these modes only account for systematic noise.

The PIM algorithm simultaneously reconstructs the complex-valued probe and object modes by iteratively transforming between real and reciprocal spaces and applying constraints in each space. In each iteration, PIM starts from guesses for the physical and noise probe and object modes, calculates the ESW of each mode, ${\psi}_{j,k,l}(\vec{r})$ and ${\psi^{noise}}_{k,l}(\vec{r})$, and numerically propagates them to the reciprocal space to obtain the diffracted waves, $\Psi_{j,k,l}(\vec{q}) = \mathcal{P}_k\{\psi_{j,k,l}(\vec{r}) \cdot e^{i\vec{r}\cdot\vec{q}_{j,k}}\}$ and ${\Psi^{noise}}_{k,l}(\vec{q}) = \mathcal{P}_k\{{\psi^{noise}}_{k,l}(\vec{r})\}$. The reciprocal space modulus constraint is applied on these diffracted waves as follows:

$$\Psi'(\vec{q}) = \frac{\sqrt{{I^m}_l(\vec{q})}}{\sqrt{I_l(\vec{q})}} \cdot \Psi(\vec{q}) = \frac{\sqrt{{I^m}_l(\vec{q})}}{\sqrt{\sum_{j,k}|\Psi_{j,k,l}(\vec{q})|^2 + \sum_k|{\Psi^{noise}}_{k,l}(\vec{q})|^2}} \cdot \Psi(\vec{q}) \quad (2.6)$$

where ${I^m}_l(\vec{q})$ is the measured diffraction pattern at the lth scan position on the detector plane. The updated diffracted waves are then back propagated to the real space to form the updated ESWs, ${\psi'}_{i,j,k}(\vec{r}) = {\mathcal{P}_k}^{-1}\{{\Psi'}_{i,j,k}(\vec{q})\} \cdot e^{-i\vec{r}\cdot\vec{q}_{j,k}}$ and ${\psi^{noise'}}_{j,k}(\vec{r}) = {\mathcal{P}_k}^{-1}\{{\Psi^{noise'}}_{j,k}(\vec{q})\}$, where

$\mathcal{P}_k{}^{-1}\{\Psi\} = \mathcal{F}^{-1}\{\Psi\} \cdot FresnelPhase_k^*$ is a backward propagation from the detector to the sample planes. The probe and object functions are updated as follows:

$$P'(\vec{r}) = P(\vec{r}) + \alpha \frac{O*(\vec{r})}{max(|O(\vec{r})|^2)} \cdot [\psi'(\vec{r}) - \psi(\vec{r})]$$

$$O'(\vec{r}) = O(\vec{r}) + \beta \frac{P*(\vec{r})}{max(|P(\vec{r})|^2)} \cdot [\psi'(\vec{r}) - \psi(\vec{r})] \quad (2.7)$$

where α and β are the feedback parameters. This process is performed for every scanning position and repeated until it reaches convergence. With a good probe initialization, we observe good convergence in <1000 iterations. The computer memory usage of the multimode reconstruction is greater in total than that of a single mode reconstruction, but less on a per mode basis as diffraction data, coordinates, etc. are shared between modes.

2.6.2 Fourier-space amplitude limit to help decouple incoherent modes

An example multibeam diffraction pattern from two mutually incoherent beams is shown in Fig. 2.7(a). It consists of two single-beam diffraction patterns centered at different positions on the detector plane. The PIM algorithm is used to decouple these two single-beam diffraction patterns and reconstruct the corresponding probe and object modes. However, this decoupling process turns out to be very difficult and slow, and can result in crosstalk artifacts appearing as haze or interference fringes in the reconstructed object images, as shown in Figs. 2.8(b) and 2.8(d). The origin of these artifacts can be understood by examining the Fourier transform of the PIM reconstructed object 1 and 2, shown in Figs. 2.8(c) and 2.8(e). If the two modes have been fully decoupled, the Fourier transform of each object should look similar to single-beam diffraction patterns, with a single bright DC peak in the center. However, the Fourier transforms of both

reconstructed objects show an additional residual peak at the position of the other beam, Figs. 2.8(b) and 2.8(d), indicating that there is significant crosstalk between the two modes. We confirm the link between the artifacts in real (object) and reciprocal (diffraction) space by measuring the period of the interference fringe artifacts in the object reconstructions to be 2.2 μm, corresponding exactly to the spacing of the two DC peaks in the diffraction plane, Figs. 2.8(a-e).

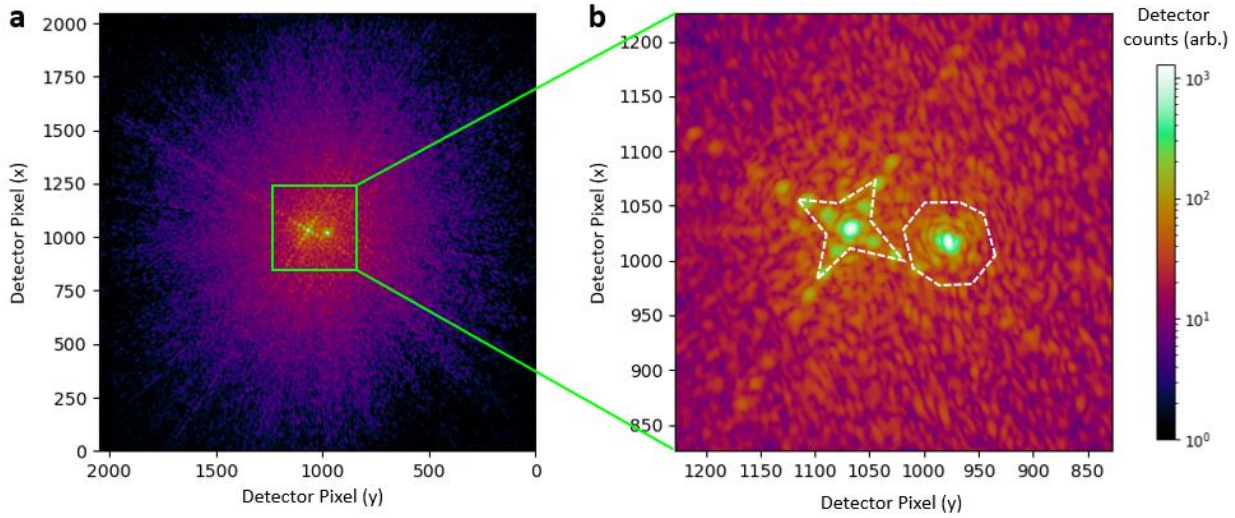

Figure 2.7: Diffraction pattern from two temporally incoherent illuminating modes. (a) Full detector area, showing two slightly separated DC peaks with overlapping diffraction orders out to the edges of the detector. **(b)** Close-up of the central part of the detector. The white dashed curves indicate the areas where the Fourier amplitude limit is applied to help decouple the two probe modes. Figure adapted from [87].

In order to help decouple these incoherent modes, an additional constraint is applied to the updated diffracted waves in the reciprocal (Fourier) space. During each iteration, at each scan position and for each physical object mode, take the Fourier transform of the updated object function, $|\mathcal{F}\{O'_{j,k}(\vec{r})\}|$, and enforce an amplitude limit of value ε to $\mathcal{F}\{O'_{j,k}(\vec{r})\}$ in a small area around the DC peak of other object functions (marked by white dashed curve in Fig. 2.7(b), and blue curves in Figs. 2.8(c, e, g, i), i.e. all pixels with value > ε in this small area are set to ε. The value of ε is initially set to be close to the values of the surrounding pixels in Fourier space, and fine-tuned to

improve the reconstruction. This operation is a powerful constraint which greatly helps decouple the two modes. The reconstructed object images with the Fourier-space amplitude limit included are shown in Figs. 2.8(f-h), showing higher quality and reduced interference artifacts. The Fourier transforms of the object images are shown in Figs. 2.8(g-i), and show almost no residual crossing diffraction components.

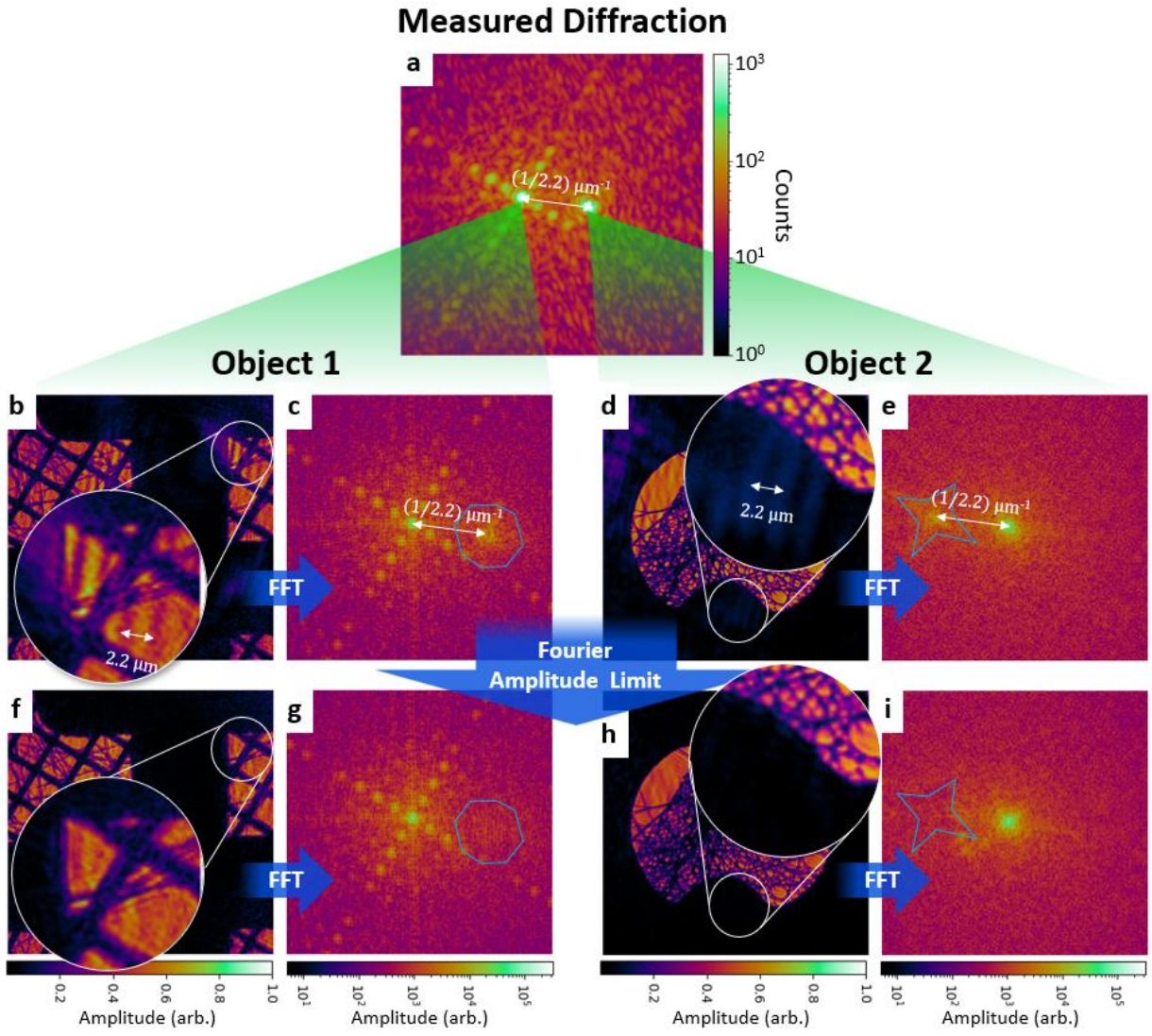

Figure 2.8: Application of Fourier amplitude limit operation. (a) Measured diffraction pattern at a single scan position, showing two DC peaks corresponding to two objects. **(b)** Object 1 reconstruction (without a Fourier amplitude limit operation), and **(c)** its Fourier transform. Haze and stripe artifacts in **(b)** object space result from incomplete decoupling of the two modes, visible

in **(c)** Fourier space as residual peaks (inside blue curves). Stripe artifacts in **(b)** have a period of 2.2 μm, corresponding to the separation distance between the true DC peak and the residual peak in **(c)** denoted by the white arrow. **(d, e)** similar for Object 2. **(f, g, h, i)** Reconstructions and Fourier transforms of both objects, this time with the Fourier amplitude limit step applied within the areas of Fourier space encircled by the blue curves. Figure adapted from [87].

Chapter 3: Tabletop EUV Actinic Microscope System

As EUV lithography transitions to high volume manufacturing, actinic inspection tools at 13.5 nm wavelength are attractive for understanding the printability of EUV mask defects, as well as for in-fab monitoring for possible defects emerging from extended use. Coherent diffractive imaging (CDI) is a lensless imaging technique that allows for phase-and-amplitude, aberration-free, high-resolution imaging in the EUV. Moreover, sources based on high harmonic generation (HHG) of ultrafast lasers are a proven viable coherent light source for CDI, with flux sufficient for rapid large-area inspection and small-area imaging. In this chapter, by combining CDI and HHG, we implemented actinic EUV photomask inspection on a low-cost tabletop-scale setup.

3.1 Introduction

Since the mid-1980s, EUV lithography has been under development, and it is currently integrated into the high volume manufacturing with 0.33 NA scanners at chip manufacturing facilities. As shown in Fig. 3.1, in an EUV lithography scanner, the 13.5 nm photons are generated by a laser-produced plasma (LPP) source. An optical device called a ‘collector‘ collects EUV light from the plasma source and focuses it to form an intermedium focus (IF). A collection of shaped optics, called an illuminator, then guide light from the IF to form a stable and uniform light field on an EUV photomask. Through an imaging system, called a projector, the pattern on the EUV photomask is transferred to wafers for nanopatterning.

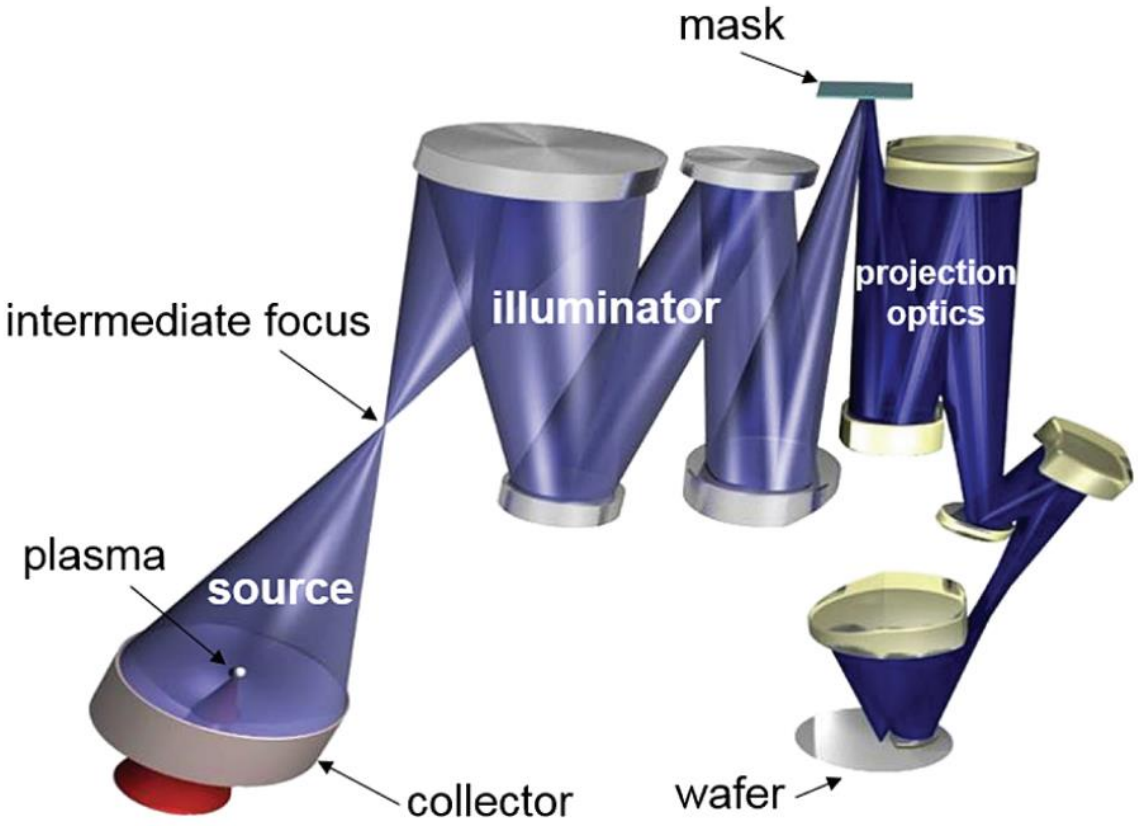

Figure 3.1: Schematic drawing of an optical system for an EUVL scanner. The EUV light generated by a plasma source is collected and focused by a collector onto the entrance of the illuminator, the so-called intermediate focus (IF). The illuminator then forms the light such that the mask is illuminated very homogeneously from well-defined beam directions. The mask is a critical optical element in itself, as it serves as a master template for lithographic printing. The structures on the mask generate a complex diffraction pattern containing the circuit information. The projection optics catches and combines this diffraction pattern, finally imaging the mask structure onto the wafer. Figure adapted from [140].

EUV Photomasks is a critical component because it serves as a master template for lithographic printing. Any defect/contamination must be ruled out before moving to and during extensive use in HVM. Conventional photomasks for deep ultraviolet (DUV) lithography at 193 nm wavelength are transmissive and work by blocking light using a single chromium layer on a quartz substrate.

However, because all materials heavily absorb EUV light, making reflective photomasks the only viable solution for EUV photomasks. An EUV photomask consists of a customized 6" by 6" square substrate made of low thermal expansion materials and 40 alternating silicon and molybdenum layers on top, which act to reflect EUV light around 13.5 nm through Bragg diffraction with a maximum efficienct of ~ 70%. A schematic view of the cross-ssection of an EUV photomask is shown in Fig. 3.2.

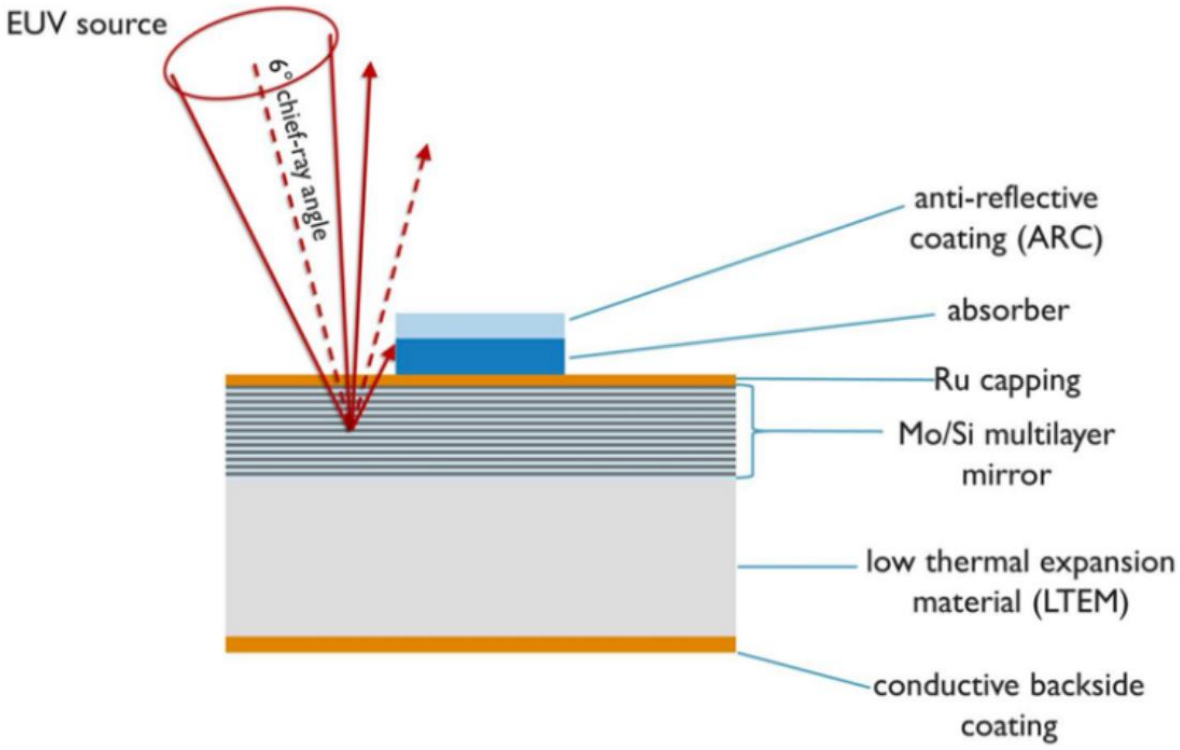

Figure 3.2: Cross-section of an EUV photomask. In EUV lithography, light incidents onto the mask at 6° of chief-ray angle, and is either reflected by the exposed multilayer mirror or absorbed by the absorber layer. Angles and thickness are not to scale. Figure adapted from [141].

As extreme ultraviolet (EUV) lithography is moving to high volume manufacturing, the fabrication and inspection of defect-free EUV photomasks remains one of the most critical and challenging issues in EUV metrology [17,142-146]. Although some inspection can be done using DUV or

electron beams, non-actinic inspection techniques struggle with low spatial resolution and/or exaggeration or distortion of the actual impact of photomask defects on patterned wafers. For example, it has been demonstrated that a photomask defect detected by electron beams can result in no impact on the patterned wafer [17], or vice versa. Consequently, an EUV actinic inspection tool is extremely attractive for inspection of the printability of EUV mask defects, as well as for in-fab monitoring for possible defects emerging from extended use.

However, current implementations of actinic review of masks using conventional reflective or zone-plate imaging are too expensive to be routinely employed. First, EUV microscopy using zone plate optics can inspect EUV masks with relatively high sensitivity and throughput [142]. But they can only provide amplitude images, i.e., no phase information, with resolution limited by the zone plate fidelity. Direct imaging with reflective optics is also possible, but with extreme demands on the optical figure and alignment [143]. In contrast, ptychography, as a particularly powerful approach to CDI, is a lensless imaging technique that allows phase-contrast, aberration-free and high-resolution imaging of semiconductor samples [18,20,61,64], including EUV photomasks. High-NA, diffraction-limited resolution can provide an unprecedented view of photomasks, making it possible to identify sub-threshold mask features that may evolve into printed defects. Furthermore, the phase information inherent in ptychographic images is very beneficial to numerical simulation tools for EUV technologies.

Ptychography has been used with synchrotron radiation to produce high quality images of EUV photomasks [144,146]—however, these sources have limited access. High harmonic generation [74,75] is a promising alternative to synchrotrons that can provide bright and coherent EUV light at 13.5nm. By combining HHG and ptychography, it is possible to implement actinic EUV mask inspection on a tabletop scale setup and at a reasonable cost. Although researchers have

demonstrated ptychographic reconstruction of micron- and submicron-scale features, the quality and reliability of these images still needs validation, and the challenge of ptychographic imaging of highly periodic structures, for example, 1D line-space and 2D contact array structures, remains to be definitively addressed. This challenge is due to the lack of diversity in the diffraction data [18,145,147] used in ptychographic reconstruction. Consequently, a versatile tabletop-scale tool for robust and reliable actinic EUV photomask microscopy has not previously been implemented.

3.2 System configuration

The TEAMS configuration is detailed in this section. It can be divided into the EUV source and beamline, and the ptychography microscope end-station, which consists both hardware and software development. Optically, the goal is to delivery as much EUV flux at 13.5 nm wavelength from the source to form a well-behaved illumination spot on the mask, called the probe. Mechanically, two sets of fine and coarse translational stages are used cooperatively to scan the EUV photomask in a wide range of 10*s* of cm while maintaining nm-scale precision. Complementary software for ptychographic data taking, processing and reconstruction is developed in a user-friendly manner.

3.2.1 The EUV light source

The TEAMS is powered by a bright and coherent tabletop HHG source at 13.5 nm wavelength driven by a Ti:sapphire laser. The Ti:sapphire amplifier (KMLabs RAEA^{TM}) is operating at λ ~ 790 nm central wavelength, 30 fs pulse duration, 3 mJ pulse energy, and 5 kHz repetition rate (total output power is 15 W). HHG up-conversion is accomplished in a KMLabs XUUS4 using a waveguide filled with ~ 1 atm helium gas. A beamline separates the EUV beam from the driving

laser, and a diagnostic beamline with a switchable mirror serves to optimize the spatial profile and flux of the EUV beam, as shown in Fig. 3.3(a). After the EUV beam is optimized, it is delivered to the lensless EUV microscope end-station, see Fig. 3.3(b).

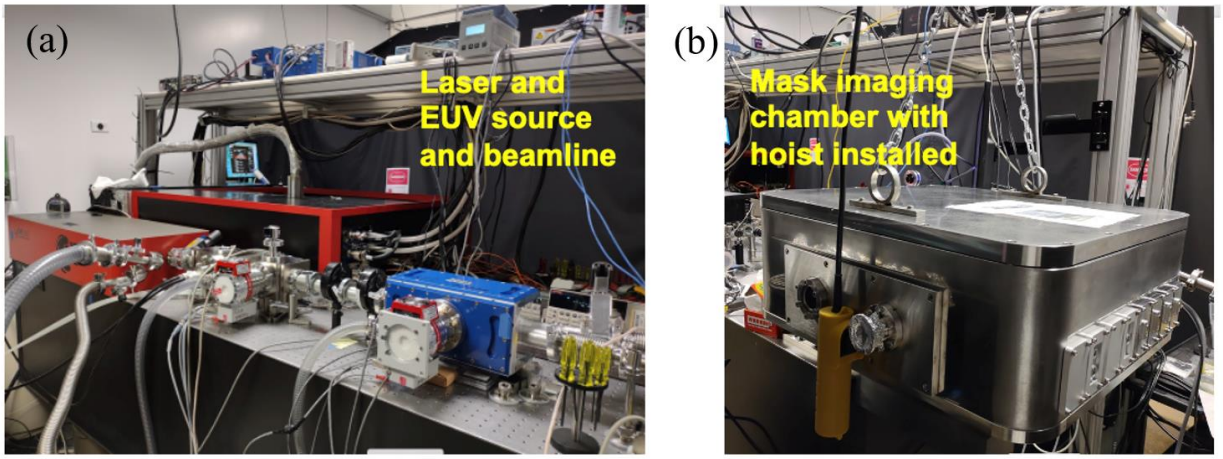

Figure 3.3: Photos show **(a)** the Ti:sapphire amplifier, XUUS for HHG, and diagnostic and beam delivery beamline, and **(b)** the actinic mask imaging end-station.

3.2.2 The lensless EUV microscope – Hardware development

The generated EUV HHG beam usually consists of a comb of narrowband peaks, which is not suitable for ptychography imaging. Therefore, two narrowband Si/Mo multilayer mirrors are used to select a single wavelength at ~ 13.5nm, with $\Delta\lambda/\lambda$ ~ 4%, for actinic ptychography imaging. More specifically, the first mirror is a spherical mirror, M_S, with 10cm radius of curvature and 0° nominal angle of incidence (AOI) from normal and the second mirror is a flat mirror, M_F, with 48° nominal AOI from normal. As shown in Fig. 3.4(a), the EUV illuminations incident from the left onto M_S at an angle of ~ 6° from normal, and is focused and folded into M_F. While the beam is focusing, the EUV beam is deflected by M_F upward onto the EUV photomask sample at an angle of incidence of ~ 6° from normal. Both mirrors are mounted on precision XYZ translation stage ensembles (SmarAct XYZ-SLC17:30) and can be precisely positioned in 3D space for alignment.

Furthermore, M_F has an extra degree of freedom for rotation (SRP20:13) to fine tune the angle of incidence onto M_F and the EUV photomask sample. The EUV photomask is mounted on a micro-scale precision XY translation stage ensemble (Griffin Motion XY stages) for coarse positioning over a large area (~100 x 100 mm^2). An EUV-CCD camera (Teledyne Princeton Instruments SOPHIA-XO 2048B-132, 2048 x 2048 imaging array, 13.5 x 13.5 um pixel size) is mounted below the sample, with the sensor facing up towards the sample and with a sample-to-sensor distance of ~ 40 mm, to capture the far-field diffraction patterns. A photo of the real apparatus can be found in Fig. 3.4(b). The reflectivity vs wavelength curves for each individual mirror and for the combination of both mirrors can be found in Fig. 3.4(c).

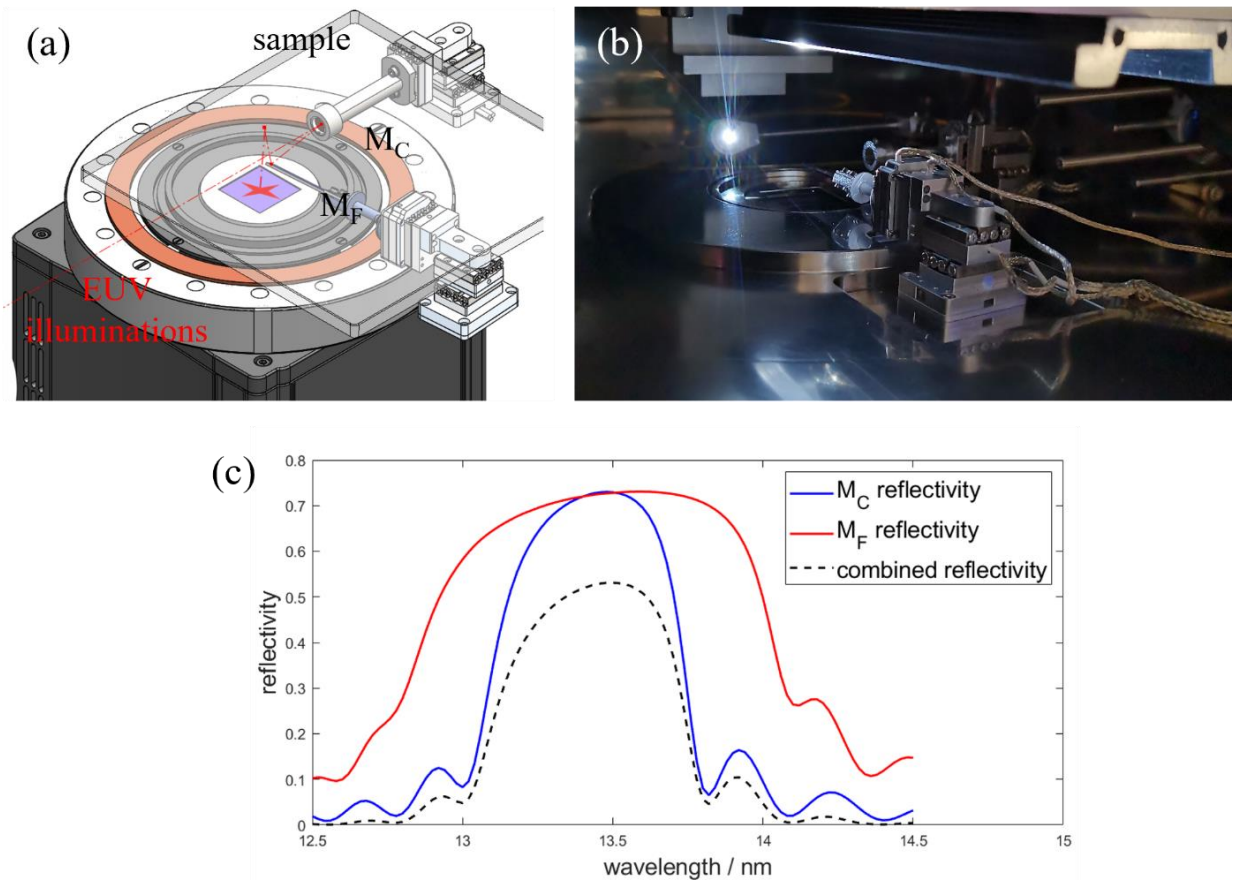

Figure 3.4: The lensless EUV microscope consists of two Si/Mo multilayer mirrors, M_C and M_F, to select out a single wavelength at 13.5 nm wavelength and focus it onto the EUV photomask sample at a 6° angle of incidence from normal. The EUV beam reflects and diffracts off the sample and is collected by an EUV-CCD camera. **(a)** A schematic diagram and **(b)** a photo of the lensless EUV microscope. **(c)** The reflectivity vs wavelength curves for M_C, in blue, M_F, in red, and both mirrors, in dashed black.

3.2.3 The lensless EUV microscope – Software development

We have developed a data acquisition software in LabView to perform ptychography scans on an EUV photomask and many other tasks. A screenshot of the main panel of the full program is shown in Fig. 3.5(a). This program is capable of saving sample positions and the corresponding far-field diffraction patterns, if desired, at regions of interest, automatically move the $\mathbf{M_S}$ and $\mathbf{M_F}$

translation and rotation stages to any saved coordinates, automatically performing ptychography scans at sample areas of interest, which is accessible through the “Ptychography” tab in the red dashed box in the cyan-highlighted area in the main panel, of which a close view is shown in Fig. 3.5(b).

We have also developed a data processing software package in MATLAB for reconstruction of ptychography datasets. Figure 3.6 shows a screenshot of the MATLAB script for data pre-processing in (a), including background noise removal, tilted plane correction [124, 125], binning, centering and cropping, and a screenshot of the running ptychography reconstruction interface in (b). The detail of this software package will be introduced in section 3.3.3.

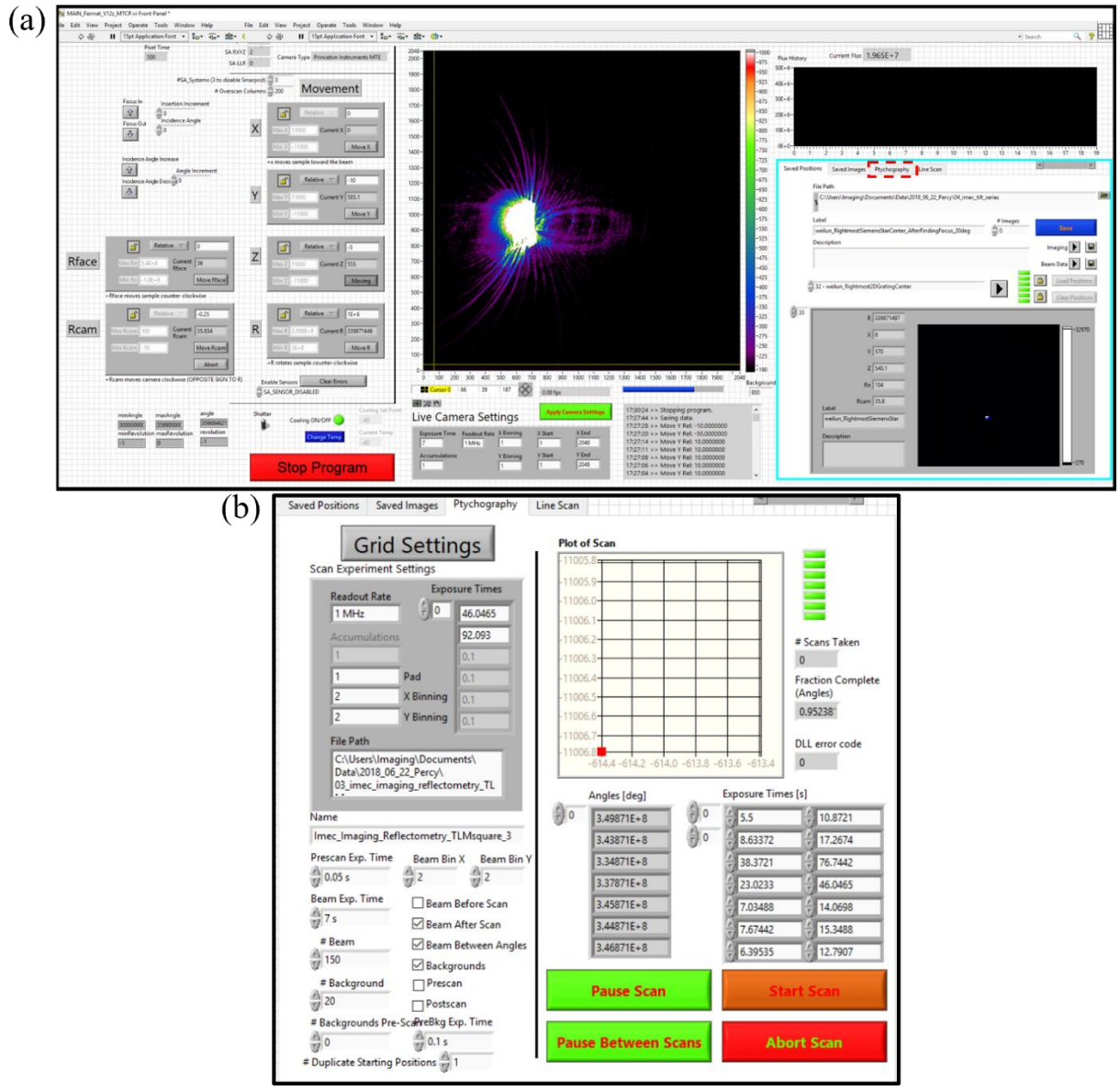

Figure 3.5: Screenshots showing the TEAMS data taking software user interface. (a) This screenshot shows the TEAMS data acquisition software full program. The functionality to setup and execute ptychography scans are under the "Ptychography" tab marked by the red dashed box within the cyan-highlighted area, of which a close view is shown in **(b)**.

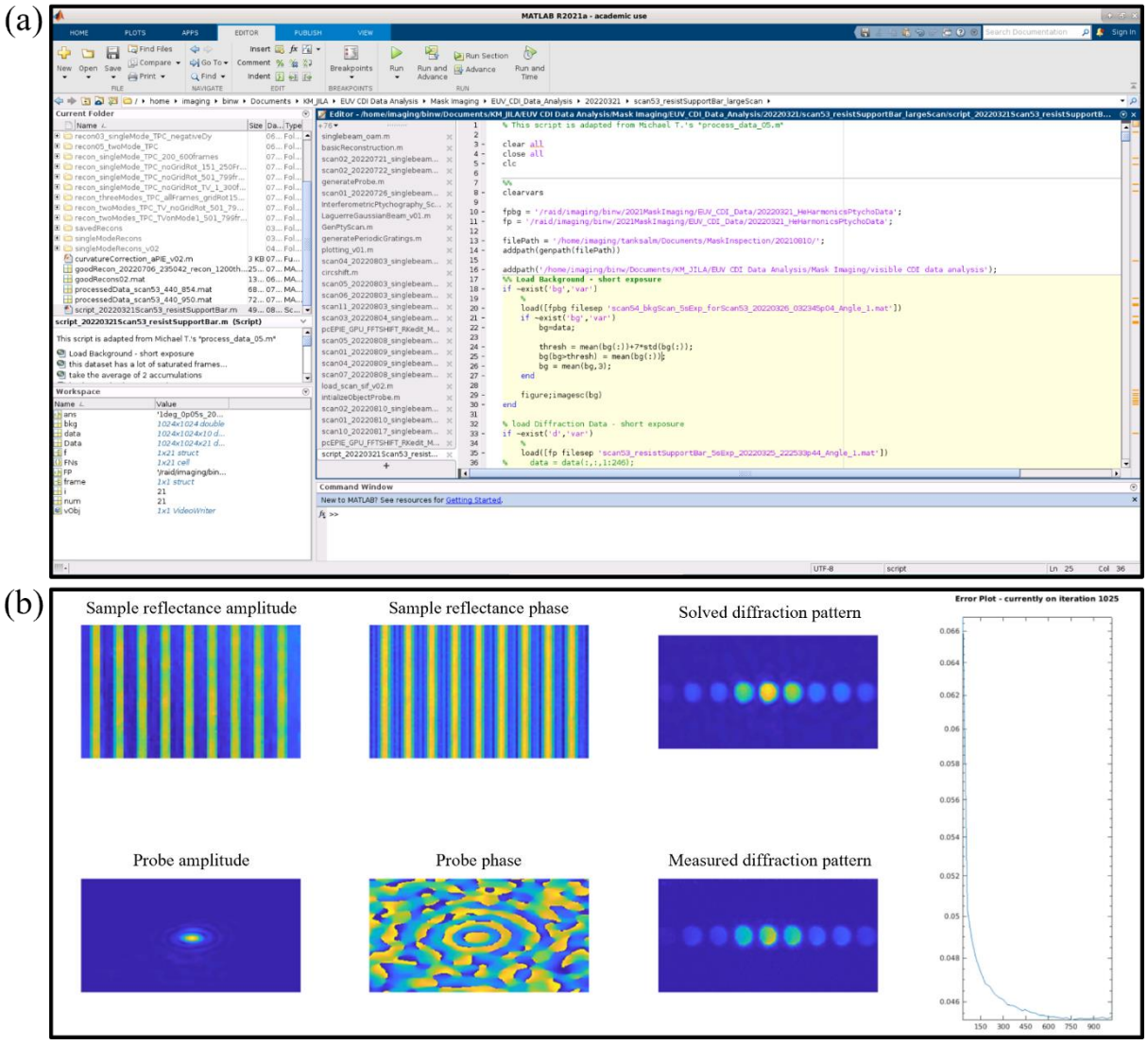

Figure 3.6: Screenshots of the TEAMS data processing software interface. (a) This screenshot shows the MATLAB script for data pre-processing necessary for running ptychography reconstructions. **(b)** This screenshot shows a running session of ptychography reconstruction.

3.2.4 Visible-light alignment microscope

Sample navigation is challenging for EUV imaging because the entire system needs to stay in ultra-high vacuum (UHV). We designed and installed an in-situ visible-light microscope with 10 um spatial resolution and a 2x2 mm^2 field of view to assist sample navigation under UHV. A

white-light LED is coupled into the EUV microscope vacuum chamber through a fiber feedthrough to illuminate the sample, see the bright light source in Fig. 3.4(b). Part of the reflected light from the sample surface is deflected by M_F into a single lens imaging system mounted on a cage system, and a CMOS camera is mounted on the outside-wall of the vacuum chamber to capture an image of the sample area. A reflective 1951 US Air Force test target, of which a photo is shown in Fig. 3.7(a), is used to align and test the alignment microscope. After it is aligned, a 2x2 mm^2 sample region in the red dashed box in Fig. 3.7(a) is imaged, resulting the image shown in Fig. 3.7(b).

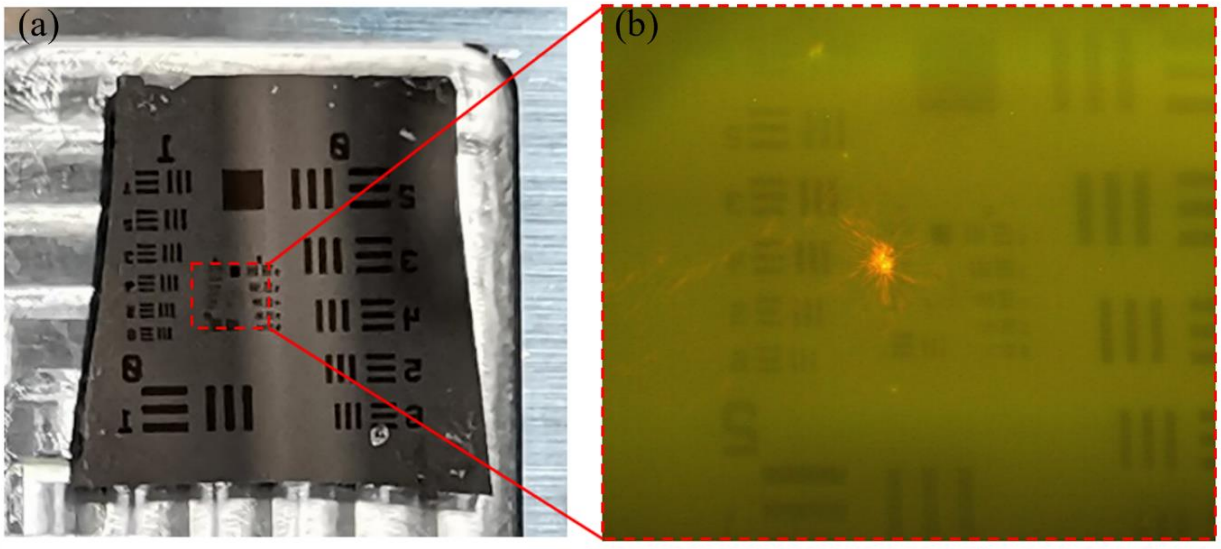

Figure 3.7: Optical alignment microscope for sample navigation. (a) This photo shows an USAF target for aligning the visible-light microscope. A 2x2 mm^2 region close to the center is imaged by the visible-light microscope, as shown in **(b)**.

3.3 Experimental results

3.3.1 Flux throughput estimation

The available photon flux at 13.5nm wavelength on the EUV photomask is estimated. Starting from the HHG source, there are two grazing incidence rejector mirrors to rejector most of the IR driving laser (sapphire substrates with 100nm Ru coating, 93.7% reflectivity at 13.5nm wavelength

each), Zr metal filters with a total thickness of 400nm to completely block the residual IR laser (24.7% transmission at 13.5nm wavelength), two Si/Mo multilayer mirror to select a single wavelength at ~13.5nm and deliver it onto the sample (~60% reflectivity each), which results in a total flux throughput at 13.5nm from source to sample of ~ 9.1%. Given a 10^{10} photons per second at the 13.5nm flux estimation at the source plane, we estimate the 13.5nm flux on the sample to be ~ 9.1×10^{8} photons per second.

The actual 13.5nm flux incident onto the sample can be measured by the built-in EUV-CCD camera of TEAMS. The monochromatic beam at 13.5nm wavelength goes through all optics described above and incidents onto a sample area with flat Si/Mo multilayer stack, and the specular reflection is recorded by the EUV-CCD camera. At 0.2 second exposure time, the EUV-CCD records a total amount of detector count of about 1.25×10^{8}. Given that the analog-to-digital converter setting is 5 electrons per detector count and the fact that each EUV photon at 13.5nm wavelength generates ~23 photoelectrons on average, the total number of EUV photon on the EUV-CCD per second is ~1.35×10^{8}. Furthermore, considering a reflectivity of ~60% for the Si/Mo multilayer stack on the sample, the number of photons per second on the sample is ~ 2.3×10^{8}, which is 4 times lower than the estimated flux on the sample. This discrepancy is likely due to non-optimal harmonic conversion efficiency, optics surface contamination/damaging, and Si/Mo multilayer oxidation (the EUV photomask from imec was fabricated in 2011).

3.3.2 Microscope geometry calibration

When installing the EUV microscope, there are two calibration steps that need to be done carefully.

First, the AOI on the EUV photomask and the distance between the photomask and the CCD sensor need to be measured very precisely, because the former one is necessary for correcting the curvature in diffraction patterns resulting from conical diffraction (see section 3.3 for more information), and the later one determines the scaling of the reconstructed sample images. However, it is almost impossible to measure them in traditional ways due to the limited space. We discovered an elegant, yet effective way for this task by utilizing the double reflection of the driving laser between the sample and the camera. This measurement is valid because the driving laser and the EUV beam is colinear. Fig. 3.8(a) shows a schematic side view of the EUV microscope. An attenuated driving laser beam passes through M_S and M_F, incident on the sample at an AOI of $\boldsymbol{\theta}$, and is reflected onto the camera. Since the sample and the camera surfaces are parallel to each other and are very reflective, the driving laser is reflected by the camera onto the sample, which is a distance of $\mathbf{z}$ away from the sample, and once again is reflected by the sample onto the camera. Consequently, what we record on the camera is two beams separated by a distance of $\mathbf{d}$, which is determined by the following linear equation:

$$\mathbf{d} = \mathbf{2} \cdot \mathbf{z} \cdot \boldsymbol{\theta} \qquad (3.1)$$

The flat mirror M_F is mounted on a rotational stage with an angular resolution of $25\boldsymbol{\mu}°$, which enables us to scan the AOI, $\boldsymbol{\theta}$, and measure the distance between the two beams on the camera. A linear fitting is then applied to the measured data points to extract the AOI and the distance, as shown in Fig. 3.8(b). In our setup, the AOI is set at 6° and the distance is measured to be 39.9mm.

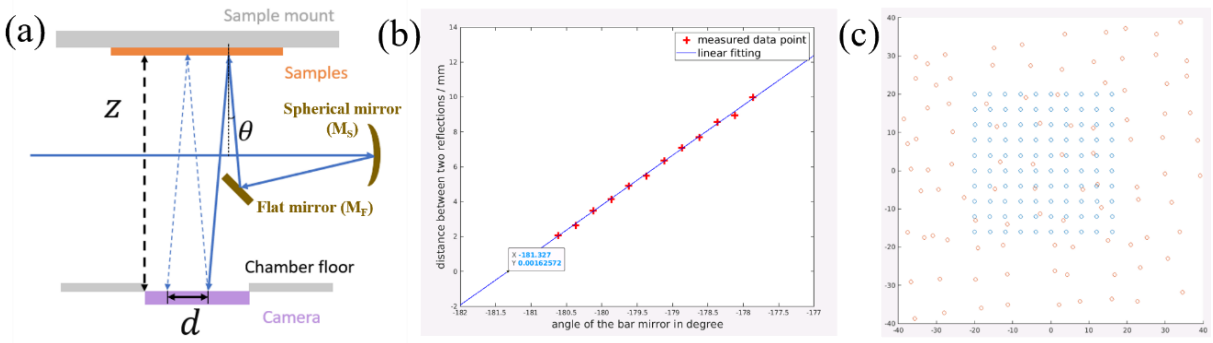

Figure 3.8: Microscope geometry calibration. (a) A schematic shows the double reflection feature between sample and camera that are used to measure the AOI on the sample and the distance between the sample and the camera. **(b)** Measured distance between the two beams on the camera as a function of the orientation of flat mirror is shown in red data points, and a linear fitting is performed to extract the AOI and the distance between sample and camera. **(c)** The spherical mirror is scanned along a 2D square grid, shown in blue circles, and the beam on the EUV-CCD moves in a corresponding grid, shown in red circles. The beam motion grid is rotated counter-clock-wise with respect to the mirror motion grid by ~2°, which indicates a minor misalignment of the orientation of the EUV-CCD by ~2°.

Second, the ptychographic scan is accomplished by scanning the spherical mirror, M_S, in a plane perpendicular to the beam direction. When one scans the spherical mirror horizontally or vertically, the beam on the EUV-CCD should also move left-and-right or up-and-down, as opposed to diagonally. However, the in-plane orientation of the EUV-CCD is extremely difficult to align perfectly, and the angular error needs to be calibrated and compensated carefully. This can be accomplished by scanning the spherical mirror in a square grid and monitoring the beam motion on the EUV-CCD. As shown in Fig. 3.8(c), the blue circles indicate the square scanning grid of the spherical mirror, and the red circles indicate the center of the beams on the EUV-CCD. Using a linear fitting, we obtained a 2 degrees angle offset between the ptychographic scanning coordinate and the EUV-CCD coordinate, which is later compensated during the data processing stage.

3.3.3 Data pre-processing procedure

Several significant pre-processing steps must be carried out between reading out images from a CCD and running ptychographic reconstructions. We have developed a MATLAB script capable of pre-processing ptychographic datasets once a small set of user inputs is established.

Step 1: Background subtraction, which is presented in Fig. 3.9(a-c). Before or after each ptychography scan, we block the EUV beam and take several background images with the same camera settings (for example, exposure time, temperature, readout rate, gain, etc.). One then subtracts the averaged background image (Fig. 3.9(b)) from each diffraction pattern in the ptychography dataset (Fig. 3.9(a)), resulting in much cleaner patterns (Fig. 3.9(c)).

Step 2: Thresholding to remove the detector readout noise, which has a Gaussian distribution with a mean close to zero and a standard deviation, from diffraction patterns. The threshold value is obtained by plotting a histogram of the diffraction patterns, determining the half-maximum of the peak around zero, i.e., the detector noise peak, and setting the larger one from the two corresponding pixel values as the threshold value.

Step 3: High dynamic range (HDR) image combination. HDR significantly increase the SNR in the ptychography datasets by taking multiple diffraction patterns with different exposure times at the same sample location and combining them into one via computer algorithms.

Step 4: Centering and cropping the diffraction patterns. The diffraction patterns are centered at the DC peak and cropped to an appropriate size.

Step 5: Tilted plane correction that corrects the curvature in diffraction patterns resulting from the 6° incidence angle from normal on the sample. Figure 3.9(d) shows an example diffraction pattern after the three steps above, and it is compressed vertically and stretched horizontally and is shown in Fig. 3.9(c) for better visualization of the curvature in it. We also added two parallel dashed red

line for reference. The incidence angle is determined by the method discussed in Section 3.2, and is used for tilted plane correct. An example corrected diffraction pattern is shown in Fig. 3.9(f-g).

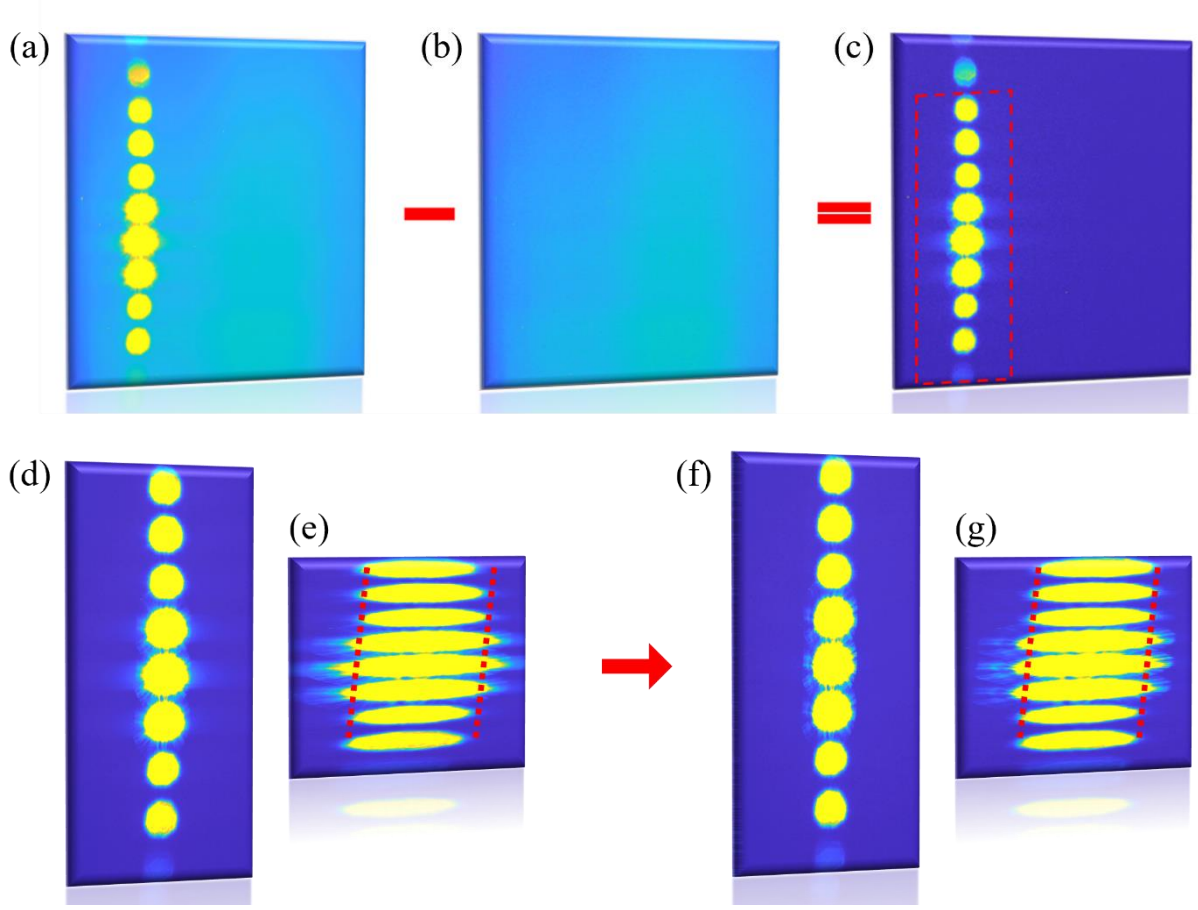

Figure 3.9: Data pre-processing procedures for TEAMS. (a) An example diffraction pattern offloaded from the EUV-CCD. **(b)** An example background image offloaded from the EUV-CCD with the same settings. **(c)** A background-subtracted diffraction pattern corresponding to **(a)**. The red dashed box indicates the cropping range. **(d-e)** A cropped diffraction pattern shown in different aspect ratio to better visualize the curvature. **(f-g)** A diffraction pattern after tilted plane correct shown in the same aspect ratios as in **(d-e)**. All images are plotted in log scale and share the same colormap.

3.3.4 Visible laser demonstration

The ptychography reconstruction algorithms are wavelength agnostic, providing diffraction-limited spatial resolution that scales directly with wavelength of the illumination. Likewise, the CCD works well for both visible and EUV detection. Thus, we validated operation of the system and verified its performance by demonstrating ptychographic imaging on two test samples using visible laser illumination, see Fig. 3.10(a).

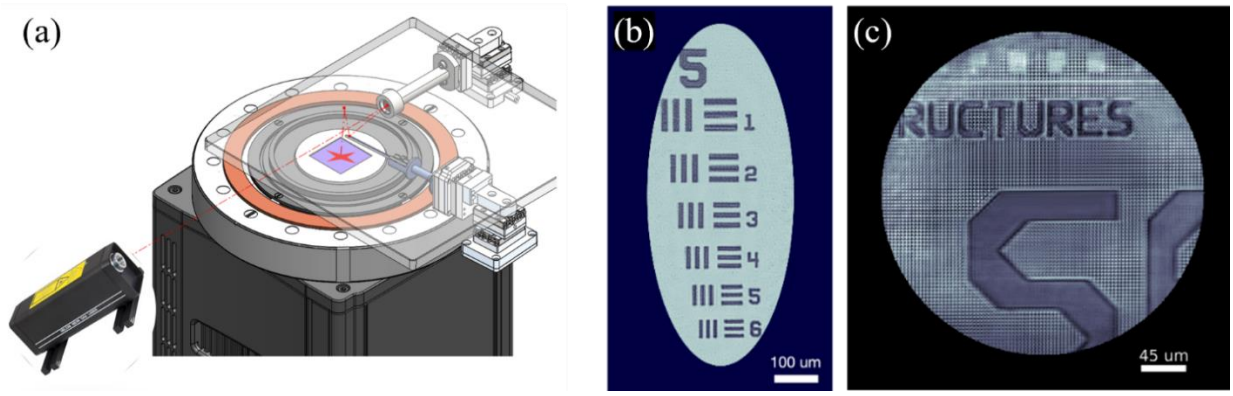

Figure 3.10: TEAMS system calibration and demonstration using visible lasers. (a) A schematic shows the coupling of a visible laser to the lensless imaging end-station for troubleshooting and preliminary demonstrations. **(b)** The amplitude of a ptychographic reconstruction of a 1951 USAF test target taken with a He-Ne laser at 632nm wavelength, showing excellent image quality and a spatial resolution of at least 17.54um (element 6 in group 5), while the diffraction-limited spatial resolution is 7.31um. **(c)** the amplitude of a ptychographic reconstruction of a semiconductor test sample from imec taken with a diode laser at 450nm wavelength.

Firstly, using a He-Ne laser at 632nm wavelength, we imaged a 1951 USAF test target. Figure 3.10(b) shows the amplitude of a ptychographic reconstruction of a 1951 USAF test target. The smallest features in this field of view, i.e., the horizontal and vertical bars from element 6 in group

5 with 8.77um linewidth, are clearly resolved with excellent fidelity, corresponding to a spatial resolution of at least 17.54um, while the diffraction-limited resolution is calculated to be 7.31um. Secondly, we used a diode laser at slightly shorter wavelength, 405nm, to image a semiconductor sample from imec [20]. This sample is more challenging for two reasons: (1) The sample has low contrast, which leads to low diffraction efficiency into high orders and low SNR; (2) The sample is covered with 2D periodic arrays (a 3.6um pitch) of square pillars (1.8um lateral size), which is challenging for ptychography due to the lack of diversity in diffraction patterns [18,145,147]. The amplitude image of a ptychographic reconstruction is shown in Fig. 3.10(c), where the large features, such as the letters and the squares, are clearly resolved while the 2D periodic arrays still need improvement. This can be accomplished by better system calibration and alignment, using other test samples with higher contrast (either in amplitude or phase), and detector cooling or high dynamic range for higher SNR.

3.3.5 EUV actinic imaging results

In this section, we successfully used TEAMS to image the nanoscale line-space (L/S) structures in an EUV photomask provided by imec. The full EUV HHG beamline starts with the $XUUS_4$ to generate the illumination. The EUV is separated from the infrared driving laser first by reflecting from two rejector mirrors that transmit the driving laser and reflect the EUV beam, and then using 800nm-thick Zr filters to further filter out lower-order harmonics with a ~6% transmission at 13.5nm wavelength. An in-vacuum adjustable iris ~3 meters after the source is used to define the EUV mode. After it enters the end-station, the EUV beam reflects off the two Si/Mo multilayer mirrors, M_S and M_F, which selects out a single wavelength at 13.5nm with a combined reflectivity of ~50%. The total flux at 13.5nm incident onto the EUV photomask was estimated to be about

$2.3x10^8$ photons per second. A 16-bit EUV-CCD camera is installed approximately 40mm away from the EUV photomask, which is equivalent to a numerical aperture (NA) of 0.3456 and a pixel size of 20nm in the reconstructed image. The EUV-CCD camera was cooled to -20°C under ultra-high vacuum to reduce the noise level. The sample is an EUV photomask from imec that is designed to perform defectivity testing on 27nm L/S patterns—27nm half-period on the wafer corresponding to 108 nm half pitch on the mask itself. The ptychography scans were carried out by laterally scanning the spherical Si/Mo multilayer mirror, M_S, causing the beam focus to move along with the mirror without changing the beam profile. We acquired a ptychography scan at 100 scan positions arranged in a 10 x 10 rectangular grid, with average nearest-neighbor spacing of 200nm and random offset at each position of up to 40nm to avoid gridding artifacts. The CCD integration time is set to 10 second, which nearly saturates the CCD. The far-field diffraction patterns consist of several completely separated diffraction orders, and the diffraction efficiencies slightly change as one scans the beam relative to the periodic L/S pattern. The complex images of the sample and the beam are reconstructed simultaneously using the ePIE algorithm [61]. The reconstructed beam in the sample plane is shown in Fig. 3.11(a), with a $1/e^2$ diameter of ~ 1um. A lineout of the beam intensity along the white dashed line in Fig. 3.11(a) is shown in Fig. 3.11(b). In the reconstruction process, we also applied total variation (TV) regularization to improve reconstruction fidelity. More specifically, every 5 reconstruction iterations, we used an open access TV regularization package [148] with a regularization parameter of 0.005 on the real and imaginary parts of the sample image in the high-fidelity region, and used as the object guess for the next iteration the mean of the regularized and original images. The TV regularization greatly suppressed the noise in the reconstruction and made the grating lines very sharp, as shown in Fig. 3.11(c) and 3.11(d) for the amplitude and phase, respectively. Moreover, we averaged the

amplitude and phase of the reconstructed L/S pattern along the line direction, and plotted the lineouts in Fig. 3.11(e) and 3.11(f).

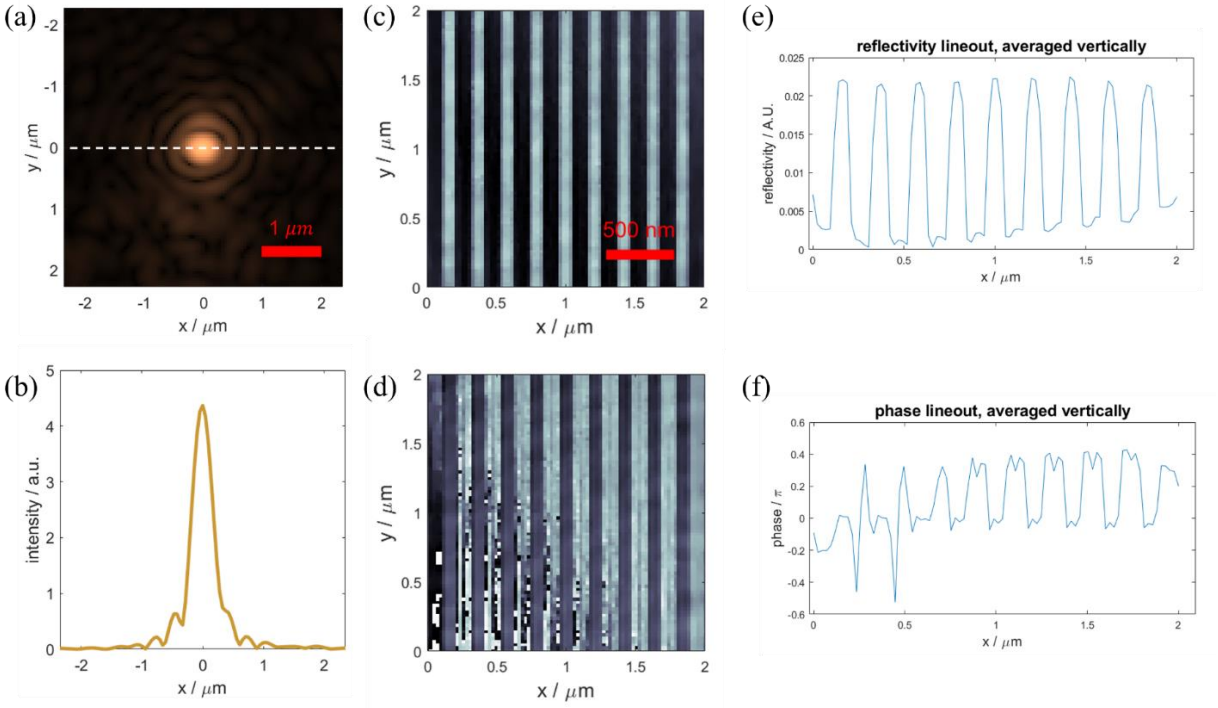

Figure 3.11: Actinic ptychographic imaging of EUV photomasks using TEAMS. (a) The reconstructed beam intensity at 13.5nm wavelength. A lineout along the white dashed line is shown in **(b)**. **(c-d)** The reconstructed amplitude and phase images of the 27nm L/S patterns on the EUV photomask. **(e-f)** The averaged cross-section of the 27nm L/S patterns.

3.4 Discussions

The goal of TEAMS is to perform high-fidelity inspection and imaging of EUV photomasks at high enough speed that meets the industry standards. We are currently working on system upgrade: (1) designing and installing a new EUV focusing module to deliver a focused beam with a higher illumination NA, which will improve the imaging fidelity and reliability; and (2) improving imaging throughput by taking advantage of state-of-the-art EUV CMOS cameras, which have a readout frame rate of about 20 frames per second as opposed to 0.5 frames per second for EUV

CCD cameras. Improvements in efficiency of the EUV beamline, for example, by reducing the Zr filter thickness from 800nm to 200nm can increase the beamline efficiency by an order of magnitude and allow us to take advantage of these higher frame rates.

In summary, we successfully implemented a tabletop EUV actinic microscope system (TEAMS) combining HHG and ptychography. We accomplished system calibrations and proof-of-concept demonstrations of ptychographic imaging capability by first using visible lasers to image some test samples and then using an HHG source at 13.5nm to image L/S patterns in an EUV photomask. Several future upgrades of the system are planned to achieve fast, reliable and high-fidelity inspection and imaging of EUV photomasks.

Chapter 4: EUV ptychographic imaging of highly periodic nano-structures

In the modern ptychography community, reseachers always believe that ptychography, which is a powerful variation of coherent diffractive imaging, does not work well for periodic structures, which greatly limits its potential applications in certain fields. On the other hand, ptychography has been proven by many researchers from all over the world to be a powerful and robust technique for EUV/x-ray imaging of a wide variety of samples, such as biological samples, semiconductor circuits, etc., which is much more complicated in structure than the simple periodic structures. These observations are quite counter-intuitive. In this chapter, we proposed and demonstrated an illumination engineering technique that allows us to achieve fast and reliable ptychographic imaging of periodic structures, which resolves the counter-intuitive observation and can potentially be applied to semiconductor photomask metrology and many other fields.

4.1 Introduction

Over the past couple of decades, ptychography has enabled robust, diffraction-limited, phase contrast imaging of systems down to the nanoscale [18,20,56,62-64,149-151]. In ptychography, a coherent illumination, called the probe, is focused and scanned laterally across an extended sample, and a series of far-field diffraction patterns are recorded at each scan position while keeping a large area overlap among adjacent scan positions. Iterative phase-retrieval algorithms [49,55,61,152] are used to reconstruct the complex sample and illumination functions robustly and uniquely. The successful implementation of high-fidelity ptychographic imaging heavily relies on, among many other factors, (1) the data redundancy provided by overlapping illumination areas during scanning, and (2) the data diversity provided by the lateral scanning of the illumination

relative to the sample. Ptychographic imaging of highly periodic samples is extremely challenging due to the lack of data diversity in the series of diffraction patterns, leading to poor convergence in the reconstructed sample images. This is a significant drawback and limitation, as nanoscale periodic structures are present in a wide variety of samples including optical components like zone plates [18], photonic crystals [153,154], semiconductor devices [44], and especially EUV photomasks [145, 155-160]. Advanced metrology techniques that enable reliable imaging of nanoscale periodic structures and localization of critical defects within them are crucial for the development, performance and manufacturing of these highly periodic nanostructures. Consequently, it is extremely critical to fill this characterization gap to aid the advancement of a host of next-generation nano-devices.

In this chapter, I will first give a historical overview of this problem described above and borrow some ideas from past demonstrations to tackle this challenge. Then, I will present experimental evidences in support of our imaging technique. Finally, I will go one step further and demonstrate improved imaging quality by illumination design.

4.2 Borrowing wisdom from the past

Nowadays, when people talk about ptychography, especially in the major optical/EUV/x-ray ptychography community, the first thing that comes to their mind is either Rodenburg's demonstration of phase retrieval using a shifting illumination in 2004 [59], or the fancy algorithms developed by various researchers for phase retrieval, for example, extended ptychographical iterative engine (ePIE), difference map (DM), maximum likelihood (ML), etc. However, people in the community of crystallography and/or electron diffraction would probably very much disagree because they have quite different perspectives about the history of ptychography. In order

to understand the divergence and fill in the gap between these two groups of people, let us take a tour about the history of ptychography from the very beginning.

The earliest introduction of ptychography was actually by *Walter Hoppe et al.* between 1969 and 1972 [57,161,162] to describe a method of calculating the phase of the Bragg reflection peaks from a crystal. If a localized electron beam illuminates a crystal, the Fraunhoffer diffraction pattern is a convolution of the crystal's Bragg reflection with the Fourier transform of the illumination function. The coherent illumination was tightly focused such that its Fourier transform is wide and the Bragg peaks, which are usually small spots, are made to overlap and interfere with one another (or in German *Faltung*, folding). Hoppe conjectured that this interference effect could be used to estimate the phase difference between any pair of overlapping diffraction orders with an ambiguity of a complex conjugate. By shifting the illumination relative to the sample, the Fourier shift theorem further resolves this ambiguity. Consequently, Hoppe used the word "*ptycho*", which comes from the Greek word "*πτυξ*" meaning "*to fold*", to refer to the convolution theorem, or rather the "*folding*" of diffraction orders into one another via the convolution theorem. It is a fair guess that Hoppe *et al.* were following the example set by Gabor, who constructed the term *holography* from Greek "*ολο*", meaning "*whole*": the whole wave distribution being both its modulus and phase. Like holography, ptychography tries to reconstruct the entire wave field scattered from an object. Unlike holography, it does not require a reference beam, instead, it extract the phase information by interfering multiple, at least two, diffraction orders. Twenty-five years later, this idea was then re-visited and demonstrated using transmission electron microcopy by Nellist, Chapman and Rodenburg [58] to image atoms in a crystal of silicon, shown in Fig. 4.1.

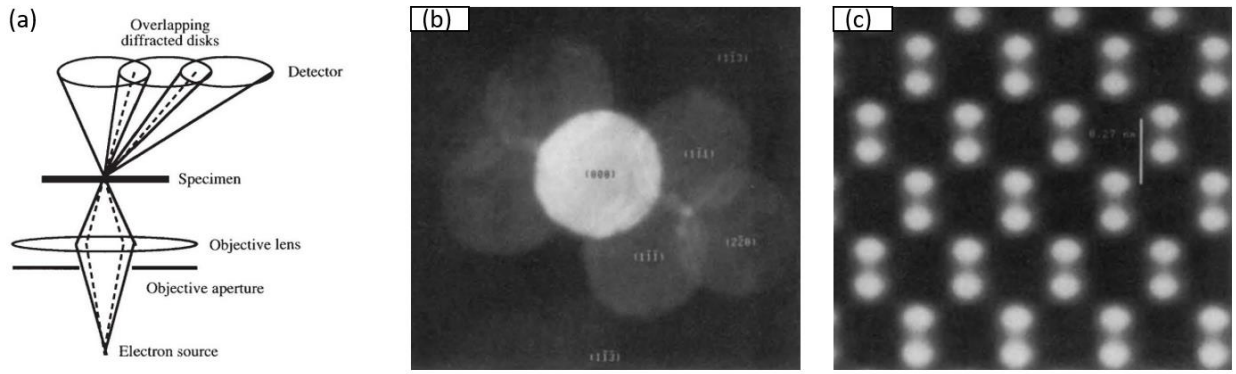

Figure 4.1: First demonstration of ptychography using transmission electron microscopy. (a) Schematic diagram of the principle of ptychography using STEM. **(b)** An example of a microdiffraction pattern of silicon, where interference fringes can be seen in the disk overlap regions. **(c)** The phase of the reconstructed image, which shows that all the atomic columns are resolved. Figure adapted from [58].

However, modern ptychography, mostly using coherent photons instead of electrons, has very little in common with this original concept and demonstration, but for historical reasons, the name has stuck. The big explosion of interest in ptychography began in 2007, starting in the x-ray synchrotron microscopy community [62,63,163] to meet the high demand for high-resolution x-ray imaging of general, aperiodic samples. For these general samples, their Fourier representation is rather widely distributed, which makes the '*folding*' of diffraction orders into one another happen natrually. On the contrary, in the case of periodic samples whose Fourier representations are sparse, one has to carefully design the illumination to achieve diffraction overlap in the Fraunhoffer field. Without realizing this by most of researcher in this field, ptychographic imaging of highly periodic structures is considered to be extremely difficult.

To summarize, it is quite interesting, but unfortunate, that people from the electron microscopy and the x-ray (now extended to other wavelength regime including visible and EUV light) microscopy communities have quite distinct perspectives about ptychography. I personally

attribute it to the fact that the momentum of the development of ptychography-based microscopy techniques in the EUV/x-ray regime is so strong that researchers tend to forget or forget to ask where it actually comes from.

4.3 Methodology

Periodic structures (in real space representation) usually have a sparse representation in Fourier space (meaning that only very few spatial frequency component have a non-zero amplitude). Three examples are shown in Fig. 4.2 of a 1D line-space structure in (a,d), a 2D square lattice structure in (b,e), and a 2D hexagonal lattice structure in (c,f), where (a-c) are the real space representations and (d-f) are the Fourier space representations. When illuminated by a focused beam with a full convergence angle of α, these periodic structures will produce characteristic far-field diffraction patterns, which is the convolution of the Fourier transform of the periodic structure (consisting of many diffraction orders arranged in a periodic grid with modulated amplitude and phase) and the Fourier transform of the in-focus beam (which is simply the far-field beam profile). The diffraction orders have an angular separation between adjacent orders of $\beta = sin^{-1}\frac{\lambda}{\Lambda}$, where Λ is the pitch of the 2D periodic structure and λ is the wavelength of the beam. Depending on α and β, these diffraction orders will either be completely isolated from each other, as in Fig. 4.3(a), or partially overlap with one another, as in Fig. 4.3(b). For a certain combination of illumination wavelength λ and sample period Λ, there exists a critical value $\alpha_c = sin^{-1}\frac{\lambda}{\Lambda}$ for the full convergence angle of the illumination. The corresponding critical illumination NA is given by:

$$NA_c = \frac{1}{2}sin\alpha_c = \frac{\lambda}{2\Lambda} \qquad (5.1)$$

Only when above this critical value can interference happen between diffraction orders. If the diffraction orders are isolated and thus not interfered, the diffraction patterns are insensitive to the

illuminated position on the sample, making it difficult or impossible for the phase retrieval algorithms to reconstruct an image. On the other hand, if the diffraction orders are overlapped, interference fringes will appear and shift as the beam is scanned across the sample, giving direct information about the relative position between the illumination and the sample, and enabling robust image reconstruction.

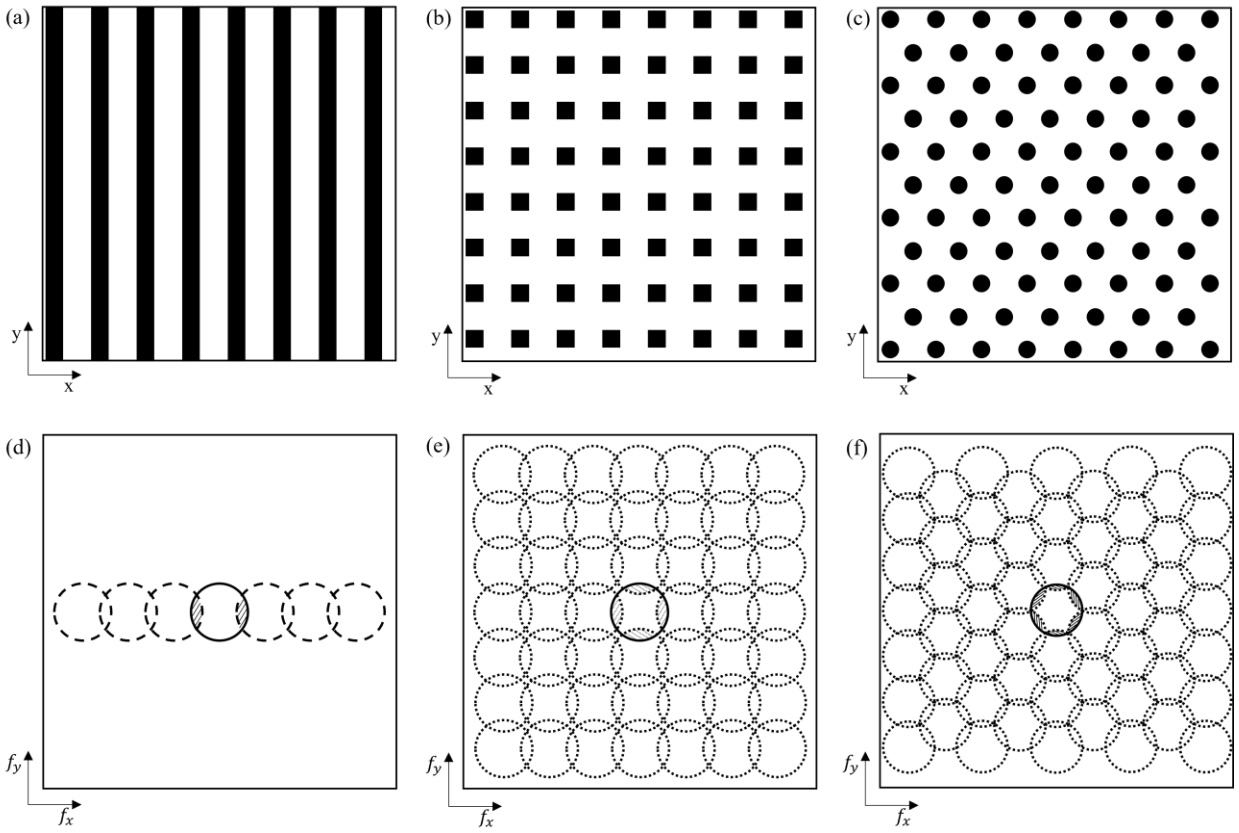

Figure 4.2: Representations in real (*x*-*y*) and Fourier spaces (f_x-f_y) of three kinds of periodic structures. (a,d) One-dimensional line-space structures. **(b,e)** Two dimensional square grids. **(c,f)** Two dimensional hexagonal lattices.

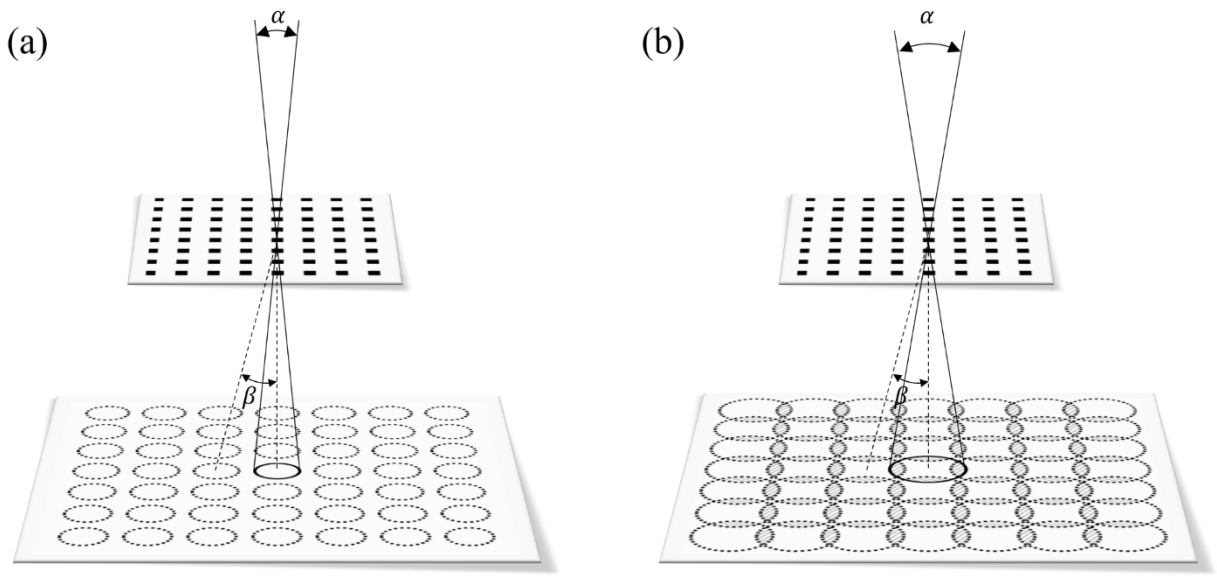

Figure 4.3: Schematic representations showing that the key to imaging periodic structures using ptychography is to enforce diffraction orders to overlap and interfere in the detector plane. In (a), the divergence angle of the 0^{th} order is smaller than the angular separation between adjacent diffraction orders, resulting in no overlap in the detector plane and inhibiting image reconstruction. In (b), the divergence angle of the 0^{th} order is increased to be larger than the angular separation between adjacent diffraction orders, so interference begins to happen in the overlap regions, allowing reliable and robust reconstructions of periodic samples.

Experimentally, an easy way to achieve interference is to increase numerical aperture (NA) of the illumination onto the sample such that each diffraction order is large enough in the far-field to overlap with one another. For a fixed illumination wavelength, this can be achieved by either increasing the divergence angle of the light source, or using focusing optics with shorter focal length.

A characteristic, phase-change-like behavior is expected to happen as one smoothly increases the illumination NA, as shown in Fig. 4.4. For 2D periodic structures with a certain pitch, for example 9 um as indicated in blue, and illumination with a certain wavelength, for example 56 nm in this study, there exists a critical value for the illumination numerical aperture, NA_c =0.00311, given

by Eq. (5.1). Below the critical NA_c, diffraction orders do not overlap in the detector plane, thus ptychographic reconstructions are not reliable, while above the critical NA diffraction orders overlap with one another, leading to fast and high-quality reconstructions with minimal grid artifacts. In the presence of experimental noise, the reconstruction is expected to be improved as illumination NA increases. For 2D periodic structures with smaller periods, for example 4.5 μm and 3 μm pitches, the critical NA increases accordingly to 0.0062 and 0.0093, as shown in yellow and red in Fig. 4.4, respectively.

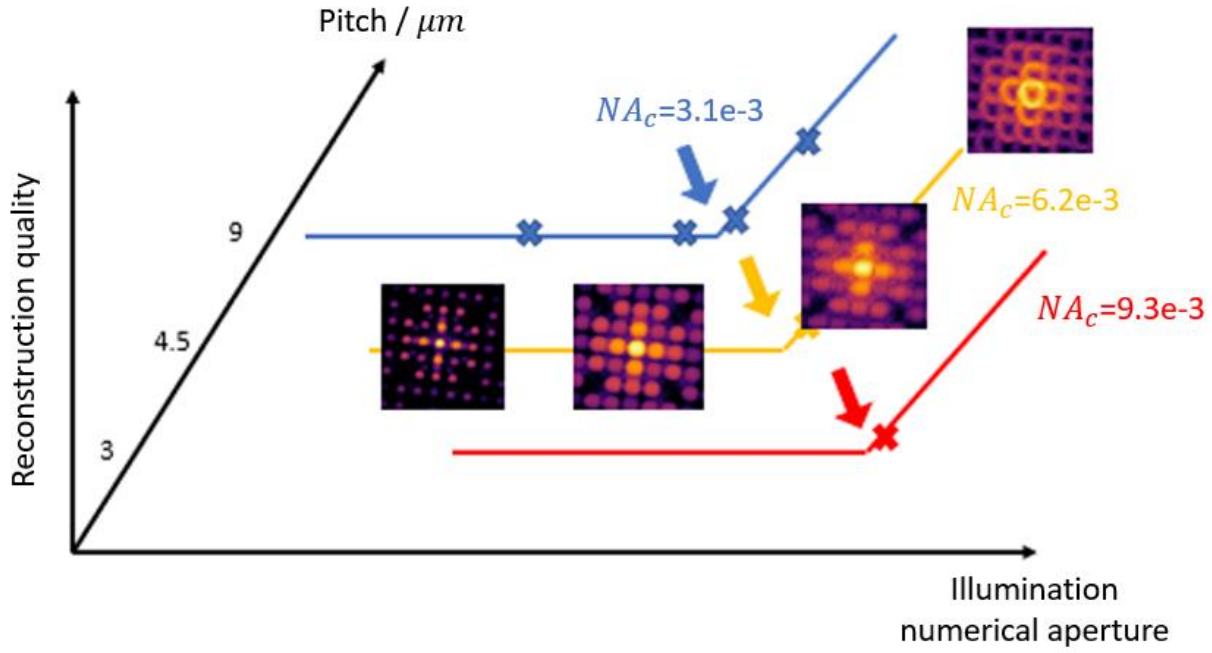

Figure 4.4: A schematic phase diagram in ptychographic imaging of periodic structures indicating reconstruction quality as a function of sample period and illumination NA. For a specific sample period, blue for 9 μm, yellow for 4.5 μm and red for 3 μm, a critical illumination NA has to be realized in order to do successful ptychographic reconstructions.

4.4 Experimental configuration

We built an EUV ptychographic microscope in transmission geometry using high harmonic generation (HHG) illumination to experimentally verify our proposed technique. We demonstrated that it is capable of imaging highly periodic samples, either with a Gaussian mode or carrying orbital angular momentum (OAM) of vortex charge $\ell = 7$. The experimental set-up is quite similar to that used in section 2.2. We will omit the similar part of these two set-ups and describe in detail the difference. A schematic diagram of the set-up is shown in Fig. 4.5. Again, we first use an amplified Ti:sapphire ultrafast laser (790nm central wavelength) to generate SHG (395 nm central wavelength) in a β-BBO crystal. This SHG beam is then focused into a semi-infinite gas cell (SIGC), which consists of a Brewster-cut entrance window, a 20 cm length filled with 50 torr of argon gas, and a copper gasket placed in the focal plane of the driving laser where a coherent HHG beam is generated [164,165]. The driving laser is separated from the high-harmonic beam by using a 200 nm aluminum filter. The resulting EUV beam after the aluminum filter consists of narrow peaks at the 7^{th} (λ = 56 nm) and 9^{th} (λ = 44 nm) harmonics. The intensity ratio of the two harmonics in our experimental setup is estimated to be $I_{\lambda=56nm}/I_{\lambda=44nm}$ ~ 30:1, which can be well-approximated as a monochromatic illumination suitable for ptychographic imaging. For generating HHG beams with a Gaussian spatial profile, we used an SHG beam with pulse energy of ~ 500 μJ. For generating HHG beams carrying OAM, we increased the pulse energy of the SHG beam to ~1.5 mJ, and inserted a spiral phase plate (Holo-Or) to generate a driving beam with OAM charge number ℓ = 1, and λ = 395 nm. The increased pulse energy is necessary in order to make the peak intensity (which is located at a central point for Gaussian beams, but is distributed in a ring for the OAM beams) equal for the two cases, in order to match HHG cutoff energies and conversion

efficiency. Due to the conservation of OAM in HHG, the resulting quasi-monochromatic 7th harmonic beam (λ = 56 nm) carries an OAM charge number of ℓ = 7 [166-168].

After entering the imaging end-station, the HHG beam is focused sequentially by two toroidal mirrors (toroidal mirror #1: B_4C-coated, f_{eff} = 27 cm, θ = 15°; toroidal mirror #2: Au-coated, f_{eff} = 50 cm, θ = 10°) in a Wolter configuration to create an focusing system with higher NA (f_{eff} = 17 cm) while managing coma aberration [169]. The resulting focusing beam is redirected towards the sample at normal incidence using a glancing incidence mirror (B_4C coating, fused silica substrate, 3° incidence angle from grazing, nominal reflectivity 95%). The testing samples are three Quantifoil holey carbon films which have various hole sizes and shapes arranged in a rectangular grid, and are mounted on standard Ted Pella Ø3mm Cu TEM grids with 200 mesh (125 um pitch, 90 um hole width and 35 um bar width). More specifically, the three Quantifoil holey carbon films have a pitch of 9 um (7 um square hole and 2 um bar, product number 656-200-CU from Ted Pella), 4.5 um (3.5 um diameter circular holes and 1 um separation, product number 660-200-CU) and 3 um (2 um diameter circular holes and 1 um separation, product number 661-200-CU), respectively. The samples are positioned close to the beam focus (~ 30 um diameter for Gaussian HHG beams, and ~ 40 um diameter for OAM HHG beams), and are mounted on a precision translation stage ensemble (SmarAct XYZ-SLC17:30). They are translated in the plane perpendicular to the beam path to perform ptychographic scans in 7 x 7 rectangular grids (49 positions) with nominally 3.3 um between adjacent positions. A random offset of $\pm$20% of the scan step size was added to each scan position to avoid artifacts originating from the scan grid itself. The far-field diffraction patterns are recorded by an EUV-CCD detector (Andor iKon-L, 2048 x 2048, 13.5 um pixel size) positioned about 50 mm after the sample. In order to obtain the best ptychographic reconstructions possible for each illumination case, we carefully characterized

each illumination function in the sample planes by taking ptychographic scans on a non-periodic sample and reconstructing both the sample and the illumination function through blind deconvolution. The reconstructed illumination functions were then used in the ptychographic reconstructions of highly periodic samples as initial guesses.

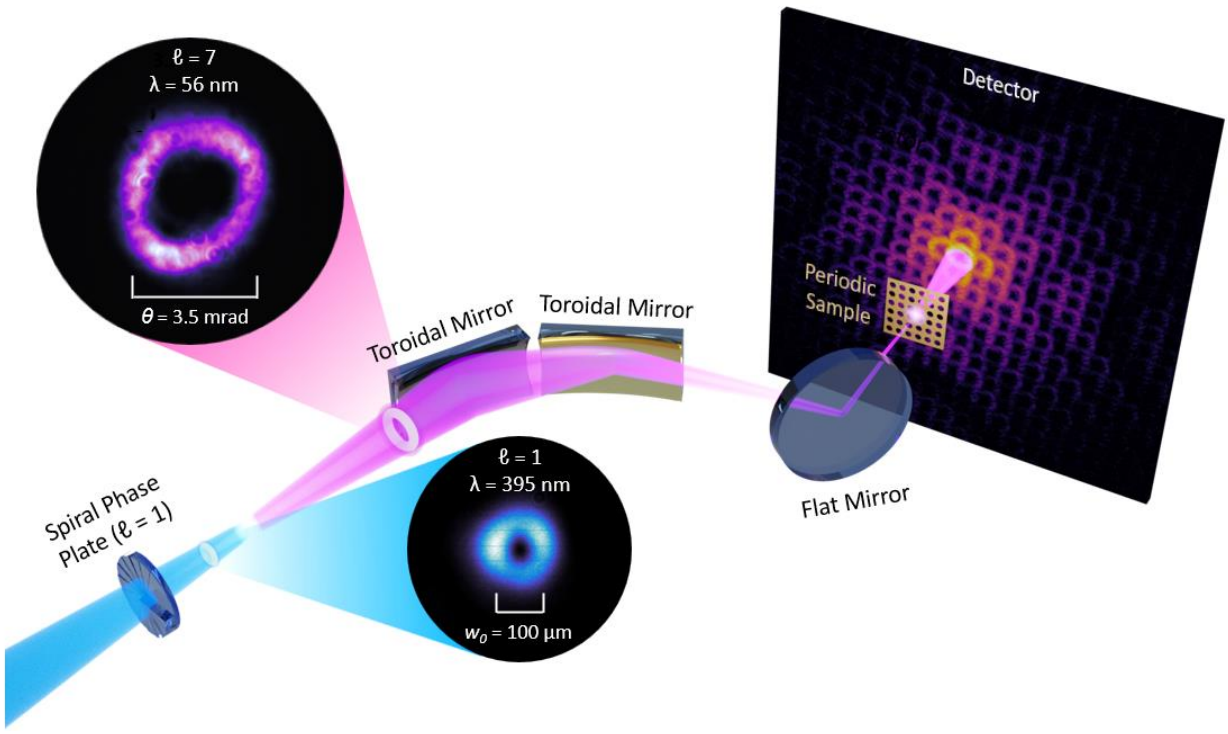

Figure 4.5: Schematic diagram of the experimental set-up for ptychographic imaging of highly periodic structures. A quasimonochromatic beam at ~56 nm wavelength (either with a Gaussian mode or carrying OAM l=7) is generated via HHG. It is then focused by a double-toroid system onto the periodic structures to produce characteristic far-field diffraction patterns.

4.5 Experimental results

4.5.1 Gaussian-HHG illuminations with controlled NA demonstrate a phase-change-like behavior in ptychographic imaging of periodic structures

For the first part, we demonstrated the phase-change-like behavior in ptychographic imaging of highly periodic structures, as shown in Fig. 4.6, using Gaussian HHG beams with controlled beam divergence (equivalent to illumination NA). An in-vacuum iris is inserted ~ 0.5 m after the SIGC to allow direct control on the divergence of the HHG beams. We chose four different iris aperture sizes such that the illumination NAs onto the sample are 0.0005, 0.0025, 0.0045, and 0.0065, and tested them on the two 2D periodic structures with 9 um pitch. As shown in Fig. 4.6(a,c), these two ptychography datasets on the 9-um pitch sample with illumination NA = 0.0005 and 0.0025 (smaller than the critical value NA_c=0.0031) cannot be reconstructed because the diffraction orders are isolated and no interference happened (see the insets), and the reconstructed images are heavily corrupted by gridding artifacts, see Fig. 4.6(b,d). As the illumination NA is increases to 0.0045 and 0.0065 (larger than the critical value NA_c=0.0031), interference happens, as shown in Fig. 4.6(e,g) and the insets, and high-fidelity images are reconstructed within only a couple of hundreds of iterations, as shown in Fig. 4.6(f,h). All datasets have a similar total number of photons collected by the EUV-CCD.

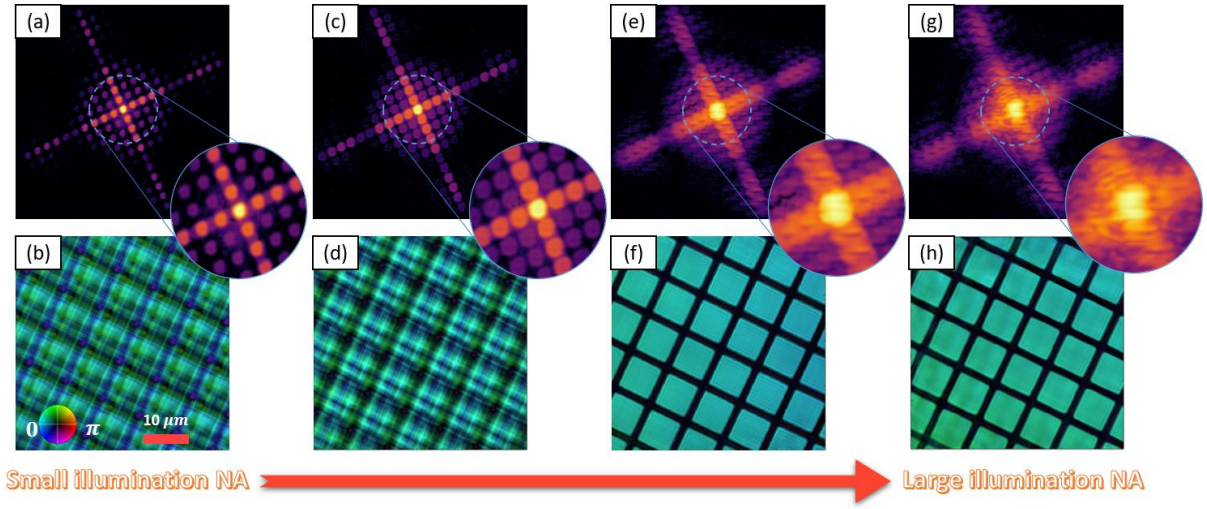

Figure 4.6: A phase-change-like behavior is demonstrated by Gaussian-HHG illuminations with controlled divergence. (a-b) A Gaussian beam with small divergence angle, controlled by an in-vacuum iris, is not capable of imaging the specific periodic structures because the diffraction orders do not overlap. **(c-d)** The corresponding ptychographic reconstructions failed. **(e-f)** With a larger in-vacuum iris aperture, diffraction orders start to overlap and high-fidelity reconstruction can be achieved within a few hundreds of iterations. **(g-h)** With the in-vacuum iris aperture further increased, the interference fringes increase in SNR, leading to better reconstruction quality.

4.5.2 OAM-HHG illuminations enable higher-fidelity imaging than Gaussian-HHG

Due to the conservation of OAM in the HHG process and the resulting high spatial frequency content in the generated EUV beam, OAM HHG beams naturally have a significantly increased beam divergence (equivalent to illumination NA) compared to that of Gaussian HHG beams. This optically enhanced illumination NA allows us to achieve area overlap among diffraction orders for smaller pitch periodic samples beyond what is possible with the Gaussian probe, without making any changes to the focusing optics. Furthermore, the donut-shaped intensity distribution of OAM HHG beams ensures that the majority of photons fall in the overlap area (in contrast to the Gaussian beam, for which the overlap between diffraction orders occurs at the tails of the intensity

distributions), which increases the SNR for the interference fringes. Here, we demonstrate that these two intrinsic advantages of OAM HHG beams enable ptychographic imaging of highly periodic structures with higher quality than the corresponding Gaussian HHG beams.

To generate OAM HHG beams, we used a driving laser with $\ell = 1$ to generate a 7^{th} harmonic beam carrying OAM $\ell = 7$. As shown in Fig. 4.5, we tested Gaussian and OAM HHG beams, both with the in-vacuum iris fully open, on three periodic structures with 9 um, 4.5 um and 3 um pitches. For the 9 um pitch sample, Gaussian beams can produce a decent image with some artifacts, while OAM beams manage to remove most of the gridding artifacts and result in a much higher-fidelity image that can be further used for defect analysis (see section 4.5.3). Moreover, for the 4.5 um pitch sample, Gaussian beams are barely able to produce reliable images, but the OAM beams are still able to produce high-quality images. Lastly, for the 3 um pitch sample, Gaussian beams totally failed due to the lack of interference in the diffraction patterns, while OAM beams still managed to image the general periodic structure, even though the quality of the unit cell is poor. All datasets have a similar total number of photons collected by the EUV-CCD. We also took SEM images of these three samples and overlaid them with the reconstructed images from our technique, as shown in Fig. 4.8, which shows great agreement.

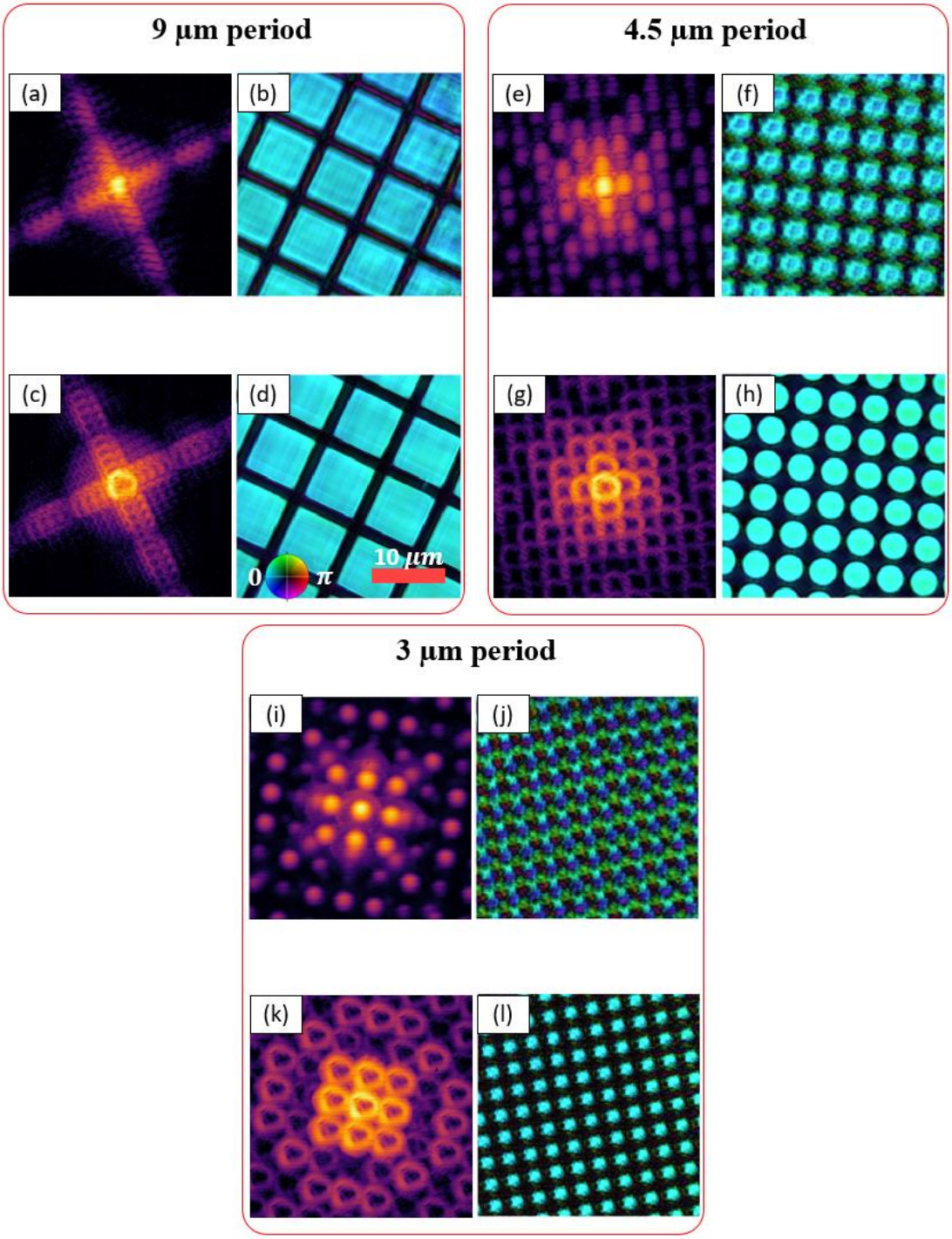

Figure 4.7: Comparison of ptychographic imaging quality from Gaussin and OAM HHG illuminations. (a-b) An example diffraction pattern and the reconstructed 9 μm pitch sample using Gaussian HHG beams. **(c-d)** An example diffraction pattern and the reconstructed 9 μm pitch sample using OAM HHG beams. **(e-h)** Similar results for the 4.5 μm pitch sample. **(i-l)** Similar results for the 3 μm pitch sample.

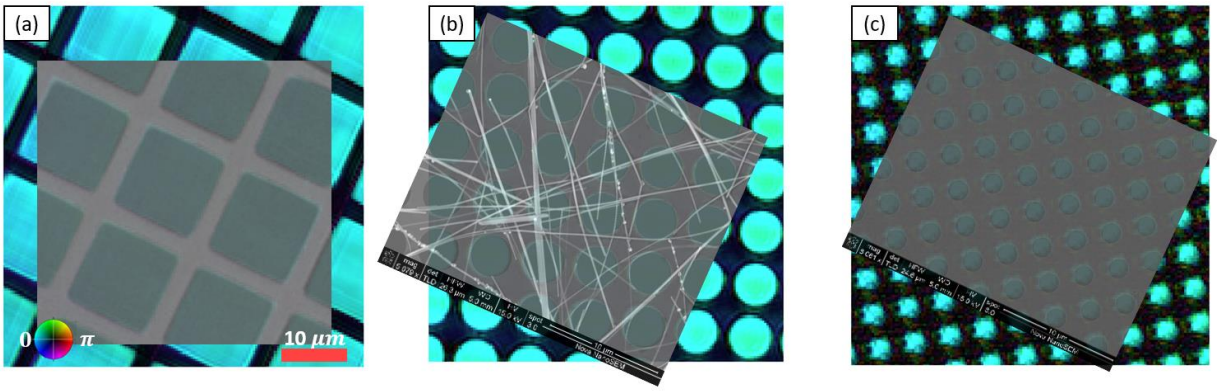

Figure 4.8: Reconstructed images from OAM HHG illuminations overlaid with SEM images of the same sample area on the 9 μm **(a)**, 4.5 μm **(b)**, and 3 μm **(c)** samples.

4.5.3 OAM-HHG illuminations reveal nanoscale defects in otherwise periodic structures

A major motivation for wanting to image periodic structures is to reliably observe and pinpoint small areas where the periodicity is broken, *i.e.*, defects. For the cases where the diffraction orders are insufficiently overlapped, the artifacts in the ptychography reconstructs make it difficult or impossible to locate these defects. Here, we observed that the increase in reconstruction quality granted by using OAM HHG probes enables reliable localization of nanoscale defects in otherwise highly periodic structures. This can potentially find its application in metrology for micro- and nano-fabrication and manufacturing, including the most advanced EUV lithography. In the 9 um pitch sample, there is a broken carbon bar as shown in the SEM image in Fig. 4.9(g). We performed ptychographic imaging in transmission using Gaussian HHG beams. An example diffraction pattern is shown in Fig. 4.9(a), and the reconstructed image is shown in Fig. 4.9(b), where reconstruction artifacts heavily corrupt image details and makes the defect invisible. Next, a similar experiment is performed with OAM HHG beams under otherwise the same condition, resulting in roughly the same max count in the diffraction patterns as that in the OAM case (meaning similar SNR in the datasets). The reconstructed image is shown in Fig. 4.9(d), in which

the defect is clearly resolved and is indicated by the yellow circle. Furthermore, the SEM image in Fig. 4.9(g) shows that the defect is about 289 nm in width, which is close to the diffraction-limited resolution of the current microscope (200nm).

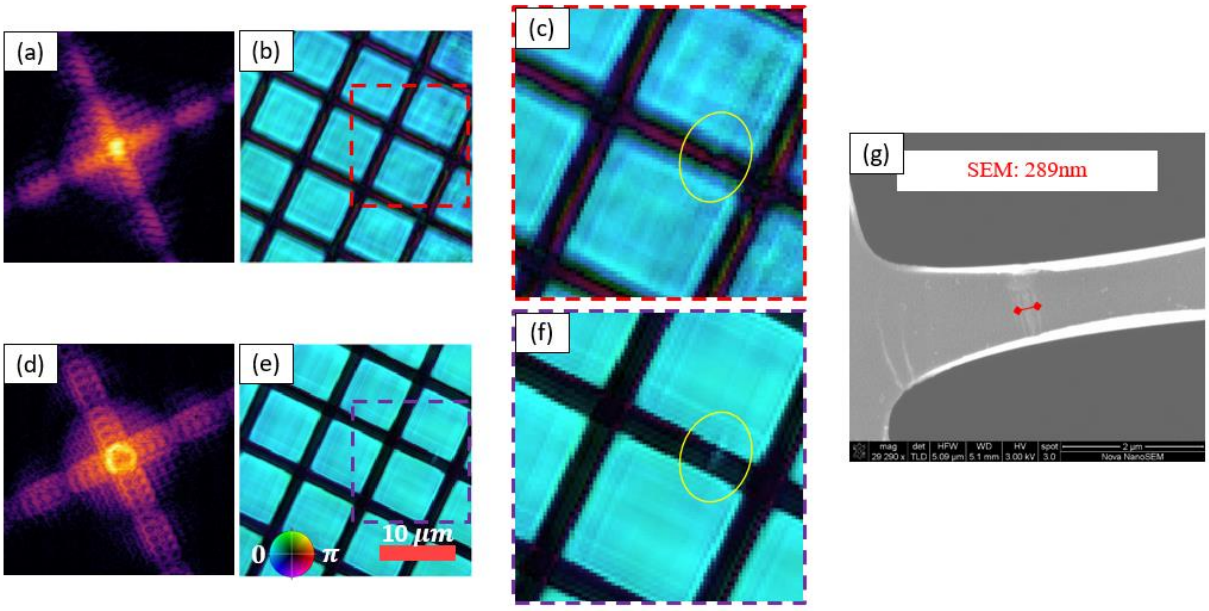

Figure 4.9: Comparison of Gaussian and OAM HHG illumination for nanoscale defect inspection. An example diffraction pattern **(a)** and the reconstructed image **(b)** of a 9 μm pitch sample using Gaussian HHG illuminations. A zoomed-in view of the red box in **(b)** is shown in **(c)**, where the nano-defect is heavily corrupted by the reconstruction artifact. Similar figures from OAM HHG illuminations are shown in **(d-f)**, where the gridding artifact is significantly surpressed and the defect is clearly revealed. **(g)** An SEM image of the same sample area, showing a defect of 289 nm x 2 μm.

We show the measured/reconstructed Gaussian and OAM HHG beams in three different planes, as shown in Fig. 4.10. The intrinsic divergence for Gaussian and OAM HHG beams are characterized by directly recording the beam on a disgnostic camera without reflecting off any curved surface, and the intensity profiles are shown in Fig. 4.10(a). The Gaussian and OAM beams in the sample plane were reconstructed through ptychography and their complex fields are shown

in Fig. 4.10(b) with intensity encoded in brightness and phase encoded in hue. The beam profiles in the detector plane can be calculated by propagating the beams in the sample plane to the detector plane, and are shown in Fig. 4.10(c).

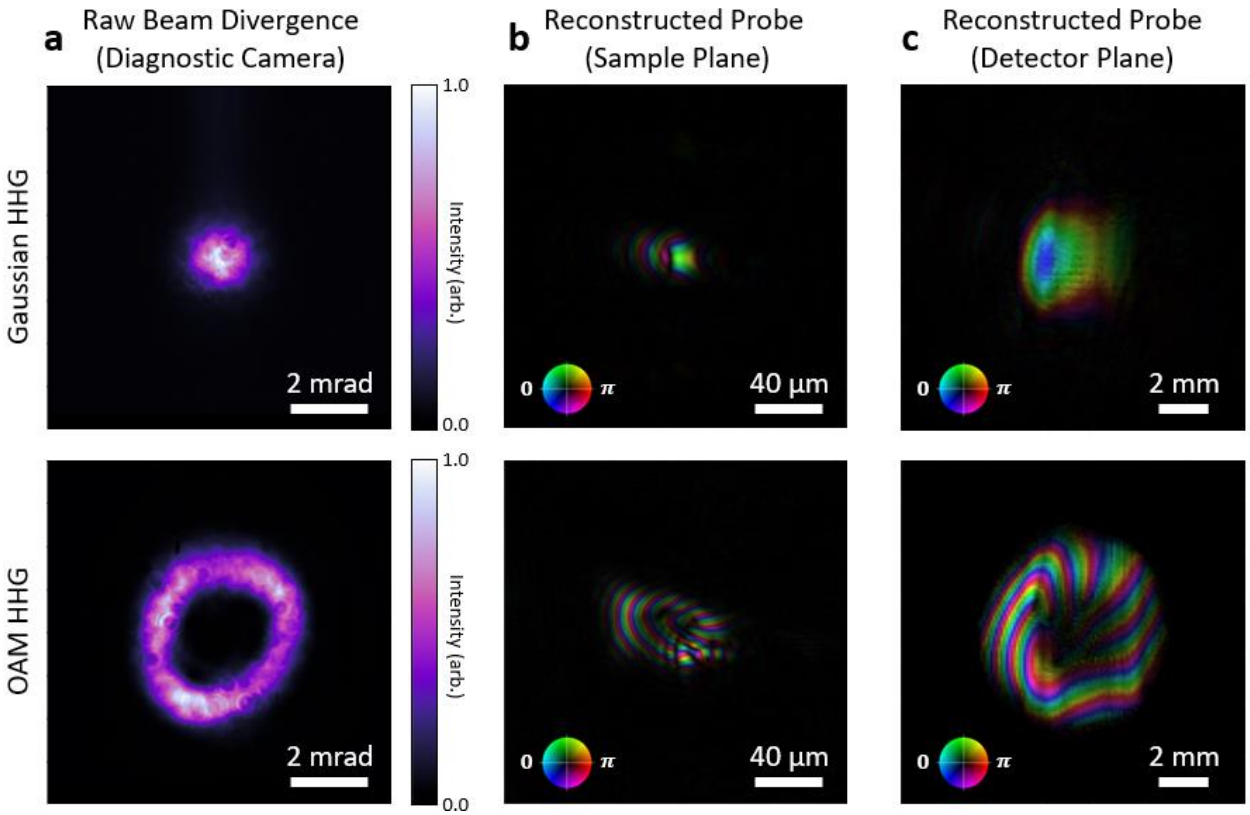

Figure 4.10: Gaussian and OAM HHG beam profiles in different planes. (a) Intensity profiles of the Gaussian and OAM HHG beams 1.5m after they are generated without focusing/defocusing optics in the middle. They are directly measured on a diagnostic camera. **(b)** The reconstructed Gaussian and OAM HHG beams in the sample plane. The beams are focused by a double-toroid system onto the sample. The intensity and phase are encoded in brightness and hue, respectively. **(c)** The reconstructed Gaussian and OAM HHG beams in the detector plane.

4.6 Conclusion

We have demonstrated reliable and robust ptychographic imaging of periodic structures using a coherent tabletop EUV source based on HHG. We verified that the key is to design the illumination

conditions such that the resulting diffraction orders have area overlap and interfere with each other in the far-field. This is experimentally accomplished with a Gaussian HHG beam with controlled divergence angle. We further converted our light source to carry OAM, which has a characteristic ring-shaped intensity profile and an intrinsic larger divergence. These properties of the OAM HHG beams allow us to achieve (1) better image quality than Gaussian HHG beams, and (2) successful ptychographic imaging of periodic structures with small pitches that is beyond what is possible for Gaussian HHG beams. Last but not least, we observed that OAM HHG illuminations are capable of providing nearly artifact-free ptychographic reconstructions of periodic structures, which allows us to spot diffraction-limited-sized defects in them. This is particularly interesting for the nano-metrology community, including semiconductor metrology.

Chapter 5: Summary and future directions

5.1 Summary

In this thesis, I have demonstrated several EUV lensless microscopes using tabletop high harmonic generation sources. In chapter 2, I showed how multiple mutually incoherent EUV modes, different in wavelength and/or being separated in time, can be simultaneously applied to perform ptychographic imaging to extract more sample information, i.e., spectral responses and/or larger sample field of views. This simultaneous implementation of temporal and/or spectral multiplexing in ptychography is a natural way to take full advantages of the unique properties of HHG light sources. This is achieved by adapting the ptychographic information multiplexing algorithm [68] and adding extra constraints for better convergence and higher reconstruction quality. This technique allows one to perform higher-throughput lensless imaging without increasing the amount of data needed. In chapter 3, I introduced our tabletop EUV actinic microscope system based on lensless imaging. It is specifically designed for defect inspection and analysis in EUV photomask samples. The system has been calibrated using various diagnostic methods, including sample-to-detector distance, angle of incidence, detector orientation offset, etc. Some preliminary actinic imaging results on 108 nm line-space structures have been reported with large amount of algorithmic effort (total-variation regularization). It turns out to be extremely challenging to image these one-dimensional line-space structures through ptychography, which is the major inspiration for chapter 4. In chapter 4, we proposed and demonstrated a novel technique that enables fast, reliable and robust ptychographic imaging of 1D/2D periodic structures by illumination engineering. We also compared imaging quality of periodic structures under two types of illuminations, *i.e.*, Gaussian and OAM HHG illuminations, and discovered that OAM HHG

illuminations are superior due to their ring-shaped intensity profile and larger intrinsic beam divergence. We believe that these findings can help fill in the metrology gap for advanced semiconductor and quantum devices, especially for EUV photomasks.

5.2 Future directions

There are several exciting extensions of the work presented in this thesis that I would like to share with the readers and hopefully some of them can be accomplished by future researchers in the Kapteyn-Murnane group.

First, in the multibeam ptychography experiments, it would be interesting to explore the maximum number of mutually incoherent beams allowed in this technique.

Second, the TEAMS hardware can be upgraded for high-throughput and high-fidelity imaging of EUV photomasks following these two general directions: (1) designing and installing a new EUV illuminating module to deliver a focused beam with a larger illumination NA to support the interference of diffraction orders, which will improve the imaging fidelity and reliability; and (2) improving imaging throughput by increasing source brightness and beamline efficiency, as well as taking advantage of state-of-the-art EUV CMOS cameras, which have a readout frame rate of about 20 frames per second as opposed to 0.5 frames per second for the current EUV CCD cameras. In terms of improving the EUV beamline efficiency, one can increase the beamline efficiency by almost an order of magnitude by reducing the Zr filter thickness from 800nm to 200nm.

Last but not least, as a new research topic, numerous opportunities exits in the exploration and optimization of the technique introduced in chapter 4.

- The experimental demonstration in chapter 4 used 56 nm wavelength EUV beams with an imaging NA of 0.138 and provided a diffraction limited resolution limit of ~ 200 nm. Future efforts can be devoted to combining shorter wavelength light and experimental setups with larger imaging NA to explore periodic structures with 10*s*-100*s* of nanometer pitches, for example those in EUV photomasks. The reconstructed phase information about the EUV photomasks are especially valuable for understanding and addressing mask 3D effects.
- Since illumination pattern is very critical for this technique, optimizing the illumination pattern can be valuable for real-world applications. Future effort can be devoted to figuring out the optimal illumination patterns for different lattice patterns (1D line-space structures, 2D rectangular structures, 2D hexagonal structures, etc.). In HHG, EUV beam mode and divergence can be controlled by tailoring the driving field using combinations of different vortex number, polarization states, etc [139]. Alternatively, by combining a Köhler illumination system with a fly's eye integrator, it is possible to create almost arbitrary illumination patterns in the EUV [170].

Bibliography

[1] [2018 Orji] N. G. Orji, M. Badaroglu, B. M. Barnes, C. Beitia, B. D. Bunday, U. Celano, R. J. Kline, M. Neisser, Y. Obeng, and A. E. Vladar, Metrology for the next generation of semiconductor devices. *Nat. Electron.* **1**, 532-547 (2018).

[2] [2000 Reimer] L. Reimer, Scanning Electron Microscopy: Physics of Image Formation and Microanalysis, 2nd edition, Springer (2000).

[3] [2018 Mohammed] A. Mohammed and A. Abdullah. Scanning Electron Microscopy (SEM): A Review, *Proc. of 2018 International Conference on Hydraulics and Pneumatics*, (2018).

[4] [2003 Jones] R. L. Jones, T. Hu, E. K. Lin, and W.-L. Wu, Small angle X-ray scattering for sub-100 nm pattern characterization. *Appl. Phys. Lett.* **83**, 4059–4061 (2003).

[5] [1997 Raymond] C. J. Raymond, M. R. Murnane, S. L. Prins, S. Sohail, H. Naqvi, and J. R. McNeil, Multiparameter grating metrology using optical scatterometry. *J. Vacuum Sci. Technol. B* **15**, 361–368 (1997).

[6] [2016 Boef] A. J. den Boef, Optical wafer metrology sensors for process-robust CD and overlay control in semiconductor device manufacturing. *Surface Topography—Metrology and Properties* **4**, 023001 (2016).

[7] [2009 Erni] R. Erni, M. D. Rossell, C. Kisielowski and U. Dahmen, Atomic-resolution imaging with a sub-50-pm electron probe. *Phys. Rev. Lett.* **102**, 096101 (2009).

[8] [1991 Sarid] D. Sarid and V. Elings. Review of scanning force microscopy. *Journal of Vacuum Science & Technology B: Microelectronics and Nanometer Structures*, **9**, 431 (1991).

[9] [2004 Jalili] N. Jalili and K. Laxminarayana. A review of atomic force microscopy imaging systems: application to molecular metrology and biological sciences. *Mechatronics*, **14**, 907–945 (2004).

[10] [2015 Sunday] D. F. Sunday, S. List, J. S. Chawla, and R. J. Kline, Determining the shape and periodicity of nanostructures using small-angle X-ray scattering. *J. Appl. Cryst.* **48**, 1355–1363 (2015).

[11] [2002 Engel] B. N. Engel, N. D. Rizzo, J. Janesky, J. M. Slaughter, R. Dave, M. Deherrera, M. Durlam, and S. Tehrani. The Science and Technology of Magnetoresistive Tunneling Memory. *IEEE Transactions on Nanotechnology*, **1**(1) (2002).

[12] [2020 Frazer] T. D. Frazer, J. L. Knobloch, J. N. Hernández-charpak, K. M. Hoogeboompot, D. Nardi, S. Yazdi, W. Chao, E. H. Anderson, M. K. Tripp, S. W. King, H. C. Kapteyn, M. M. Murnane, and B. Abad. Full characterization of ultrathin 5nm low-k dielectric bilayers: Influence of dopants and surfaces on the mechanical properties. *Phys. Rev. Materials*, **4**(7), 073603 (2020).

[13] [2010 Martinez] A. Martinez, N. Seoane, A. R. Brown, J. R. Barker, and A. Asenov. Variability in Si nanowire MOSFETs due to the combined effect of interface roughness and random dopants: A fully three-dimensional NEGF simulation study. *IEEE Transactions on Electron Devices*, **57**(7), 1626–1635 (2010).

[14] [2020 Mori] K. Mori, S. Samata, N. Mitsugi, A. Teramoto, R. Kuroda, T. Suwa, K. Hashimoto, and S. Sugawa. Influence of silicon wafer surface roughness on semiconductor device characteristics. *Japanese Journal of Applied Physics*, **59**(SMMB06) (2020).

[15] [2013 Arisawa] Y. Arisawa, T. Terasawa, and H. Watanabe. Impact of EUV mask roughness on lithography performance. *Proc. SPIE **8679**, Extreme Ultraviolet (EUV) Lithography IV*, 86792S (2013).

[16] [2020 Rook] K. Rook, P. Turner, N. Srinivasan, T. Henry, K. Yamamoto, and M. H. Lee, Process optimization for performance improvement in Mo/Si multilayers for EUV mask blanks. *Proc. SPIE **11517**, Extreme Ultraviolet Lithography*, 1151708 (2020).

[17] [2010 Mochi] I. Mochi, K. A. Goldberg, B. La Fontaine, A. Tchikoulaeva, and C. Holfeld, Actinic imaging of native and programmed defects on a full-field mask. *Proc. SPIE **7636**, Extreme Ultraviolet (EUV) Lithography*, 76361A (2010).

[18] [2017 Gardner] D. F. Gardner, M. Tanksalvala, E. R. Shanblatt, X. Zhang, B. R. Galloway, C. L. Porter, R. Karl Jr, C. Bevis, D. E. Adams, H. C. Kapteyn, M. M. Murnane, and G. F. Mancini, Subwavelength coherent imaging of periodic samples using a 13.5 nm tabletop high-harmonic light source, *Nat. Photon.*, **11**(4), 259–263, (2017).

[19] [2022 Eschen] W. Eschen, L. Loetgering, V. Schuster, R. Klas, A. Kirsche, L. Berthold, M. Steinert, T. Pertsch, H. Gross, M. Krause, J. Limpert, and J. Rothhardt, Material-specific high-resolution table-top extreme ultraviolet microscopy. *Light: Science & Applications*, **11**, 117 (2022).

[20] [2021 Tanksalvala] M. Tanksalvala, C. L. Porter, Y. Esashi, B. Wang, N. W. Jenkins, Z. Zhang, G. P. Miley, J. L. Knobloch, B. McBennett, N. Horiguchi, S. Yazdi, J. Zhou, M. N. Jacobs, C. S. Bevis, R. M. Karl, P. Johnsen, D. Ren, L. Waller, D. E. Adams, S. L. Cousin, C.-T. Liao, J. Miao, M. Gerrity, H. C. Kapteyn, and M. M. Murnane, Nondestructive, high-resolution, chemically specific 3D nanostructure characterization using phase-sensitive EUV imaging reflectometry, *Sci. Adv.* **7**(5), eabd9667 (2021).

[21] [1993 Henke] B. L. Henke, E. M. Gullikson, and J. C. Davis, X-Ray Interactions: Photoabsorption, Scattering, Transmission, and Reflection at E = 50-30,000 eV, Z = 1-92, *Atomic Data and Nuclear Data Tables*, **54**(2), 181–342 (1993).

[22] [2016 Shanblatt] E. R. Shanblatt, C. L. Porter, D. F. Gardner, G. F. Mancini, R. M. Karl Jr, M. D. Tanksalvala, C. S. Bevis, V. H. Vartanian, H. C. Kapteyn, D. E. Adams, and M. M. Murnane, Quantitative chemically specific coherent diffractive imaging of reactions at buried interfaces with few nanometer precision, *Nano Lett.* **16**(9), 5444–5450, (2016).

[23] [2016 Attwood] D. Attwood and A. Sakdinawat, X-rays and Extreme Ultraviolet Radiation: Principles and Applications, 2nd edition, Cambridge University Press, (2016).

[24] [Wikipage Wilhelm] https://en.wikipedia.org/wiki/Wilhelm_R%C3%B6ntgen

[25] [1972 Horowitz] P. Horowitz and J. A. Howell, A scanning x-ray microscope using synchrotron radiation. *Science* **178**, 608–611 (1972).

[26] [1992 McNulty] I. McNulty, J. Kirz, C. Jacobsen, E. H. Anderson, M. R. Howells, and D. P. Kern, High Resolution Imaging by Fourier Transform X-ray Holography. *Science* **256**, 1009–1012 (1992).

[27] [2004 Eisebitt] S. Eisebitt, J. Lüning, W. F. Schlotter, M. Lörgen, O. Hellwig, W. Eberhardt, and J. Stöhr, Lensless imaging of magnetic nanostructures by X-ray spectro-holography. *Nature* **432**, 885–888 (2004).

[28] [1948 Kirkpatrick] P. Kirkpatrick and A. V. Baez, Formation of optical images by X-rays. *J. Opt. Soc. Am.* **38**, 766–774 (1948).

[29] [2000 Artioukov] I. A. Artioukov, K. M. Krymski, Schwarzschild objective for soft x-rays, *Opt. Eng.* **39**(8) (2000).

[30] [2012 Artyukov] I. A. Artyukov, “Schwarzschild objective and similar two-mirror systems,” *Proc. SPIE* **8678**, 86780A (2012).

[31] [2006 Budano] A. Budano, F. Flora, and L. Mezi, Analytical design method for a modified Schwarzschild optics. *Appl. Opt.* **45**, 4254–4262 (2006).

[32] [2006 Bollanti] S. Bollanti, P. Di Lazzaro, F. Flora, L. Mezi, D. Murra, and A. Torre, Conventional and modified Schwarzschild objective for EUV lithography: Design relations, *Appl. Phys. B* **85**, 603–610 (2006).

[33] [2015 Morgan] A. J. Morgan, M. Prasciolu, A. Andrejczuk, J. Krzywinski, A. Meents, D. Pennicard, H. Graafsma, A. Barty, R. J. Bean, M. Barthelmess, D. Oberthuer, O. Yefanov, A. Aquila, H. N. Chapman, and S. Bajt, High numerical aperture multilayer Laue lenses. *Sci. Rep.* **5**, 9892 (2015).

[34] [1991 Jacobsen] C. Jacobsen, S. Williams, E. Anderson, M. T. Browne, C. J. Buckley, D. Kern, J. Kirz, M. Rivers, and X. Zhang, Diffraction-limited imaging in a scanning transmission x-ray microscope, *Opt. Commun.* **86**, 351–364 (1991).

[35] [2012 Chao] W. Chao, P. Fischer, T. Tyliszczak, S. Rekawa, E. Anderson, and P. Naulleau, Real space soft x-ray imaging at 10 nm spatial resolution, *Opt. Exp.* **20**(9), 9777-9783 (2012).

[36] [2013 Döring] F. Döring, A. L. Robisch, C. Eberl, M. Osterhoff, A. Ruhlandt, T. Liese, F. Schlenkrich, S. Hoffmann, M. Bartels, T. Salditt, and H. U. Krebs, Sub-5 nm hard x-ray point focusing by a combined Kirkpatrick-Baez mirror and multilayer zone plate, *Opt. Express* **21**(16), 19311– 19323 (2013).

[37] [2008 De Jonge] M. D. De Jonge, B. Hornberger, C. Holzner, D. Legnini, D. Paterson, I. McNulty, C. Jacobsen, and S. Vogt, Quantitative phase imaging with a scanning transmission X-ray microscope, *Phys. Rev. Lett.* **100**, 163902 (2008).

[38] [2009 Huang] X. Huang, H. Miao, J. Steinbrener, J. Nelson, D. Shapiro, A. Stewart, J. Turner, and C. Jacobsen, Signal-to-noise and radiation exposure considerations in conventional and diffraction X-ray microscopy, *Opt. Exp.* **17**(16), 13541–13553 (2009).

[39] [Gardner Thesis] D. F. Gardner, Coherent Diffractive Imaging Near the Spatio-Temporal Limit with High-Harmonic Sources, PhD Thesis, University of Colorado Boulder (2017).

[40] [1998 Miao] J. Miao, D. Sayre, and H. N. Chapman, Phase retrieval from the magnitude of the fourier transforms of nonperiodic objects. *J. Opt. Soc. Am. A,* **15**(6), 1662–1669, (1998).

[41] [2001 Robinson] I. K. Robinson, I. A. Vartanyants, G. J. Williams, M. A. Pfeifer, and J. A. Pitney, Reconstruction of the shapes of gold nanocrystals using coherent x-ray diffraction. *Phys. Rev. Lett.* **87**(19), 195505, (2001).

[42] [2003 Williams] G. J. Williams, M. A. Pfeifer, I. A. Vartanyants, and I. K. Robinson, Three-dimensional imaging of microstructure in au nanocrystals. *Phys. Rev. Lett*. **90**(17), 175501, (2003).

[43] [2006 Pfeifer] M. A. Pfeifer, G. J. Williams, I. A. Vartanyants, R. Harder, and I. K. Robinson, Three-dimensional mapping of a deformation field inside a nanocrystal. *Nature*, **442**(7098), 63–66, (2006).

[44] [2017 Holler] M. Holler, M. Guizar-Sicairos, E. H. R. Tsai, R. Dinapoli, E. Muller, O. Bunk, J. Raabe, and G. Aeppli, High-resolution non-destructive three-dimensional imaging of integrated circuits, *Nature* **543**, 402-406 (2017).

[45] [2010 Dierolf] M. Dierolf, A. Menzel, P. Thibault, P. Schneider, C. M. Kewish, R. Wepf, O. Bunk, and F. Pfeiffer, Ptychographic X-ray computed tomography at the nanoscale, *Nature* **467**, 436–439 (2010).

[46] [2020 Baksh] P. D. Baksh, M. Ostrčil, M. Miszczak, C. Pooley, R. T. Chapman, A. S. Wyatt, E. Springate, J. E. Chad, K. Deinhardt, J. G. Frey, and W. S. Brocklesby, Quantitative and correlative extreme ultraviolet coherent imaging of mouse hippocampal neurons at high resolution, *Sci. Adv.* **6**(18), eaaz3025 (2020).

[47] [2003 Elser] V. Elser, Phase retrieval by iterated projections. *J. Opt. Soc. Am. A*, **20**(1), 40–55, (2003).

[48] [2007 Marchesini] Stefano Marchesini, Invited article: A unified evaluation of iterative projection algorithms for phase retrieval. *Review of scientific instruments*, **78**(1), 011301, (2007).

[49] [1982 Fienup] J. R. Fienup, Phase retrieval algorithms: a comparison. *Applied optics*, **21**(15), 2758–2769, (1982).

[50] [1980 Sayre] D. Sayre, Prospects for long-wavelength x-ray microscopy and diffraction. In *Imaging Processes and Coherence in Physics*, 229–235, Springer, (1980).

[51] [2002 Bauschke] H. H. Bauschke, P. L. Combettes, and D. R. Luke, Phase retrieval, error reduction algorithm, and fienup variants: a view from convex optimization. *J. Opt. Soc. Am. A*, **19**(7), 1334–1345, (2002).

[52] [Bevis Thesis] C. Bevis, Ptychography Coherent Diffractive Imaging Systems for Extreme Ultraviolet and X-ray Sources, PhD Thesis, University of Colorado Boulder (2020).

[53] [1972 Gerchberg] R. W. Gerchberg, and W. O. Saxton, A practical algorithm for the determination of phase from image and diffraction plane pictures. *Optik* **35**(2), 237-246 (1972).

[54] [1984 Levi] A. Levi, and H. Stark, Image restoration by the method of generalized projections with application to restoration from magnitude. *J. Opt. Soc. Am. A* **1**(9), 932-943 (1984).

[55] [2005 Luke] D. R. Luke, Relaxed average alternating reflections for diffraction imaging, *Inverse Problems* **21**, 37-50 (2005).

[56] [1999 Miao] J. Miao, P. Charalambous, J. Kirz, and D. Sayre, Extending the methodology of X-ray crystallography to allow imaging of micrometre-sized non-crystalline specimens, *Nature* **400**, 342–344 (1999).

[57] [1969 Hoppe] W. Hoppe, Diffraction in inhomogeneous primary wave fields: 1. Principle of phase determination from electron diffraction interference, *Acta Crystallogr. A* **25**, 495–501 (1969)

[58] [1995 Nellist] P. D. Nellist, B. C. McCallum, and J. M. Rodenburg, Resolution beyond the 'information limit' in transmission electron microscopy. *Nature*, **374**, 630–632, (1995).

[59] [2004 Rodenburg] J. M. Rodenburg and H. M. L. Faulkner, A phase retrieval algorithm for shifting illumination. *Applied Physics Letters*, **85**(20), 4795–4797, (2004).

[60] [2009 Thibault] P. Thibault, M. Dierolf, O. Bunk, A. Menzel, and F. Pfeiffer, Probe retrieval in ptychographic coherent diffractive imaging, *Ultramicroscopy*, **109**(4), 338–343, (2009).

[61] [2009 Maiden] A. M. Maiden and J. M. Rodenburg, An improved ptychographical phase retrieval algorithm for diffractive imaging, *Ultramicroscopy* **109**(10), 1256–1262 (2009).

[62] [2007 Rodenburg PRL] J. M. Rodenburg, A. C. Hurst, A. G. Cullis, B. R. Dobson, F. Pfeiffer, O. Bunk, C. David, K. Jefimovs, and I. Johnson, Hard-X-ray lensless imaging of extended objects, *Phys. Rev. Lett.* **98**(3), 034801 (2007).

[63] [2008 Thibault] P. Thibault, M. Dierolf, A. Menzel, O. Bunk, C. David, and F. Pfeiffer, High-Resolution Scanning X-ray Diffraction Microscopy, *Science* **321**(5887), 379–382 (2008).

[64] [2014 Seaberg] M. D. Seaberg, B. Zhang, D. F. Gardner, E. R. Shanblatt, M. M. Murnane, H. C. Kapteyn, and D. E. Adams, Tabletop nanometer extreme ultraviolet imaging in an extended reflection mode using coherent Fresnel ptychography, *Optica* **1**(1), 39–44 (2014).

[65] [2018 Pfeifer] F. Pfeiffer, X-ray ptychography, *Nat. Photon.*, **12**(1), 9–17, (2018).

[66] [Porter Thesis] C. L. Porter, Complex Extreme Ultraviolet Imaging Reflectometry: Quantitative Lensless Imaging with Short-Wavelength Light in Reflection Geometries, PhD Thesis, University of Colorado Boulder (2018).

[67] [2017 Maiden] A. Maiden, D. Johnson, and P. Li, Further improvements to the ptychographical iterative engine, *Optica*, **4**(7), 736–745, (2017).

[68] [2014 Batey] D. J. Batey, D. Claus, and J. M. Rodenburg, Information multiplexing in ptychography, *Ultramicroscopy* **138**, 13–21 (2014).

[69] [2011 Maiden] A. M. Maiden, M. J. Humphry, F. Zhang, and J. M. Rodenburg, Superresolution imaging via ptychography, *J. Opt. Soc. Am. A*, **28**(4), 604–612, (2011).

[70] [2013 Edo] T. B. Edo, D. J. Batey, A. M. Maiden, C. Rau, U. Wagner, Z. D. Peˇsi´c, T. A. Waigh, and J. M. Rodenburg, Sampling in x-ray ptychography, *Phys. Rev. A*, **87**(5), 053850, 2013.

[71] [Tenio Thesis] T. Popmintchev. Tunable Ultrafast Coherent Light in the Soft and Hard X-ray Regions of the Spectrum: Phase Matching of Extreme High-Order Harmonic Generation. PhD thesis, University of Colorado, Boulder, (2009).

[72] [Galloway Thesis] B. R. Galloway. High-Order Harmonic Generation Driven by Mid-Infrared Laser Light. PhD thesis, University of Colorado, Boulder, (2017).

[73] [Fan Thesis] T. Fan. Bright Linearly and Circularly Polarized Extreme Ultraviolet and Soft X-Ray High Harmonics for Absorption Spectroscopy. PhD thesis, University of Colorado, Boulder, (2017).

[74] [1998 Rundquist] A. Rundquist, C. G. Durfee, Z. Chang, C. Herne, S. Backus, M. M. Murnane, and H. C. Kapteyn, Phase-matched generation of coherent soft x-rays, *Science* **280**(5368), 1412–1415, (1998).

[75] [2002 Bartels] R. A. Bartels, A. Paul, H. Green, H. C. Kapteyn, M. M. Murnane, S. Backus, I. P. Christov, Y. Liu, D. Attwood, and C. Jacobsen, Generation of spatially coherent light at extreme ultraviolet wavelengths, *Science* **297**(5580), 376–378, (2002).

[76] [2009 Popmintchev] T. Popmintchev, M.-C. Chen, A. Bahabad, M. Gerrity, P. Sidorenko, O. Cohen, I. P. Christov, M. M. Murnane, and H. C. Kapteyn, Phase matching of high harmonic generation in the soft and hard x-ray regions of the spectrum, *Proc. Natl. Acad. Sci. U S A* **106**(26), 10516–10521, (2009).

[77] [2012 Popmintchev] T. Popmintchev, M.-C. Chen, D. Popmintchev, P. Arpin, S. Brown, S. Aliˇsauskas, G. Andriukaitis, T. Balˇciunas, O. D. M¨ucke, A. Pugzlys, A. Baltuska, B. Shim, S. E. Schrauth, A. Gaeta, C. Hernndez-Garca, L. Plaja, A. Becker, A. Jaron-Becker, M. M. Murnane, and H. C. Kapteyn, Bright coherent ultrahigh harmonics in the kev x-ray regime from mid-infrared femtosecond lasers, *Science* **336**(6086), 1287–1291, (2012).

[78] [2016 Tao] Z. Tao, C. Chen, T. Szilv´asi, M. Keller, M. Mavrikakis, H. C. Kapteyn, and M. M. Murnane, Direct time-domain observation of attosecond final-state lifetimes in photoemission from solids, *Science* **353**(6294), 62–67, (2016).

[79] [2018 You] W. You, P. Tengdin, C. Chen, X. Shi, D. Zusin, Y. Zhang, C. Gentry, A. Blonsky, M. Keller, P. M. Oppeneer, H. C. Kapteyn, Z. Tao, and M. M. Murnane, Revealing the nature of the ultrafast magnetic phase transition in ni by correlating extreme ultraviolet magneto-optic and photoemission spectroscopies, *Phys. Rev. Lett.* **121**(7), 077204, (2018).

[80] [2018 Tengdin] P. Tengdin, W. You, C. Chen, X. Shi, D. Zusin, Y. Zhang, C. Gentry, A. Blonsky, M. Keller, P. M. Oppeneer, H. C. Kapteyn, Z. Tao, and M. M. Murnane, Critical behavior within 20 fs drives the out-of-equilibrium laser-induced magnetic phase transition in nickel, *Sci. Adv.* **4**(3), eaap9744, (2018).

[81] [2019 Shi] X. Shi, W. You, Y. Zhang, Z. Tao, P. M. Oppeneer, X. Wu, R. Thomale, K. Rossnagel, M. Bauer, H. C. Kapteyn, and M. M. Murnane, Ultrafast electron calorimetry uncovers a new long-lived metastable state in 1t-tase2 mediated by mode-selective electron-phonon coupling, *Sci. Adv.* **5**(3), eaav4449, (2019).

[82] [2020 Zhang] Y. Zhang, X. Shi, W. You, Z. Tao, Y. Zhong, F. C. Kabeer, P. Maldonado, P. M. Oppeneer, M. Bauer, K. Rossnagel, H. C. Kapteyn, and M. M. Murnane, Coherent modulation of the electron temperature and electron–phonon couplings in a 2d material, *Proc. Natl. Acad. Sci. U S A* **117**(16), 8788–8793, (2020).

[83] [2015 Hoogeboom-Pot] K. M. Hoogeboom-Pot, J. N. Hernandez-Charpak, X. Gu, T. D. Frazer, E. H. Anderson, W. Chao, R. W. Falcone, R. Yang, M. M. Murnane, H. C.

Kapteyn, D. Nardi, A new regime of nanoscale thermal transport: Collective diffusion increases dissipation efficiency, *Proc. Natl. Acad. Sci. U S A* **112**(16), 4846-4851 (2015).

[84] [2019 Frazer] Travis D Frazer, Joshua L Knobloch, Kathleen M Hoogeboom-Pot, Damiano Nardi, Weilun Chao, Roger W Falcone, Margaret M Murnane, Henry C Kapteyn, and Jorge N HernandezCharpak. Engineering nanoscale thermal transport: Size-and spacing-dependent cooling of nanostructures. *Phys. Rev. Appl.*, 11(2):024042, 2019.

[85] [2015 Zhang] B. Zhang, D. F. Gardner, M. D. Seaberg, E. R. Shanblatt, H. C. Kapteyn, M. M. Murnane, and D. E. Adams, High contrast 3D imaging of surfaces near the wavelength limit using tabletop EUV ptychography, *Ultramicroscopy*, **158**, 98–104, (2015).

[86] [2018 Karl] R. M. Karl, G. F. Mancini, J. L. Knobloch, T. D. Frazer, J. N. Hernandez-Charpak, B. Abad, D. F. Gardner, E. R. Shanblatt, M. Tanksalvala, C. L. Porter, C. S. Bevis, D. E. Adams, H. C. Kapteyn, and M. M. Murnane, Full-field imaging of thermal and acoustic dynamics in an individual nanostructure using tabletop high harmonic beams, *Sci. Adv.* **4**(10), eaau4295 (2018).

[87] [2022 Brooks] N. J. Brooks, B. Wang, I. Binnie, M. Tanksalvala, Y. Esashi, J. L. Knobloch, Q. L. D. Nguyen, B. McBennett, N. W. Jenkins, G. Gui, Z. Zhang, H. C. Kapteyn, M. M. Murnane, and C. S. Bevis, Temporal and spectral multiplexing for EUV multibeam ptychography with a high harmonic light source, *Opt. Exp.*, **30**(17), 30331-30346 (2022).

[88] [1987 McPherson] A. McPherson, G. Gibson, H. Jara, U. Johann, T. S. Luk, I. A. McIntyre, K. Boyer, and C. K. Rhodes. Studies of multiphoton production of vacuum-ultraviolet radiation in the rare gases. *J. Opt. Soc. Am. B*, **4**(4), 595–601, (1987).

[89] [1988 Elder] F. R. Elder, A. M. Gurewitsch, R. V. Langmuir, and H. C. Pollock. Radiation from Electrons in a Synchrotron. *Phys. Rev.* **71**(11), 829–830, (1947).

[90] [1993 Macklin] J. J. Macklin, J. D. Kmetec, and C. L. Gordon. High-order harmonic generation using intense femtosecond pulses. *Phys. Rev. Lett.*, **70**(6), 766–769, (1993).

[91] [1993 L'Huillier] A. L'Huillier and Ph. Balcou. High-order harmonic generation in rare gases with a 1-ps 1053-nm laser. *Phys. Rev. Lett.* **70**(6), 774–777, (1993).

[92] [1993 Corkum] P. B. Corkum, Plasma perspective on strong-field multiphoton ionization, *Phys. Rev. Lett.*, **71**(13), 1994– 1997 (1993).

[93] [1993 Kulander] K. C. Kulander, K. J. Schafer, J. L. Krause, Dynamics of short-pulse excitation, ionization and harmonic generation, *In Proceedings on Super-Intense Laser-Atom Physics (SILAP III)*, Plenum, New York, 95-110, (1993).

[94] [1994 Lewenstein] M. Lewenstein, P. Balcou, M. Y. Ivanov, A. L'Huillier, and P. B. Corkum, Theory of high-harmonic generation by low-frequency laser fields, *Phys. Rev. A* **49**(3), 2117–2132, (1994).

[95] [2007 Kapteyn] H. C. Kapteyn, O. Cohen, I. Christov, and M. M. Murnane, Harnessing attosecond science in the quest for coherent x-rays, *Science* **317**(5839), 775-778 (2007).

[96] [1986 Ammosov] M. V. Ammosov, N. B. Delone, and V. P. Krainov, Tunnel ionization of complex atoms and of atomic ions in an alternating electromagnetic field, *J. Exp. Theo. Phys.* **64**(6), 1191–1194, (1986).

[97] [2004 Zhang] X. Zhang, A. R. Libertun, A. Paul, E. Gagnon, S. Backus, I. P. Christov, M. M. Murnane, H. C. Kapteyn, R. A. Bartels, Y. Liu, and D. T. Attwood, Highly coherent light at 13 nm generated by use of quasi-phase-matched high-harmonic generation, *Opt. Lett.* **29**(12), 1357–1359, (2004).

[98] [Rundquist Thesis] A. R. Rundquist, Phase-matched generation of coherent, ultrafast x-rays using high harmonics, PhD thesis, University of Colorado, Boulder, (1998).

[99] [1999 Durfee] C. G. Durfee, A. R. Rundquist, S. Backus, C. Herne, M. M. Murnane, and H. C. Kapteyn, Phase Matching of High-Order Harmonics in Hollow Waveguides, *Phys. Rev. Lett.* **83**(11), 2187–2190, (1999).

[100] [2017 Chen] C. Chen, Z. Tao, A. Carr, P. Matyba, T. Szilvási, S. Emmerich, M. Piecuch, M. Keller, D. Zusin, S. Eich, M. Rollinger, W. You, S. Mathias, U. Thumm, M. Mavrikakis, M. Aeschlimann, P. M. Oppeneer, H. Kapteyn, and M. Murnane, Distinguishing attosecond electron-electron scattering and screening in transition metals, *Proc. Natl. Acad. Sci.* **114**(27), E5300–E5307 (2017).

[101] [2017 Kfir] O. Kfir, S. Zayko, C. Nolte, M. Sivis, M. Möller, B. Hebler, S. S. Phani, K. Arekapudi, D. Steil, S. Schäfer, M. Albrecht, O. Cohen, S. Mathias, and C. Ropers, Nanoscale magnetic imaging using circularly polarized high-harmonic radiation, *Sci. Adv.* **3**(12), eaao4641 (2017).

[102] [2020 Tengdin] P. Tengdin, C. Gentry, A. Blonsky, D. Zusin, M. Gerrity, L. Hellbrück, M. Hofherr, J. Shaw, Y. Kvashnin, E. K. Delczeg-Czirjak, M. Arora, H. Nembach, T. J. Silva, S. Mathias, M. Aeschlimann, H. C. Kapteyn, D. Thonig, K. Koumpouras, O. Eriksson, and M. M. Murnane, Direct light-induced spin transfer between different elements in a spintronic Heusler material via femtosecond laser excitation, *Sci. Adv.* **6**(3), eaaz1100 (2020).

[103] [2021 Honarvar] H. Honarvar, J. L. Knobloch, T. D. Frazer, B. Abad, B. McBennett, M. I. Hussein, H. C. Kapteyn, M. M. Murnane, and J. N. Hernandez-Charpak, Directional

thermal channeling: A phenomenon triggered by tight packing of heat sources, *Appl. Phys. Sci.* **118**(40), e2109056118 (2021).

[104][2021 Beardo] A. Beardo, J. L. Knobloch, L. Sendra, J. Bafaluy, T. D. Frazer, W. Chao, J. N. Hernandez-Charpak, H. C. Kapteyn, B. Abad, M. M. Murnane, F. X. Alvarez, and J. Camacho, A General and Predictive Understanding of Thermal Transport from 1D- And 2D-Confined Nanostructures: Theory and Experiment, *ACS Nano* **15**(8), 13019–13030 (2021).

[105][2022 Zhang] Y. Zhang, X. Shi, M. Guan, W. You, Y. Zhong, T. R. Kafle, Y. Huang, H. Ding, M. Bauer, K. Rossnagel, S. Meng, H. C. Kapteyn, and M. M. Murnane, Creation of a novel inverted charge density wave state, *Structural Dynamics* **9**, 014501 (2022).

[106][2021 Zayko] S. Zayko, O. Kfir, M. Heigl, M. Lohmann, M. Sivis, M. Albrecht, and C. Ropers, Ultrafast high-harmonic nanoscopy of magnetization dynamics, *Nat. Comm.* **12**, 6337 (2021).

[107][2004 Agostini] P. Agostini and L. F. DiMauro, The physics of attosecond light pulses, *Reports on Progress in Physics* **67**(6), 813–855 (2004).

[108][2010 Popmintchev] T. Popmintchev, M. C. Chen, P. Arpin, M. M. Murnane, and H. C. Kapteyn, The attosecond nonlinear optics of bright coherent X-ray generation, *Nat. Photon.* **4**, 822–832 (2010).

[109][2016 Calegari] F. Calegari, G. Sansone, S. Stagira, C. Vozzi, and M. Nisoli, Advances in attosecond science, *J. Phys. B: At. Mol. Opt. Phys.* **49**, 062001 (2016).

[110][2010 Chen] M. C. Chen, P. Arpin, T. Popmintchev, M. Gerrity, B. Zhang, M. Seaberg, D. Popmintchev, M. M. Murnane, and H. C. Kapteyn, Bright, coherent, ultrafast soft x-ray

harmonics spanning the water window from a tabletop light source, *Phys. Rev. Lett.* **105**, 173901 (2010).

[111][2004 Faulkner] H. M. L. Faulkner and J. M. Rodenburg, Movable aperture lensless transmission microscopy: A novel phase retrieval algorithm, *Phys. Rev. Lett.* **93**(2), 023903 (2004).

[112][2022 Loetgering] L. Loetgering, S. Witte, and J. Rothhardt, Advances in laboratory-scale ptychography using high harmonic sources [Invited], *Opt. Exp.* **30**(3), 4133–4164 (2022).

[113][2017 Donnelly] C. Donnelly, M. Guizar-Sicairos, V. Scagnoli, S. Gliga, M. Holler, J. Raabe, and L. J. Heyderman, Three-dimensional magnetization structures revealed with X-ray vector nanotomography, *Nature* **547**, 328–331 (2017).

[114][2021 Rana] A. Rana, C.-T. Liao, E. Iacocca, J. Zou, M. Pham, E.-E. C. Subramanian, Y. H. Lo, S. A. Ryan, X. Lu, C. S. Bevis, R. M. Karl, A. J. Glaid, Y.-S. Yu, P. Mahale, D. A. Shapiro, S. Yazdi, T. E. Mallouk, S. J. Osher, H. C. Kapteyn, V. H. Crespi, J. v Badding, Y. Tserkovnyak, M. M. Murnane, and J. Miao, Direct observation of 3D topological spin textures and their interactions using soft x-ray vector ptychography, arXiv:2104.12933 (2021).

[115][2013 Pan] X. Pan, C. Liu, and J. Zhu, Single shot ptychographical iterative engine based on multi-beam illumination, *Appl. Phys. Lett.* **103**, 171105 (2013).

[116][2016 Sidorenko] P. Sidorenko and O. Cohen, Single-shot ptychography, *Optica* **3**(1), 9–14 (2016).

[117][2020 Goldberger] D. Goldberger, J. Barolak, C. G. Durfee, and D. E. Adams, Three-Dimensional Single-Shot Ptychography, *Opt. Exp.* **28**(13), 18887–18898 (2020).

[118][2022 Barolak] J. Barolak, D. Goldberger, J. Squier, Y. Bellouard, C. Durfee, and D. Adams, Wavelength-multiplexed single-shot ptychography, *Ultramicroscopy* **233**, 113418 (2022).

[119][2015 Karl] R. Karl, C. Bevis, R. Lopez-Rios, J. Reichanadter, D. Gardner, C. Porter, E. Shanblatt, M. Tanksalvala, G. F. Mancini, M. Murnane, H. Kapteyn, and D. Adams, Spatial, spectral, and polarization multiplexed ptychography, *Opt. Exp.* **23**(23), 30250–30258 (2015).

[120][2018 Bevis] C. Bevis, R. Karl, J. Reichanadter, D. F. Gardner, C. Porter, E. Shanblatt, M. Tanksalvala, G. F. Mancini, H. Kapteyn, M. Murnane, and D. Adams, Multiple beam ptychography for large field-of-view, high throughput, quantitative phase contrast imaging, *Ultramicroscopy* **184**, 164–171 (2018).

[121][2020 Hirose] M. Hirose, T. Higashino, N. Ishiguro, and Y. Takahashi, Multibeam ptychography with synchrotron hard X-rays, *Opt. Exp.* **28**(2), 1216–1224 (2020).

[122][2020 Yao] Y. Yao, Y. Jiang, J. A. Klug, M. Wojcik, E. R. Maxey, N. S. Sirica, C. Roehrig, Z. Cai, S. Vogt, B. Lai, and J. Deng, Multi-beam X-ray ptychography for high-throughput coherent diffraction imaging, *Sci. Rep.* **10**, 19550 (2020).

[123][2021 Wittwer] F. Wittwer, M. Lyubomirskiy, F. Koch, M. Kahnt, M. Seyrich, J. Garrevoet, C. David, and C. G. Schroer, Upscaling of multi-beam x-ray ptychography for efficient x-ray microscopy with high resolution and large field of view, *Appl. Phys. Lett.* **118**, 171102 (2021).

[124][2012 Gardner] D. F. Gardner, B. Zhang, M. D. Seaberg, L. S. Martin, D. E. Adams, F. Salmassi, E. Gullikson, H. Kapteyn, and M. Murnane, High numerical aperture reflection

mode coherent diffraction microscopy using off-axis apertured illumination, *Opt. Exp.* **20**(17), 19050–19059 (2012).

[125][2017 Porter] C. L. Porter, M. Tanksalvala, M. Gerrity, G. Miley, X. Zhang, C. Bevis, E. Shanblatt, R. Karl, M. M. Murnane, D. E. Adams, and H. C. Kapteyn, General-purpose, wide field-of-view reflection imaging with a tabletop 13 nm light source, *Optica* **4**(12), 1552–1557 (2017).

[126][2017 Sidorenko] P. Sidorenko, O. Lahav, and O. Cohen, Ptychographic ultrahigh-speed imaging, *Opt. Exp.* **25**(10), 10997–11008 (2017).

[127][2019 Wengrowicz] O. Wengrowicz, O. Peleg, B. Loevsky, B. K. Chen, G. I. Haham, U. S. Sainadh, and O. Cohen, Experimental time-resolved imaging by multiplexed ptychography, *Opt. Exp.* **27**(17), 24568–24577 (2019).

[128][2014 Huang] X. Huang, H. Yan, R. Harder, Y. Hwu, I. K. Robinson, and Y. S. Chu, Optimization of overlap uniformness for ptychography, *Opt. Exp.* **22**, 12634–12644 (2014).

[129][2013 Thibault] P. Thibault and A. Menzel, Reconstructing state mixtures from diffraction measurements, *Nature* **494**, 68–71 (2013).

[130][1949 Shannon] C. E. Shannon, Communication in the Presence of Noise, *Proceedings of the IRE* **37**, 10–21 (1949).

[131][2005 Heel] M. van Heel and M. Schatz, Fourier shell correlation threshold criteria, *Journal of Structural Biology* **151**, 250–262 (2005).

[132][2016 Zhang] B. Zhang, D. F. Gardner, M. H. Seaberg, E. R. Shanblatt, C. L. Porter, R. Karl, C. A. Mancuso, H. C. Kapteyn, M. M. Murnane, and D. E. Adams, Ptychographic

hyperspectral spectromicroscopy with an extreme ultraviolet high harmonic comb, *Opt. Exp.* **24**, 18745–18754 (2016).

[133][2018 Esashi] Y. Esashi, C.-T. Liao, B. Wang, N. Brooks, K. M. Dorney, C. Hernández-García, H. Kapteyn, D. Adams, and M. Murnane, Ptychographic amplitude and phase reconstruction of bichromatic vortex beams, *Opt. Exp.* **26**, 34007–34015 (2018).

[134][2020 Rana] A. Rana, J. Zhang, M. Pham, A. Yuan, Y. H. Lo, H. Jiang, S. J. Osher, and J. Miao, Potential of Attosecond Coherent Diffractive Imaging, *Phys. Rev. Lett.* **125**, 086101 (2020).

[135][2021 Goldberger] D. Goldberger, D. Schmidt, J. Barolak, B. Ivanic, C. G. Durfee, and D. E. Adams, Spatiospectral characterization of ultrafast pulse-beams by multiplexed broadband ptychography, *Opt. Exp.* **29**, 32474–32490 (2021).

[136][2021 Loetgering] L. Loetgering, X. Liu, A. C. C. de Beurs, M. Du, G. Kuijper, K. S. E. Eikema, and S. Witte, Tailoring spatial entropy in extreme ultraviolet focused beams for multispectral ptychography, *Optica* **8**, 130–138 (2021).

[137][2012 Larruquert] J. I. Larruquert, L. v. Rodríguez-de Marcos, J. A. Méndez, P. J. Martin, and A. Bendavid, High reflectance ta-C coatings in the extreme ultraviolet, *Opt. Exp.* **21**, 27537–27549 (2013).

[138][2015 Popmintchev] D. Popmintchev, C. Hernández-García, F. Dollar, C. Mancuso, J. A. Pérez-Hernández, M.-C. Chen, A. Hankla, X. Gao, B. Shim, A. L. Gaeta, M. Tarazkar, D. A. Romanov, R. J. Levis, J. A. Gaffney, M. Foord, S. B. Libby, A. Jaron-Becker, A. Becker, L. Plaja, M. M. Murnane, H. C. Kapteyn, and T. Popmintchev, Ultraviolet surprise: Efficient soft x-ray high-harmonic generation in multiply ionized plasmas, *Science* **350**, 1225–1231 (2015).

[139][2022 Rego] L. Rego, N. J. Brooks, Q. L. D. Nguyen, J. San Román, I. Binnie, L. Plaja, H. C. Kapteyn, M. M. Murnane, and C. Hernández-García, Necklace-structured high-harmonic generation for low-divergence, soft x-ray harmonic combs with tunable line spacing, *Sci. Adv.* **8**, eabj7380 (2022).

[140][2018 EUV Lithography book] V. Bakshi, EUV Lithography, SPIE Press, Bellingham, Washington, (2018).

[141][2018 Luong] V. Luong, V. Philipsen, E. Hendrickx, K. Opsomer, C. Detavernier, C. Laubis, F. Scholze, M. Heyns, Ni-Al alloys as alternative EUV mask absorber, *Appl. Sci.* **8**(4), 521 (2018).

[142][2019 Miyai] H. Miyai, T. Kohyama, T. Suzuki, K. Takehisa, and H. Kusunose, Actinic patterned mask defect inspection for EUV lithography, *Proc. SPIE Photomask Technology* **11148**, 111480W (2019).

[143][2019 Capelli] R. Capelli, M. Dietzel, D. Hellweg, M. Koch, G. Kersteen, K. Gwosch, D. Pagel, Actinic metrology platform for defect review and mask qualification: flexibility and performance, *Proc. SPIE Extreme Ultraviolet (EUV) Lithography* **10957**, 109570X (2019).

[144][2019 Mochi] I. Mochi, S. Fernandez, R. Nebling, U. Locans, P. Helfenstein, R. Rajeev, A. Dejkameh, D. Kazazis, L.-T. Tseng, and Y. Ekinci, Absorber and phase defect inspection on EUV reticles using RESCAN, *Proc. SPIE Extreme Ultraviolet (EUV) Lithography* **10957**, 109570W (2019).

[145][2019 Nagata] Y. Nagata, T. Harada, T. Watanabe, H. Kinoshita, and K. Midorikawa, At wavelength coherent scatterometry microscope using high-order harmonics for EUV mask inspection, *Int. J. Extrem. Manuf.* **1,** 032001 (2019).

[146][2020 Mochi] I. Mochi, H.-S. Kim, U. Locans, A. Dejkameh, R. Nebling, D. Kazazis, and Y. Ekinci, Illumination control in lensless imaging for EUV mask inspection and review, *Proc. SPIE Extreme Ultraviolet (EUV) Lithography* **11323**, 113231I (2020).

[147][2022 Kim] Y. W. Kim, D. G. Lee, S. Moon, C. M. Ku, J. H. Cho, and J. Ahn, Actinic patterned mask imaging using extreme ultraviolet ptychography microscope with high harmonic generation source, *Appl. Phys. Express* **15**, 076505 (2022).

[148][2009 Beck] A. Beck, and M. Teboulle, Fast gradient-based algorithms for constrained total variation image denoising and deblurring problems, *IEEE Trans. Image Process.* **18**(11), 2419-2434 (2009).

[149][2014 David] D. A. Shapiro, Y.-S. Yu, T. Tyliszczak, J. Cabana, R. Celestre, W. Chao, K. Kaznatcheev, A. L. D. Kilcoyne, F. Maia, S. Marchesini, Y. S. Meng, T. Warwick, L. L. Yang, and H. A. Padmore, Chemical composition mapping with nanometre resolution by soft X-ray microscopy, *Nat. Photon.* **8**, 765-769 (2014).

[150][2015 Donnelly] C. Donnelly, M. Guizar-Sicairos, V. Scagnoli, M. Holler, T. Huthwelker, A. Menzel, I. Vartiainen, E. Muller, E. Kirk, S. Gliga, J. Raabe, and L. J. Heyderman, Element-specific x-ray phase tomography of 3D structures at the nanoscale, *Phys. Rev. Lett.* **114**, 115501 (2015).

[151][2007 Rodenburg Ultramicroscopy] J. M. Rodenburg, A. C. Hurst, & A. G. Cullis, Transmission microscopy without lenses for objects of unlimited size. *Ultramicroscopy* **107**, 227-231 (2007).

[152][2012 Thibault] P. Thibault, and M. Guizar-Sicairos, Maximum-likelihood refinement for coherent diffractive imaging, *New J. Phys.* **14**, 063004 (2012).

[153][2018 Lazarev] S. Lazarev, I. Besedin, A. V. Zozulya, J.-M. Meijer, D. Dzhigaev, O. Yu. Gorobtsov, R. P. Kurta, M. Rose, A. G. Shabalin, E. A. Sulyanova, I. A. Zaluzhnyy, A. P. Menushenkov, M. Sprung, A. V. Petukhov, and I. A. Vartanyants, Ptychographic x-ray imaging of colloidal crystals, *Small* **14**, 1702575 (2018).

[154][2018 Mancini] G. F. Mancini, R. M. Karl, E. R. Shanblatt, C. S. Bevis, D. F. Gardner, M. D. Tanksalvala, J. L. Russell, D. E. Adams, H. C. Kapteyn, J. V. Badding, T. E. Mallouk, and M. M. Murnane, Colloidal crystal order and structure revealed by tabletop extreme ultraviolet scattering and coherent diffractive imaging. *Opt. Exp.* **26**, 11393-11406 (2018).

[155][2013 Goldberg] K. A. Goldberg,I. Mochi, M. Benk, A. P. Allezy, M. R. Dickinson, C. W. Cork, D. Zehm, J. B. Macdougall, E. Anderson, F. Salmassi, W. Chao, V. K. Vytla, E. M. Gullikson, J. C. DePonte, M. S. Gideon Jones, D. V. Camp, J. F. Gamsby, W. B. Ghiorso, H. Huang, W. Cork, E. Martin, E. V. Every, E. Acome, V. Milanovic, R. Delano, P. P. Naulleau, and S. B. Rekawa, Commissioning an EUV mask microscope for lithography generations reaching 8 nm. *Proc. SPIE* **8679**, *Extreme Ultraviolet (EUV) Lithography IV*, 867919 (2013).

[156][2016 Helfenstein] P. Helfenstein, I. Mohacsi, R. Rajendran, and Y. Ekinci, Scanning coherent diffractive imaging methods for actinic EUV mask metrology. *Proc. SPIE* **9776**, *Extreme Ultraviolet (EUV) Lithography VII*, 97761F (2016).

[157][2017 Hellweg] D. Hellweg, S. Perlitz, K. Magnusson, R. Capelli, M. Koch, and M. Malloy, Actinic review of EUV masks: performance data and status of the AIMS^{TM} EUV system, *Proc. SPIE* **10143**, *Extreme Ultraviolet (EUV) Lithography VIII*, 101430J (2017).

[158][2017 Rajeev] R. Rajeev, I. Mochi, P. Helfenstein, I. Mohacsi, S. Redford, A. Mozzanica, B. Schmitt, S. Yoshitake, and Y. Ekinci, Towards a stand-alone high-throughput EUV actinic photomask inspection tool – RESCAN, *Proc. SPIE* **10145**, *Metrology, Inspection, and Process Control for Microlithography XXXI*, 101450N (2017).

[159][2020 Mochi] I. Mochi, S. Fernandez, R. Nebling, U. Locans, R. Rajeev, A. Dejkameh, D. Kazazis, L.-T. Tseng, S. Danylyuk, L. Juschkin, and Y. Ekinci, Quantitative characterization of absorber and phase defects on EUV reticles using coherent diffraction imaging, *J. of Micro/Nanolithography, MEMS, and MOEMS* **19**, 014002 (2020).

[160][2022 Wang] B. Wang, N. Brooks, M. Tanksalvala, Y. Esashi, N. Jenkins, P. Johnsen, I. Binnie, G. Gui, Y. Shao, M. M. Murnane, H. C. Kapteyn, Robust and reliable actinic ptychographic imaging of highly periodic structures in EUV photomasks, *Proc. SPIE* **XXXX**, *Photomask Technology*, 765–776 (2000).

[161][1969 Hoppe and Strube] W. Hoppe, G. Strube, Diffraction in inhomogeneous primary wave fields: 2. Optical experiments for phase determination of lattice interferences, *Acta Crystallogr. A* **25**, 502–507 (1969).

[162][1970 Hegerl and Hoppe] R. Hegerl, W. Hoppe: Dynamic theory of crystalline structure analysis by electron diffraction in inhomogeneous primary wave field, *Ber. Bunsenges. Phys. Chem.* **74**(11), 1148–1154 (1970).

[163][2014 Thibault] P. Thibault, M. Guizar-Sicairos, A. Menzel, Coherent imaging at the difraction limit, *J. Synchrotron Radiat.* **21**, 1011–1018 (2014).

[164][2004 Sutherland] J.R. Sutherland, E. L. Christensen, N. D. Powers, S. E. Rhynard, J.C. Painter, and J. Peatross, High harmonic generation in a semi-infinite gas cell, *Opt. Exp.* **12**, 4430-4436 (2004).

[165][2009 Steingrube] Steingrube, D. S. *et al.* Phase matching of high-order harmonics in a semi-infinite gas cell. *Phys. Rev. A* **80**, 043819 (2009).

[166][2013 Hernández García] C. Hernández García, A. Picon, J. S. Roman, and L. Plaja, Attosecond extreme ultraviolet vortices from high-order harmonic generation, *Phys. Rev. Lett.* **111**, 083602 (2013).

[167][2014 Gariepy] G. Gariepy, J. Leach, K. T. Kim, T. J. Hammond, E. Frumker, R. W. Boyd, and P. B. Corkum, Creating high-harmonic beams with controlled orbital angular momentum, *Phys. Rev. Lett.* **113**, 153901 (2014).

[168][2016 Géneaux] R. Géneaux, A. Camper, T. Auguste, O. Gobert, J. Caillat, R. Taieb, and T. Ruchon, Synthesis and characterization of attosecond light vortices in the extreme ultraviolet, *Nat. Commun.* **7**, 12583 (2016).

[169][2017 Coudert-Alteirac] H. Coudert-Alteirac, H. Dacasa, F. Campi, E. Kueny, B. Farkas, F. Brunner, S. Maclot, B. Manschwetus, H. Wikmark, J. Lahl, L. Rading, J. Peschel, B. Major, K. Varju, G. Dovillaire, P. Zeitoun, P. Johnsson, A. L'Huillier, and P. Rudawski, Micro-focusing of broadband high-order harmonic radiation by a double toroidal mirror, *Appl. Sci.* **7**(11), 1159 (2017).

[170][2000 Komatsuda] H. Komatsuda, Novel illumination system for EUVL, *Proc. SPIE* **3997**, *Emerging Lithographic Technologies IV*, 765–776 (2000).